FUSION CROSS SECTION MEASUREMENTS FOR THE REACTIONS $^{14}N + ^{10}B$ AND $^{16}O + ^{16}O$

Thesis by

Shiu-Chin Wu

In Partial Fulfillment of the Requirements
For the Degree of
Doctor of Philosophy

California Institute of Technology
Pasadena, California

1978

(Submitted May 24, 1978)

ACKNOWLEDGMENTS

It has been a great pleasure and unforgettable experience working with my advisor, Professor C. A. Barnes, whose guidance and encouragement made this thesis possible.

I would like to express my deep gratitude to Dr. Z. E. Switkowski for introducing me to the techniques of heavy ion measurements. Professor J. C. Overley has also provided stimulating discussion and encouragement throughout the course of this work. The $^{14}N + ^{10}B$ was carried out in collaboration with both of them.

A special thank-you goes to the members of the Kellogg Radiation Laboratory: Mr. Bud Warrick for helping with operating the tandem accelerator, Mr. H. S. Wilson for many helpful discussions and for the anodized tantalum target used in Part II, Dr. F. Mann for the use of the computer code HAUSER*4, and Mr. G. Fox for assistance in some of the computer programming.

Above all, I would like to thank my parents for giving me the opportunity of being a physicist, and my husband, Chien-Ping Lee for his love and enormous help in data accumulation and analysis.

Finally, I am grateful for the support provided by Graduate Research Assistantships from the California Institute of Technology. This research was supported in part by the National Science Foundation (PHY76-83685).

ABSTRACT

PART I

The $^{14}N + ^{10}B$ fusion reactions have been studied at c.m. energies between 2.9 and 7.5 MeV by measuring the γ-ray yields from the residual nuclei with a Ge(Li) detector. Cross sections were deduced from these yields with the aid of statistical model calculations. $^{14}N + ^{10}B$ elastic scattering differential cross sections were measured from $E_{cm} = 3.3$ to 9.1 MeV at $\theta_{cm} = 74.4°$ and $90.0°$. The fusion cross sections of $^{14}N + ^{10}B$ are compared with an IWBC calculation employing a parameter set obtained by fitting the elastic scattering data.

PART II

Total fusion cross sections have been measured for the $^{16}O + ^{16}O$ reactions from $E_{cm} = 7$ to 12 MeV. Prompt γ-ray yields, measured by a Ge(Li) detector, were used to determine the cross sections for the formation of the various possible evaporation residues, as well as the total fusion cross sections, with the assistance of statistical model calculations. The total fusion cross section S-factors agrees well with previous data from this laboratory, measured by detecting evaporated light particles, and disagrees with more recent work carried out elsewhere.

TABLE OF CONTENTS

PART I: $^{14}N + ^{10}B$

PART II: $^{16}O + ^{16}O$

LIST OF TABLES

LIST OF FIGURES

Figure No. Page

PART I

PART II

PART I

FUSION CROSS SECTION MEASUREMENTS FOR THE REACTION $^{14}N + ^{10}B$

I. INTRODUCTION

I.1 The Motivation for Heavy Ion Fusion Measurements

Aside from the general nuclear reaction theory aspects of heavy ion reactions, the main interest in very low-energy heavy ion reactions at Caltech stems from the importance of the $^{12}C + ^{12}C$, $^{12}C + ^{16}O$ and $^{16}O + ^{16}O$ reactions in stellar evolution. The first reaction in nucleosynthesis converts hydrogen into helium in the center of a star (Ba 71). Following exhaustion of the hydrogen fuel, the central region of the star contracts and heats up. When the helium core becomes hot enough, helium burning begins, and gravitational contraction is halted. The reactions occurring in the helium-burning stage are $3\alpha \rightarrow ^{12}C$, $^{12}C(\alpha,\gamma)^{16}O$ and $^{16}O(\alpha,\gamma)^{20}Ne$. As the helium-burning comes to an end with the exhaustion of the helium supply, the core of the star contracts again, while the temperature rises to $\sim 7 \times 10^{8}$ °K. At this temperature (kT=60 keV, E_{eff}=1.8 MeV), ^{12}C begins to react with ^{12}C and the energy output may once again stabilize the star by balancing the gravitational force. Because of the higher Coulomb barrier, the reaction of $^{16}O + ^{16}O$ is not expected to occur until somewhat higher temperature, $\sim 10^{9}$ °K, after the exhaustion of ^{12}C. The most effective energy for the $^{16}O + ^{16}O$ reaction is approximately 4 MeV at this temperature. Reactions between ^{12}C and ^{16}O are not very important, at least as a source of energy (Cl 68). At carbon-burning temperatures, the larger Coulomb barrier renders the rate of $^{12}C + ^{16}O$ too low to be important, and the carbon is nearly completely exhausted by the time the temperature has risen to a sufficient value to ignite $^{12}C + ^{16}O$ reactions.

The three reactions involving ^{12}C and ^{16}O have been studied extensively. The $^{12}C + ^{12}C$ reaction has been measured previously by Patterson, et al (Pa 69), Mazarakis, et al (Ma 73). Resonances were found in the sub-barrier energy region. Recently, more efforts (Hi77b, Ke 77) were made to study this reaction down to a center of mass energy of approximately 2.5 MeV. The $^{12}C + ^{16}O$ reaction has been studied down to $E_{c.m.}$=4 MeV by Čujec and Barnes (Ču 76), and Christensen, et al (Ch 77a). For the reaction of $^{16}O + ^{16}O$, cross sections have been measured by Spinka and Winkler (Sp 74) from center of mass energy 6.8 MeV to 11.9 MeV.

The astrophysical reaction rates for these reactions were predicted by extrapolating the measured cross section S-factor downward to the energies of astrophysical interest. The S-factor, given by

$$S(E) = \sigma(E) \quad E \quad \exp(2\pi\eta) \quad , \qquad \text{(I-1)}$$

where $\eta = Z_1 Z_2 e^2/(\hbar v)$, has less energy dependence than $\sigma(E)$. The quantity v is the relative velocity (at large separation) between the projectile (Z_1,A_1) and the target (Z_2,A_2), and E refers to the center-of-mass energy.

Fig. 1 shows the S-factor for the $^{12}C + ^{12}C$ reactions from previous measurements. Both narrow (~100 keV) and broad (~2 MeV) resonances were found at and below the Coulomb barrier (Pa 69, Ma 73). In particular, there are large resonances below 3 MeV center-of-mass energy (See Hi 77b, Ke 77). The uncertainties in the extrapolation of S-factor curves down to low energies have sparked interest in the low-energy systematics of fusion reactions in general, and several examples have now been studied (St 76).

I.2 $^{14}N + ^{10}B \rightarrow (^{24}Mg)$ and $^{12}C + ^{12}C \rightarrow (^{24}Mg)$

Although most of the measured fusion reaction cross sections have a smooth energy dependence below the Coulomb barrier (see Fig. 1 of St 76), the $^{12}C + ^{16}O$ fusion cross sections fluctuate with energy (Ču 76, Ch 77a) although not so strongly as is the case for $^{12}C + ^{12}C$. Hypotheses adduced to explain this behavior include: compound nucleus fluctuations due to overlapping resonances, "quasi-molecular" resonances or some other form of intermediate structure (Mi 72, Mi 73), such as α-clustering, or entrance-channel effects dependent on the microscopic structure of the interaction nuclei.

The $^{14}N + ^{10}B$ reaction is of special interest in this regard, because it forms the same compound nuclear system as the $^{12}C + ^{12}C$ reaction. Fig. 2 illustrates the Q-values for formation of the compound nucleus, ^{24}Mg, and indicates most of the residual nuclei which can be formed by subsequent particle evaporation. Because the $^{14}N + ^{10}B$ reaction forms ^{24}Mg at much higher excitation energies than $^{12}C + ^{12}C$ reaction, compound nucleus resonance fluctuation effects should be considerably reduced by the higher level density. Furthermore, the microscopic structures of the two pairs of interacting nuclei are very different, with α-particle clustering presumably of less importance in the $^{14}\mathrm{N} + {}^{10}\mathrm{B}$ case. Although these features of the $^{14}\mathrm{N} + {}^{10}\mathrm{B}$ system would lead one to expect no structure in the energy dependence of the reaction cross section, structure has been observed recently in the $\alpha+{}^{20}\mathrm{Ne}$ channel (Ma 74) at energies above the Coulomb barrier.

Two quite different experimental techniques have been used for the measurement of fusion cross sections by observing the deexcitation γ-rays from residual nuclei. The first employed two large, high-efficiency NaI scintillators (Ču 76, Hi 76), each subtending a solid angle of nearly 2π sr at the target. The spectra of non-coincident events from the two counters were summed, and the total fusion cross sections were deduced after correcting for background, non-radiative transitions, and detection efficiency. The second technique employed a single high-resolution Ge(Li) detector to identify the formation of particular residual nuclei by observing transitions between low-lying states populated mainly through deexcitation cascades. The latter technique, described in Ch.II and III, has the advantage that the cross sections for production of different residual nuclei can be determined, as well as the total fusion cross section.

In the present experiment, the latter technique was used to determine the $^{14}\mathrm{N} + {}^{10}\mathrm{B}$ fusion cross sections between $E_{cm}=2.9$ and 7.5 MeV. During the late stages of the present work, High and Čujec (Hi 77a) reported a measurement on the same reaction which employed the former technique. Their data are compared with the results of the present investigation in Chapter III and Chapter VI.

Besides the fusion cross sections, the $^{14}N + {}^{10}B$ elastic scattering excitation functions were also measured at laboratory angles θ_L=30.0° and 35.5°, corresponding to $\theta_{c.m.}$=74.4° and 90.0°, respectively. In Chapter V, the scattering data are used to determine the parameters of the real ion-ion potential within the framework of the IWBC model (Ch 77b). The IWBC model is then used to calculate the expected fusion cross sections, for comparison with the measured cross sections.

Chapter VI also compares the fusion S-factors of the $^{14}N + {}^{10}B$ reactions with the results of earlier measurements of $^{12}C + {}^{12}C$ by Patterson, et al (Pa 69).

II. EXPERIMENTAL PROCEDURE, FUSION CROSS SECTIONS OF $^{14}N + ^{10}B$

II.1 General Description

In the fusion cross section measurements for the $^{14}N + ^{10}B$ reactions, the target was mounted at the end of a 15 cm long, 2 cm inside diameter, stainless steel tube. This tube, insulated from ground by quartz rods, was then placed inside the target chamber (See, for example, Fig. 1 of Ch 77a). The target chamber, connected with a copper gasket to the ultra-high vacuum system of the S-20° beam station of the Caltech tandem accelerator, was pumped by a combined ion-sublimation pump. When isolated from the beam pipe, the pressure in the pump was typically below 10^{-8} torr. The targets, which were perpendicular to the beam direction, were always mounted in the vacuum system at least twelve hours before being bombarded in order to reach a sufficiently high vacuum. During the runs, the pressure of the target chamber was normally below 2×10^{-8} torr. To minimize carbon deposition on the target, the ultra-high vacuum target region was isolated from the upstream beam tube and the remainder of the accelerator by a 30 cm long liquid-nitrogen cold trap. The beam traversed a 1 cm diameter tube through the trap.

Beams of ^{14}N (and ^{16}O, ^{12}C, and ^{19}F when necessary) of different charge states (3^+ or 4^+), were delivered by the ONR-CIT tandem accelerator. Secondary electrons were suppressed electrostatically, and a permanent magnet was placed approximately 40 cm upstream from the target, to prevent secondary electrons scattered from apertures or from the beam pipe from reaching the target chamber. The beam current integration was determined to be reliable to better than 5%.

A 73 cm^3 Ge(Li) detector was placed at 0° to measure the gamma-ray yields. The energy resolution of the Ge(Li) detector was typically 3.0 keV for the 1.33 MeV line from a ^{60}Co source. In all fusion measurements, the detector was surrounded by at least 10 cm of lead to minimize the room background (natural radioactivity and cosmic radiation). The geometry of the whole system including target chamber and the detector was always chosen to be the same as one of the geometries for which the Ge(Li) efficiency was determined (See Section II.3).

Three different geometries were used during the course of experiments: (1) A 3 mm sheet of lead was inserted between the detector and the target, and the detector was put as close as possible to the target. The distance from the target to the Germanium crystal surface was 1.4 cm. (2) No lead was put between the target and the detector in order to transmit the low-energy γ-rays to the detector. (3) The detector was placed approximately 2 cm away from the target chamber to keep the electronic dead time during the efficiency calibration below 10%. In this case the distance between the target and the Germanium crystal surface is 3.3 cm.

Prompt γ-ray spectra were stored in 4096 channels (or 8192 channels) of a Nuclear Data 4420 analyzing system. The beam intensity, limited to keep the detection electronics dead time below 12%, varied from $\sim$1μA at the lowest energies to $\sim$20 nA at the highest energies. The amount of integrated beam charge was chosen to yield a sufficient number of counts for the dominant peaks in the pulse height spectrum. The statistical errors of the strongest peak were less than 1% for most bombarding energies, and approximately 20% for the lowest energy. The yields of γ-rays were obtained by summing the counts in the photopeak for each γ-ray peak. Backgrounds from the Compton scattering of higher energy γ-rays were subtracted by assuming that they varied linearly with channel number over a small interval around the photopeak.

Occasional "beam-off" spectra were measured to insure that the build-up of delayed activities was not significant, and also to provide spectra from which corrections could be made for any neighboring natural-background lines. To minimize the possible effects of activation of the target or its surroundings, measurements were always performed from lower beam energies to higher energies.

II.2 Targets

Targets were prepared by electron-beam evaporation of elemental boron isotopically enriched to 96.2% of ^{10}B. For the fusion cross section measurements, the boron was deposited on 99.99% spectroscopically pure copper discs of 0.25 mm thickness. A more detailed description of the techniques for making boron targets is given in Chapter IV.

Two methods were used to determine the ^{10}B content on the copper-backed targets: (1) Proton scattering and (2) Coulomb excitation of ${}^{10}B$. The previously measured cross sections of ${}^{12}C$ + ${}^{10}B$ (Da 76a) were also checked against methods (1) and (2). The ${}^{12}C$ and ${}^{16}O$ contents of the target were determined by the ${}^{14}N$ + ${}^{12}C$ and ${}^{14}N$ + ${}^{16}O$ reactions (Sw 77a).

II.2.A Proton Elastic Scattering

The ${}^{10}B$ content of the copper-backed targets was determined by elastic scattering of protons at E_{lab}=2.183 MeV and θ_{lab}=140°. At this energy and angle (θ_{cm}=143.7°), the elastic scattering cross section passes through a broad maximum and σ/σ_{Ruth}=9.9 (Ov 61, Ov 62). Thus, although the ${}^{10}B$ scattering peak was superimposed on the thick-target elastic scattering yield from the copper substrate, the ${}^{10}B$ scattering yield was large enough that it could be determined to ±2% within a reasonably short time.

A surface-barrier semiconductor detector was used to detect the back-scattered protons from the ${}^{10}B$ layer and the copper backing. An aperture of 7.0±0.1mm diameter was used to determine the solid angle ($\Delta\Omega$=1.15x10^{-3} sr) to ±4%. The target was oriented so that the angle between the beam and the target normal direction was 20°. The spectrum accumulated with an integrated charge of 60 μCoulomb is shown in Fig. 3. The ${}^{10}B$ peak is easily resolved. Since the angle scale of the scattering chamber was known to ±0.1° (See IV.2), there was no significant error due to angular positioning. This implies that the accuracy of the target thickness determination was determined by the accuracy with which the solid angle and σ/σ_{Ruth} were known.

The previous measurements of σ/σ_{Ruth} were believed to have an accuracy of ±8% (Ov 61), and the target thickness determined from this (proton-scattering) method is 8.6±0.8 $\mu g/cm^2$. Proton elastic scattering was also used to determine the ^{10}B thickness of thin transmission targets, and the result will be compared with the thickness as measured by α-particle Rutherford scattering in Chapter IV.

II.2.B Coulomb Excitation of ^{10}B

The copper-backed targets were also bombarded by ^{14}N and ^{16}O ions, and the yields of the 718 keV γ-rays arising from the Coulomb excitation of the first excited state of ^{10}B were measured. Heavy ion Coulomb excitation studies of ^{10}B have been reported previously by Andreev(An 61). Coulomb excitation cross sections were calculated with the B(E2↑) value deduced from the measured lifetime of 1.013±0.015 nsec for the first excited state (Aj 74). Since the Coulomb excitation cross sections were calculated to be isotropic to within 2%, it is straightforward to deduce the ^{10}B content of the target if it can be assumed that Coulomb excitation is the dominant mechanism for the production of 718 keV γ-rays.

The formalism for calculating Coulomb excitation cross sections has been summarized by Alder, et al (Al 56, Al 66b). For ^{10}B, the spins and parities for ground state and the first excited state are 3^+ and 1^+, respectively. The reduced transition probability B(E2↑) is related to B(E2↓) by the expression

$$B(E2\uparrow) = \frac{2I_1 + 1}{2I_0 + 1} B(E2\downarrow) \qquad \text{(II-1)}$$

The symbols ↑(↓) stand for the transition $3^+ \rightarrow 1^+$ ($1^+ \rightarrow 3^+$), and I_i is the spin for state i. The B(E2↓) value is related to the mean life of the state by the expression

$$\frac{1}{\tau} = \frac{8\pi(\lambda+1)}{\lambda[(2\lambda+1)!!]^2} \frac{1}{\hbar} \left(\frac{E_\gamma}{\hbar c}\right)^{2\lambda+1} B(\lambda\downarrow) \quad , \qquad \text{(II-2)}$$

where λ defines the multipolarity of the transition(E2 for the present case), and τ is the mean lifetime of the 718 keV state of ^{10}B, 1.013±0.015 nsec. E_γ=718 keV.

The Coulomb excitation cross sections for an Eλ transition is given by

$$\sigma_{E\lambda} = c_{E\lambda} \, E_{MeV}^{\lambda-2} \, (E_{MeV} - \Delta E'_{MeV})^{\lambda-1} B(E\lambda) f_{E\lambda}(\eta_i, \xi) \quad , \qquad \text{(II-3)}$$

where E_{MeV} is the initial laboratory energy of the projectile, and $\Delta E' = (1 + \frac{A_1}{A_2})\Delta E$. ΔE = 718 keV for ^{10}B, and A_1 and A_2 are the mass numbers of the projectile and target nucleus, respectively. The quantity $c_{E\lambda}$ is given by

$$\begin{aligned} c_{E\lambda} &= \frac{Z_1^2 A_1}{40.03} \left[0.07199\left(1 + \frac{A_1}{A_2}\right) Z_1 Z_2\right]^{-2\lambda+2} \quad \text{barns} \\ &= 4.819 \, (1 + A_1/A_2)^{-2} \, A_1/Z_2^2 \quad \text{barns, for } \lambda=2. \end{aligned} \qquad \text{(II-4)}$$

The quantities $f_\lambda(\eta_i, \xi) = f_\lambda(\xi) \, R_\lambda(\eta_i, \xi)$ are given in Table II.3 and Fig. II.6 of reference Al 56.

For incident ^{14}N ions, the calculated cross sections ranged from 4.53 μb at E_{lab}=6.91 MeV (corresponding to ^{14}N beam at 7.0 MeV incident energy) to 313 μb at E_{lab} =12.52 MeV. Since the Coulomb barrier for ^{14}N + ^{10}B is approximately 5.85 MeV c.m. energy from IWBC calculations described in Chapter V, the Coulomb excitation cross sections can only be trusted up to about E_{lab}=14 MeV. For higher incident energies, nuclear excitation gradually becomes important and tends at first to decrease the excitation cross section since the nuclear and Coulomb matrix elements are most usually of opposite signs (one force is attractive, the other repulsive).

Figure 4 shows the calculated ^{10}B Coulomb excitation cross sections for both ^{14}N and ^{16}O projectiles. Also shown are the measured γ-ray yields normalized to the calculations. The ^{10}B content of the target deduced from this normalization factor and the measured γ-ray detection efficiency is 9.3±0.8 μg/cm^2. The main contributions to the target thickness uncertainty came from the uncertainties in the B(E2↑) value and efficiency calibrations.

The thickness measured by Coulomb excitation agrees with that determined from the proton elastic scattering measurements within ±5%. The agreement between the two methods of determining the ^{10}B content of the copper-backed target is particularly useful since all of the γ-ray spectra below 16 MeV laboratory energy, acquired during the fusion studies, include well-resolved 718 keV peaks, which then provide a built-in monitor of the ^{10}B target content. For the analysis of the fusion cross sections, the average of the two thickness determinations was used with an error of ±5%.

II.2.C The $^{12}C + {}^{10}B$ Reaction

Dayras, et al (Da 76a) have measured the fusion cross sections of $^{12}C + {}^{10}B$ and $^{12}C + {}^{11}B$ near the Coulomb barrier energy. The ^{10}B target thickness was determined by the Rutherford scattering of α-particles for a self-supporting boron foil target, and absolute fusion cross sections were obtained for other targets by normalizing to the yields from the calibrated self-supporting target. The most intense γ-rays from the $^{12}C + {}^{10}B$ reactions are the 937 keV line from $^{18}F + \alpha$, the 332 keV line from $^{21}Na + n$, and the 351 keV line from $^{21}Ne + p$. ^{12}C beams in the 3^+ state were used to bombard the ^{10}B target of the present experiment, over the range from 8.0 MeV to 11.0 MeV laboratory energy in 1.0 MeV steps. The assumption of (2J+1) population of residual nuclei (Sw 76) was used to calculate the summing and branching corrections described in III.1. The target thicknesses deduced from the previously measured cross sections were $12.1\pm1.8\ \mu g/cm^2$ from the ^{18}F channel, $10.2\pm2.0\ \mu g/cm^2$ from the ^{21}Ne channel, and $9.4\pm1.4\ \mu g/cm^2$ from the ^{21}Na channel.

The target thickness determined by the $^{12}C + {}^{10}B$ reactions is thus rather different from that determined by Coulomb excitation of ^{10}B. However, since the summing and branching correction factor calculated by using the (2J+1) population assumption can be quite different from that deduced from a statistical model of the compound nucleus, the target thickness as determined by the $^{12}C + {}^{10}B$ reactions will not have an accuracy better than 20%. The different thickness obtained from the ^{21}Na channel vs that obtained from the

^{21}Ne and ^{18}F channels may indicate the possibility of non-isotropic angular distributions for the different γ-rays, especially since the Ge(Li) detector was approximately 2.5 cm from the target because of the difficulty encountered in the photopeak efficiency calibration of the detector (See Section II.3).

II.2.D The ^{12}C and ^{16}O Content of the Boron Targets

It is indicated in Table 1 that the γ-rays observed for the ^{22}Na and ^{21}Ne residual nuclei, which are produced in the ^{14}N + ^{10}B reactions, can also be generated by fusion of ^{14}N with a ^{12}C target impurity. Fusion of either ^{12}C or ^{16}O nuclei with ^{14}N may also produce the 585 keV peak from the 1st excited state of ^{25}Mg by the reactions ^{12}C (^{14}N, p) ^{25}Mg or ^{16}O (^{14}N, αp) ^{25}Mg. At high ^{14}N beam energies, additional gamma ray lines to those displayed in Fig. 6 were observed. These include a line at 1779 keV, attributed to ^{28}Si formed from ^{14}N fusion with ^{16}O, and a line at 390 keV, from ^{25}Mg, which is formed through fusion of ^{14}N with both ^{16}O and ^{12}C. The 1369 keV line, which can arise from either ^{22}Na($6\rightarrow1$) or ^{24}Mg($1\rightarrow0$), was used to determine the ^{12}C content.

The 1528 keV γ-ray peak from ^{22}Na is much stronger than the 1369 keV peak in runs at low bombarding energy. This is to be expected because the summing and branching correction factors in the ^{22}Na nucleus are roughly the same for the two gamma rays (See Section III.A). However, as the ^{14}N incident energy is increased, the 1369 keV peak shows the higher intensity. By comparing the excitation functions of these two γ-peaks, we can conclude that at least 90% of the total number of counts in the 1369 keV γ-ray peak comes from ^{24}Mg(1→0), for E(^{14}N)≥14 MeV. The intensity of the 1369 keV line at laboratory energies above 16.0 MeV and the previously measured cross section (Sw 77a) were therefore used to determine the ^{12}C content of the target. The thickness of ^{12}C thus determined was 6.0±0.9 μg/cm^2.

The amount of ^{16}O was determined by the size of the 1779 keV γ-ray peak, for E(^{14}N)≥16.0 MeV, to be 3.9±1.5 μg/cm^2. Because of the unusual peak shape of the 1779 keV γ-ray shown in Fig. 4 of Sw 77a , the uncertainty in the peak area was as high as ±40%.

The 390 keV γ-ray peak from ^{25}Mg may have contributions from both ^{14}N + ^{12}C and ^{14}N + ^{16}O reactions. The ^{12}C thickness was also determined from this gamma ray by the cross sections measured previously by Switkowski, et al (Sw 77a) as 8.7±1.8 μg/cm^2. All summing and branching correction factors were calculated assuming a population of the final states proportional to (2J+1). The uncertainty in the ^{12}C content of the target can change the cross section for producing the ^{22}Na channel by the reaction ^{14}N + ^{10}B by no more than 7%, and the cross section for ^{21}Ne by no more than 6%. The uncertainty in the ^{16}O content of the target does not contribute to the uncertainty in the cross sections for producing the ^{22}Na residual nucleus by the ^{14}N + ^{10}B reactions since the yield of the 585 keV γ-ray from ^{14}N + ^{16}O→^{25}Mg + αp gives less than a 4% correction to the 583 keV γ-rays of ^{22}Na.

II.2.E The Effective Energies

Since the cross section for fusion of two nuclei varies very rapidly with the center of mass energy, it is important to know the total energy-loss in the target when fusion cross sections are studied (Ču 76). The "energy-loss" thickness of the targets used in the present studies were measured by profiling the hydrogen contamination in the evaporated layers with the $^{1}H(^{19}F,\alpha\gamma)^{16}O$ reaction (Sw 75). Resonances corresponding to ^{19}F beam energies of 6.40 MeV (Γ=45 keV) and 16.44 MeV (Γ=86 keV) were used (Ba 77). An unshielded 5"x4" NaI(Tl) scintillation counter was used to detect γ-rays, and the counts for $E\gamma \geq 3.5$ MeV were integrated. Fig. 5 shows examples of the profiles obtained at the two resonances. The widths (in energy units) of the hydrogen distributions, measured as the interval between the half maximum points at the leading and tailing edges, were corrected for the natural resonance widths to obtain the energy-loss thickness for ^{19}F ions. These widths were then converted to thickness for other ions with the aid of the stopping-power tables of Northcliffe and Schilling (No 70). The energy-loss thicknesses of the targets were greater than would be expected from the measured ^{10}B contents alone because of the contributions to the energy loss from impurities in the targets, mainly ^{12}C and ^{16}O.

Since the target was measured as containing 6.0±0.9 $\mu g/cm^2$ of ^{12}C and 3.9±1.5 $\mu g/cm^2$ of ^{16}O, the total energy loss in the target can be calculated, including 8.9±0.6$\mu g/cm^2$ of ^{10}B, 3% of this amount of

^{11}B, and the ^{12}C and ^{16}O content of the target. The calculated energy loss at the E(^{19}F) = 6.40 MeV resonance was 238±37 keV, to be compared with the measured energy loss of 283±40 keV; at the 16.44 MeV resonance, the calculated energy loss was 222±25 keV, to be compared with the measured energy loss of 290±40 keV. These discrepancies probably reflect the difficulty in determining the true position of the front surface of the target by hydrogen profiling when the target is thin and there may possibly be a few atomic layers of water accumulated on the surface of the target. The hydrogen distributions shown in Fig. 5 also indicate some inhomogeneity of target composition. The target was sufficiently thin, however, that the effects of inhomogeneous composition could be ignored in determining the effective beam energy in the ^{10}B.

For all fusion cross sections measured here, the effective energies were taken to be the incident ^{14}N energies, minus one-half the energy-loss in the combined boron (^{10}B and ^{11}B), carbon and oxygen layer. The target was assumed to be uniform and homogeneous in composition, and no corrections were made for the non-linear energy dependence of the cross sections. For the thin target used here, such corrections were negligible compared with 0.1% uncertainty in the incident beam energy, determined by the beam analysis system.

II.3 Fusion Measurements

II.3.A Peak Identification

An example of a typical γ-ray pulse height spectrum is shown in

Fig. 6 with the numbered full-energy peaks identified in Table 1. Gamma rays were observed from residual nuclei formed by single-particle evaporation from the compound nucleus (^{20}Ne, ^{23}Na and ^{23}Mg), and by two-particle evaporation (^{16}O, ^{19}F, ^{19}Ne, ^{22}Ne and ^{22}Na). Although several three-particle evaporation channels are open, with the exception of ^{21}Ne, no residual nucleus formed by this process was observed. A complete data set was obtained with the gain illustrated in Fig. 6. A second complete set was obtained at lower gain to include the 6.131 MeV γ-rays from ^{16}O.

Since the first excited state of ^{10}B was observed easily, it is important to ask whether the 6.131 MeV excited state of ^{16}O could also be produced by Coulomb excitation of ^{16}O impurities by the ^{14}N beams. Coulomb excitation of ^{16}O (6.131 MeV) is not allowed energetically for ^{14}N energies below about 12 MeV. Even for 18 MeV ^{14}N incident energy, the calculated Coulomb excitation cross section is only of the order of 10^{-14} barns, which is far too small to produce any detectable counts in the 6.131 MeV γ-ray peak. Also, the first excited state of ^{12}C, 4.439 MeV (2^+), with higher Coulomb excitation cross sections at the same incident ^{14}N energy, was not observed during the runs, in spite of a detection efficiency roughly 1.5 times higher for 4 MeV γ-rays than for 6 MeV γ-rays. It is thus concluded that all of the counts from the ^{16}O 6.131 MeV state were due to the 2α-evaporation process of the ^{14}N+^{10}B fusion reactions.

For each outgoing channel, since the residual nuclei can be formed in any excited state allowed by energy conservation , the angular distributions of the gamma rays in cascades down to the ground state are averaged more and more; thus nearly isotropic angular distributions are expected for the γ-rays from low-lying excited states. For some of the residual nuclei, such as ^{19}F, ^{19}Ne and ^{22}Na, more than two γ-ray lines were identified, and at least two of them were used to determine the cross sections. In these cases, nonisotropic angular distribution effects would show up as different cross sections deduced for the same residual nucleus, if the observed γ-rays are independent transitions (not members of the same cascade; for example, the 110 keV γ-ray of ^{19}F (1→0) and the 197 keV γ-ray of ^{19}F (2→0)).

Cross sections for the formation of the various evaporation residues were determined from spectra similar to that shown in Fig. 6. For isotropic γ-ray emission, the relation between the full-energy-peak yield Y and the cross section σ is

$$\sigma = \frac{Y}{N\, n_t\, \varepsilon\beta} \quad , \tag{II-5}$$

where N is the number of incident ions, n_t is the areal number density of ^{10}B target atoms, and ε is the full energy peak detection efficiency. (For brevity, we refer to the full energy peak as the photopeak). The summing and branching factor β is the joint probability that a particular γ-ray is emitted after the residual nucleus is formed and that no other member of a deexcitation cascade is detected in coincidence in the detector.

The yield Y in Eq. (II-5) was obtained by summing the counts in the photopeak for each γ-ray. Backgrounds were assumed to vary linearly with channel number under the photopeak. The yields of γ-rays from ^{22}Na and ^{21}Ne were corrected for the contributions arising from the fusion reactions of ^{14}N with the ^{12}C and ^{16}O impurities. These contributions were calculated from the measured ^{12}C and ^{16}O content (II.2.D) and the measured ^{14}N + ^{12}C, ^{14}N + ^{16}O fusion cross sections of Switkowski, et al (Sw 77a). The γ-rays used in the cross section calculations are listed in Table 1. In those cases where more than one γ-ray is assigned to the same residual nucleus, cross sections were calculated from the intensities of each of the γ-rays and the results were averaged. Similarly, results from runs with different geometries and different targets were averaged. The data from different runs were consistent to within ±8%. The cross sections deduced from the intensities of different γ-rays from the same nucleus were consistent to within ±10%.

The summing and branching correction factors, β, were calculated from the relative populations of the various final states, the tabulated branching ratios (Aj 74, En 73), and the calculated total detection efficiencies. More details, and the results, of the calculations of the β's and the relative populations of final states are presented in Chapter III. The method employed for calculating total detection efficiencies is described elsewhere (Ma 75a).

II.3.B Ge(Li) Photopeak Efficiency Calibrations

When the detector was located as close to the target as possible, there was some difficulty in measuring the absolute efficiency because of the high dead time in the electronic system. The live-time fraction was as low as 60% for the ^{133}Ba calibration source, and the pile-up of signals was a serious problem. The Ge(Li) detector was therefore moved approximately 2 cm farther away from the target, and the efficiencies at the two distances were normalized at $E\gamma$ = 718 keV, where the Coulomb excitation was measured for the same target with both geometries, and over the region of energies, $E\gamma$ = 1.5 MeV to 7.5 MeV, where the relative efficiency was measured, with both geometries, with the ^{27}Al (p,γ) ^{28}Si reaction. For other geometries, since the dead-time correction was always below 10% and pile-up of signals was essentially absent, the absolute detection efficiencies were measured in separate independent measurements.

The Ge(Li) detector photopeak detection efficiencies for γ-rays with energies between 0.12 and 3.3 MeV were determined by placing calibrated radioactive sources at the target position, for each detector geometry used. The efficiency was extended to 10.76 MeV by measuring γ-ray yields from the ^{27}Al$(p,\gamma)^{28}$Si resonance at Ep = 992 keV, and using the known intensities of γ-rays in the deexcitation cascades relative to the 1.779 MeV transition.

(1) Absolute efficiencies

The absolute efficiencies were determined by placing the calibrated sources at the target position for each geometry. The sources used were

^{60}Co, 3.155 μC on Jan 4, 1966, $\tau_{1/2} = 5.26$ yr.

^{22}Na, 3.269 μC on April 15, 1966 $\tau_{1/2} = 2.602$ yr.

^{137}Cs, 3.355 μC on Sept 21, 1965 $\tau_{1/2} = 30.0$ yr.

^{133}Ba, 4.14 μC on June 3, 1969 $\tau_{1/2} = 10.5$ yr.

The number of quanta emitted per second by each source is given by

$$I = S_0 \times 3.7\times10^4 \ (\tfrac{1}{2})^{\Delta t/\tau_{1/2}} \ (\mu \text{ Curie})^{-1} \qquad \text{(II-6)}$$

where Δt is the time between the present efficiency measurements and the date of calibration of the source.

For a Ge(Li) detector, if two photons interact with the crystal simultaneously, the electron-hole pairs generated by the two interactions will be summed, and the outgoing signal will have an amplitude corresponding to the sum of the two separate signals. For example, since 99.8% of ^{60}Co nuclei decay into the 2.506 MeV state of ^{60}Ni, which then cascades through the 1.332 MeV state down to ground state, the Ge(Li) crystal will have no chance to detect the 1173 keV γ-ray, if it has already detected the 1332 keV γ-ray emitted in time-coincidence from the source. The total counts per second, Y, for the 1173 keV γ-ray is thus given by

$$Y_{1173} = I\cdot \mathrm{Eff}^{p}(1173)\cdot(1-\varepsilon^{t}_{1332}) \qquad (II-7)$$

where Eff^{p} is the photopeak efficiency for the 1173 keV γ-ray, and ε^{t}_{1332} is the calculated total detection efficiency for the 1332 keV γ-ray.

The situation is a little more complicated for the case of ^{133}Ba, for which a decay scheme is presented in Fig. 7. From the information available (See Nuclear Data Sheet Vol. 11, No 4, (1974)), the yield of counts for each γ-ray from ^{133}Ba source is:

276 keV:

$$Y = I\cdot \mathrm{Eff}^{p}(276)\cdot 0.865\cdot 0.089[0.88(1-\varepsilon^{t}_{161})+0.12(1-\varepsilon^{t}_{80})(1-\varepsilon^{t}_{81})] \qquad (II-8)$$

303 keV:

$$Y=I\cdot \mathrm{Eff}^{p}(303)\cdot[0.865\cdot 0.172\cdot 0.67(1-\varepsilon^{t}_{53})(1-\varepsilon^{t}_{81})+0.135\cdot 0.67(1-\varepsilon^{t}_{81})] \qquad (II-9)$$

356 keV: $Y = I\cdot \mathrm{Eff}^{p}(356)\cdot 0.856\cdot 0.739\cdot(1-\varepsilon^{t}_{81}) \qquad (II-10)$

384 keV:

$$Y = I\cdot \mathrm{Eff}^{p}(384)\cdot[0.865\cdot 0.172\cdot 0.312(1-\varepsilon^{t}_{53})+0.135\cdot 0.312] \qquad (II-11)$$

where I is the number of ^{133}Ba disintegration per second in the source.

In all of the efficiency calibration runs, electronic dead-time was below 10% for the geometries (1) and (3), described in II.1. However, the dead-time was very high for geometry (2), in which there was no lead absorber between the target and the Ge(Li) detector, and the distance between the target and the Germanium crystal was only 1.4 cm. Because of the high counting rate, the peak shapes have high-energy tails (pile-up phenomenon). No reliable absolute efficiency calibration was done. The measured absolute photopeak efficiencies as a function of γ-ray energy for geometries (1) and (3) are shown in Fig. 8.

(2) Relative efficiencies

Since γ-rays ranging from 110 keV to 6.131 MeV were employed in measuring the fusion cross sections, it is necessary to know the photopeak efficiency over this energy region. A ^{56}Co source of unknown strength, produced in this laboratory by the ^{56}Fe(p,n) ^{56}Co reaction, provided γ-ray peaks from 847 keV up to 3.3 MeV with well-known relative intensities (Ke 74, Mc 75). Table 2 lists the relative intensities of γ-ray transitions adopted for the present measurements. They are quoted with better than ±5% accuracy. With the same technique described in the previous subsection, relative efficiencies were determined up to 3.3 MeV.

The nucleus ^{57}Co emits three γ-rays at energies 122 keV, 136 keV and 692 keV, with the relative intensity 87.7: 12.2: 0.160, and was used to determine the relative efficiencies of γ-rays down to 120 keV. The lowest energy γ-ray used for determining the fusion cross sections was 110 keV. The 10 keV extrapolation of the efficiency curve down to 110 keV is believed to be accurate to better than ±5%.

^{27}Al(p,γ) has a resonance at E_p=992 keV (Me 69). The cascade branching ratio of the 12.542 MeV level of ^{28}Si has been measured previously (Bo 74), and is listed in Table 2. With the known decay scheme of the low-lying states of ^{28}Si (En 74), the relative intensity for ten γ-ray lines, ranging from 1.779 to 10.76 MeV, can be calculated. A 60 μg/cm^2 aluminum target (thickness measured by the laboratory's radiofrequency thickness monitor during the evaporation), on a one-inch diameter tantalum substrate, was mounted in the target chamber at exactly the same position as used in the ^{14}N+^{10}B fusion measurements. The Ge(Li) detector was set up to reproduce the same geometries as those used in the fusion measurements. Since the energy loss of 1 MeV protons in ^{27}Al is 0.174 keV/μg/cm^2, the total energy loss in this target is approximately 10 keV, much greater than either the natural width of the resonance or the beam energy resolution.

Protons of energies from 988 keV to 1000 keV, in 1 keV steps, were used to bombard the aluminum target, and the γ-rays with energy above 1.5 MeV were integrated. The excitation function of the high-energy γ-rays, with a constant integrated beam charge of 20 μCoulomb, is shown in Fig. 9. Long runs of the pulse height spectra were then accumulated at E_p=995 keV for each geometry. The relative photopeak efficiency of the Ge(Li) detector for each of ten γ-rays from 1.779 to 10.764 MeV was obtained from the spectra; a typical result is shown in Fig. 10. Although both the first and second escape peaks were also observed, for the most intense γ-rays, no effort was made to deduce the relative efficiencies for the escape peaks in terms of the photopeak efficiencies.

(3) 6.131 MeV γ-ray efficiency by $^{19}F(p,\alpha\gamma)\,^{16}O$

The photopeak efficiency at E = 6.131 MeV was separately measured by comparing the yields of the detected 6.131 MeV γ-rays from the $^{19}F(p,\alpha\gamma)\,^{16}O$ reaction at the E_p=340 keV resonance with the yield of the corresponding α-particles. The γ-rays and α-particles were detected simultaneously, with the Ge(Li) detector placed at a distance from the target which reproduces one of the geometries of the fusion measurements. For the $^{19}F(p,\alpha\gamma)\,^{16}O$ reaction at E_p=340 keV, the γ-rays and α-particles are both isotropic. The total number of α-particles emitted by the target, N_α, was obtained by dividing the number of α-particles detected by the fraction of the sphere subtended by the surface-barrier detector. The photopeak (and escape peak) efficiencies were determined by

$$\varepsilon_\gamma = N_\gamma/N_\alpha \quad , \qquad \text{(III-12)}$$

where N_γ is the number of γ-rays detected.

The photopeak efficiency for the 6.131 MeV γ-rays was measured by this method for one particular geometry. It was lower than the efficiency determined from the $^{27}Al(p,\gamma)$ reaction and the calibrated sources by approximately 6%. Since no dead-time correction was made for the $^{19}F(p,\alpha\gamma)\,^{16}O$ measurement, it was concluded that this discrepancy was not significant and that the efficiency calibrations from the $^{27}Al(p,\gamma)$ reaction were reliable up to the region of 10 MeV.

III. FUSION CROSS SECTIONS

III.1 Summing and Branching Ratios

In a nuclear reaction, the residual nuclei may be formed in their ground states or in any of their excited states (subject to energy and other conservation laws). The simultaneous detection by the Ge(Li) detector of two or more γ-rays of a cascade will result in the loss of the event from all of the photopeaks of interest (except for the rare case when the detected γ-rays sum to yield the same energy as another γ-ray). Furthermore, not all of the states populated in the residual nuclei contribute to the yield of the γ-rays selected for measurement. To estimate these two effects, the branching ratios of the excited states, and the relative populations of the excited states and the ground state must be known for each residual nucleus. For the low lying states of the residual nuclei of the ^{14}N + ^{10}B fusion reaction, the branching ratios have been studied and tabulated (Aj 77, Aj 72 and En 74). The relative populations of the ground state and the excited states of each residual nucleus have to be estimated theoretically.

The most effective method for calculating the relative population is by the Hauser-Feshbach statistical model (Ha 52). An example of a complete calculation using the computer code "HAUSER*4" (Ma75a, Ma76a) will be described in Chapter III of part II. An analytical estimate for the ^{14}N + ^{10}B reaction will be described in the following section. However, if the energy excess for a particular outgoing nucleus is extremely high, the relative populations of the excited states for this nucleus should be approximately proportional to the statistical weights (2J + 1) of the states (Sw 76). Even when the populations are being calculated by a more sophisticated model, the (2J + 1) weighting provides a quick method to ensure that gross errors have not been made in setting up the supposedly better calculation.

The computer code "SUMM" was used for calculating the summing and branching correction factors. The detailed calculation in II.3.B shows the motivation for this calculation.

Table 3 compares the values of β obtained with the (2J + 1) rule to those obtained with the complete analytic calculation of the relative populations (III.2). In most cases, the two values of β agree within 10%, indicating that the β calculations are nearly model independent. Further details, and the results, of the cross sections calculations are given in the following subsections.

III.2 Analytic Calculation for Relative Cross Sections - Simplified Statistical Model

The partial cross section for <u>formation</u> of a compound nucleus of spin J and parity π, from a projectile and a target nucleus with spin J_P and J_T, at c.m. energy E, is given by (Pü 77)

$$\sigma(J^{\pi}) = \pi\lambda\!\!\!^{-2} \frac{2J+1}{(2J_P+1)(2J_T+1)} \sum_{S=|J_P-J_T|}^{J_P+J_T} \sum_{\substack{L=|J-S| \\ (\pi)}}^{J+S} T_L(E) \qquad \text{(III-1)}$$

The transmission coefficients T_L are assumed to depend only on energy and the orbital angular momentum L; $\vec{S} = \vec{J}_P + \vec{J}_T$ is the channel spin. The summation over L is restricted by the parity rule, $\pi = \pi_P \pi_T (-)^L$.

The expression for the <u>particle emission</u> probability is derived from the inverse cross sections, written in terms of transmission coefficients, by using the reciprocity theorem (Ha 52). The probability P_x for emitting a particle χ from an excited nucleus 1, which has excitation energy E_1, spin J_1, parity π_1, to form a product nucleus 2 which has excitation energy, E_2, spin and parity J_2 and π_2 is

$$P_x = \frac{\displaystyle\sum_{S=|J_2-S_x|}^{J_2+S_x} \; \sum_{\substack{L=|J_1-S| \\ [\pi]}}^{J_1+S} T_L^{\,x}(\varepsilon_x)}{\displaystyle\sum_y \left[\sum_{S'=|J_2'-S_x'|}^{J_2'+S_x'} \; \sum_{\substack{L'=|J_1-S'| \\ [\pi]}}^{J_1+S'} T^y_{L'}(\varepsilon_y) \right]} \qquad \text{(III-2)}$$

where ε_x is the kinetic energy of particle x, S_x is the spin of particle x, $\vec{S} = \vec{J}_2 + \vec{S}_x$ is the channel spin, and y is summed over all possible final states resulting from breakup of the compound nucleus.

Putting these two equations together, the cross section $\sigma_{\alpha\beta}$, with α for the incoming channel and β for the outgoing channel, is

$$\sigma_{\alpha\beta} = \frac{\pi\lambda\!\!\!^{-2}}{(2J_P+1)(2J_T+1)} \sum_{\substack{J^\pi \\ L,L',L''}} \frac{(2J+1)\, T_{L,\alpha}\, T_{L',\beta}}{\sum_{\gamma} T_{L''\gamma}} \qquad \text{(III-3)}$$

When a reaction has high enough Q-value, the heavy residual nucleus, resulting from the emission of one light particle, may still be populated up to a sufficiently high excitation energy that another light particle can be emitted. In this case, the statistical model calculation has to be carried out as a multi-stage process. Although no more than a three-stage calculation is needed for $^{14}N + ^{10}B$, a complete calculation would be very costly because of the very large Q-value and the large number of open channels. Such a calculation has been done, however, for $^{16}O + ^{16}O$; the details will be given in Chapter III of part II.

Transmission coefficients for the exit channels were calculated from the optical model using the potential parameters of Bechetti and Greenlees for protons and neutrons (Be 69), and of McFadden and Satchler for α-particles (Mc 66). The forms of the potentials assumed for the exit channels are summarized in Table 4, and the potential parameters are tabulated in Table 5.

Expressions for the level densities $\rho(E)$ and $\rho(E,J)$, which are required to evaluate the relative transition probabilities to excited states in the continuum , are summarized in Chapter III of part II. The values of the level-density parameters used in the present work are given in Table 6.

III.2.A Evaporation Residues from Single-particle Evaporation

Table 7 shows an example of the relative populations of the ground state and the excited states for the $^{16}O + {}^{16}O$ reaction, after the emission of one α-particle. The reaction Q-value is 9.59 MeV, the center of mass incident energy is 6.0 MeV, and the outgoing energy excess is 15.59 MeV for the ground state and 14.21 MeV for the 1st excited state, etc. Column 5, which shows the ratio of the cross section divided by (2J + 1) for each of the final states to the cross section divided by (2J+1) for the ground state, is expected to approach unity since the available outgoing energy and the compound nucleus excitation energy are both extremely high. The systematic decrease of this ratio with increasing excitation energy of the residual nucleus (^{28}Si) is due to the decrease in the transmission coefficients when the outgoing particle energy becomes lower. It is also desirable to evaluate the effect of calculating the transmission coefficients properly on obtaining the relative populations for the residual nuclei in the $^{14}N + {}^{10}B$ reactions.

The residual nuclei ^{23}Mg, ^{23}Na and ^{20}Ne can be formed by evaporation from the ^{24}Mg compound system of a neutron, proton, or α-particle, respectively. The relative populations $R_1(J_i)$ of the bound states in the final nuclei were calculated as

$$R_l(J_i) = (2J_i + 1)\, T_l \quad , \qquad \text{(III-4)}$$

where J_i is the spin of the i^{th} final state and T_l is the sum over orbital angular momenta of the transmission coefficients for particles of the appropriate type and energy. The transmission coefficients were calculated with the statistical model code "HAUSER*4" (Ma 75a, Ma 76a). The relative populations determined in this way differ from those obtained from the (2J +1) rule alone mainly by the decrease in relative importance of highly excited states. In Eq.(III-4), it is implicitly assumed that the contributions to T_l from increasing orbital angular momenta can be summed until the contributions from higher ℓ-values are negligible without being limited by the available J-values of the ^{24}Mg compound nucleus. Because of the very high compound nucleus excitation, this assumption should cause no significant error.

Final states with excitation energies up to 3.8 MeV in ^{23}Mg and 4.8 MeV in ^{23}Na were considered. These limitations are imposed by a lack of knowledge of the spins and branching ratios of higher excited states. Since ^{23}Mg β-decays with a 9% branch to the first excited state of ^{23}Na, with a lifetime short compared with the lengths of the data accumulation runs, the ^{23}Na cross sections deduced from the 440 keV γ-ray yield should be decreased by 9% of the ^{23}Mg cross sections. However, since the ^{23}Mg yields are only about 20% of the combined ^{23}Na + ^{23}Mg yields, the correction is very small. The relatively small probability of single neutron evaporation has been noted before by Switkowski, et al (Sw 77a).

States in ^{20}Ne up to 9.12 MeV were considered in the calculations of β for this nucleus. Except for the unnatural parity states at 4.97 (2^-) and 7.01 (4^-) MeV, it is possible for states of excitation above 4.73 MeV to decay by α-emission to the ground state of ^{16}O. For the higher states, $R_1(J_i)$ was therefore multiplied by the ratio of the transmission coefficients for E1 plus M1 γ-decay to the sum of the transmission coefficients for γ-decay and α-decay of the appropriate angular momentum. One result of this competition between α- and γ-decay is that states in ^{20}Ne above 7.2 MeV contribute only a few percent to the total ^{20}Ne production cross section.

The cross section results calculated by equation (II-5) are shown in Fig. 11 and tabulated in Table 9. The overall systematic uncertainty in these results is estimated as ±15%, resulting from the quadratic combination of 5% uncertainties in beam current integration, target ^{10}B content, and photopeak detection efficiency, with a 10% uncertainty in the β values. The statistical uncertainties in the cross sections at low energies are indicated in Fig. 11. At higher energies these uncertainties are roughly ±15% for ^{23}Mg, ±4% for ^{23}Na and ±10% for ^{20}Ne.

III.2.B Two-particle Evaporation Residues

The nuclei ^{23}Mg, ^{23}Na and ^{20}Ne may be formed at sufficiently high excitation energies that a second particle can be evaporated. The relative probability for these processes was taken as

$$R_1(Ex_1) = T_1\rho(Ex_1)\Delta Ex_1 \qquad \text{(III-5)}$$

where $\rho(Ex_1)\Delta Ex_1$ is the number of states with excitation energy between Ex_1 and $Ex_1+\Delta Ex_1$. Particle emission from these states can populate bound states of ^{19}F, ^{19}Ne, ^{22}Ne, ^{22}Na, ^{22}Mg and ^{16}O. To calculate the relative populations $R_2(J_f)$ of these states, Eq. (III-5) was multiplied by $(2J_f+1)T_2$ where T_2 is the transmission coefficient (summed over orbital angular momenta) for emission of the second particle, and J_f is the spin of the final state. The product is summed over particle-unstable excitation energies of the intermediate system with the result,

$$R_2(J_f) = \sum_{Ex_1} T_1\rho(Ex_1)\Delta Ex_1\, T_2\, (2J_f+1) \qquad \text{(III-6)}$$

The number of discrete states considered in the evaluation of Eq. (III-6) for each residue is indicated in Table 3. For the two-particle exit channels ^{19}F $+\alpha+$ p, ^{19}Ne $+\alpha+$ n and ^{22}Na + p + n, particles 1 and 2 may be emitted in either order. For these cases Eq. (III-6) was evaluated for both possibilities and the results were added. The relative population of the ground state of ^{16}O was calculated by evaluating Eq. (III-6) for $Ex_1>9.1$ MeV and adding the population from the α-decay of the lower energy discrete states in ^{20}Ne, calculated as previously described.

With the exception of ^{22}Mg, γ-rays characteristic of all the two-particle evaporation residues were observed. Failure to observe the ^{22}Mg + 2n channel is not surprising in view of the relatively small probability for single neutron evaporation and the small number of particle-stable states in ^{22}Mg. In any event, since ^{22}Mg quickly decays to excited states of ^{22}Na, the ^{22}Mg production cross sections will be included in those for ^{22}Na production which were deduced from the yields of 583 keV γ-rays.

The results of the cross section calculations for the production of two-particle evaporation residues are shown in Fig. 12 and tabulated in Table 9. Systematic uncertainties in these results are estimated to be ±18% for ^{22}Na and ±15% for the others. The higher figure for ^{22}Na reflects an additional 10% uncertainty arising from the uncertainty in the ^{12}C target impurity. Statistical uncertainties at low energies are indicated in Fig. 12. At higher energies, the statistical uncertainties were approximately ±6% for ^{16}O, and less than ±3% for the other channels.

III.3 Bound State Fractions

Although it is energetically possible for additional particles to be evaporated, no γ-radiation characteristic of three-particle evaporation residues was detected with the exception of ^{21}Ne. In calculating the total fusion cross sections as the sum of the cross sections for individual residue nuclei, however, three-particle evaporation residues should be included.

The relative probability that the residues from two-particle evaporation are formed in particle-unstable states was approximated by

$$R_2(Ex_2)= \sum_{Ex_1} \sum_{Ex_2} T_1\rho(Ex_1)\Delta Ex_1 T_2\rho(Ex_2)\Delta Ex_2 \langle 2J_f+1\rangle \quad , \qquad \text{(III-7)}$$

where $\rho(Ex_2)\Delta Ex_2$ is the number of states in the two-particle evaporation residues with excitation energy between Ex_2 and $Ex_2+\Delta Ex_2$. At each center-of-mass energy the summations are taken over the excitation energies consistent with energy conservation. The average weighting factor $\langle 2J_f+1\rangle$ was calculated following the procedure given in Chapter III of part II. Thus,

$$\langle 2J_f+1\rangle = \int \rho(Ex_2,J_f)(2J_f+1)dJ_f \Big/ \int \rho(Ex_2,J_f)dJ_f \quad , \qquad \text{(III-8)}$$

and took values between 4.5 and 5.5 for all cases considered here.

The contributions of the three-particle evaporations were included in the cross sections for production of two-particle evaporation residues by dividing the latter by

$$F = \frac{\Sigma_f R_2(J_f)}{R_2(Ex_2) + \Sigma_f R_2(J_f)} \qquad \text{(III-9)}$$

This factor F represents the probability that when a two-particle residue is formed, it is formed in a state which cannot decay by particle emission. The values of F calculated for ^{19}Ne and ^{22}Ne differ from unity by only a few percent at the very highest center of mass energies. The values of F for ^{19}F vary more strongly with energy and are shown in Fig. 13.

The calculated bound state fractions for ^{16}O are also shown in Fig. 13. These were calculated by explicitly treating as bound states the five unnatural parity states in ^{16}O between 10 and 13 MeV. For the unbound states, Eq. (III-7) was evaluated with the actual observed number of states in each interval ΔEx_2, rather than a parameterized density of states. The small values of the deduced bound state fraction at higher energies imply that triple α-particle evaporations should contribute significantly to the total fusion cross section. This is disturbing since 4.43-MeV γ-rays from the $^{12}C + 3\alpha$ channel were not observed.

The bound state fractions for ^{16}O were therefore calculated in several different ways. First, several parameterizations for the density of states in ^{20}Ne were used without significantly altering the results shown in Fig. 13. Second, parameterized densities of states in ^{16}O above 9-MeV excitation were used in Eq. (III-7) to calculate the relative populations of continuum states. It was assumed that only half of these states have natural parity and only half the calculated relative population was therefore used as $R_2(Ex_2)$ in Eq. (III-9). The other half was added to the sum of relative populations of bound states, taken as all states below 9-MeV excitation. The results of the two calculations agree at the lowest bombarding energies. As energy increases, the second calculation yields larger values of the bound state fraction. At

$E_{c.m.}$=6.0 MeV, the discrepancy is 10%, and at 7.5 MeV the discrepancy is 20%. A comparison of these calculations is shown in Table 8.

The case of ^{21}Ne, which may be formed by proton evaporation from ^{22}Na, provides another way of checking the calculations of the bound state fractions. The yield of 351 keV γ-rays was used to deduce ^{21}Ne production cross sections. Values of β were calculated assuming successive proton and deuteron evaporation from ^{24}Mg. These cross sections are also shown in Fig. 12 and Table 9. The sum of ^{21}Ne and ^{22}Na production cross sections was compared with ^{22}Na cross sections corrected for additional particle evaporations by Eq. (III-9). The sum is approximately 10% higher over the entire energy range. Unfortunately, the ±20% uncertainty in the ^{21}Ne cross sections at high energies arising from the uncertainty in ^{12}C target impurity content somewhat vitiates this check on the bound state fraction calculation.

III.4 Total Fusion Cross Sections

Total fusion cross sections were obtained by adding the single-particle evaporation cross sections, and the two-particle evaporation cross sections, corrected for possible three-particle evaporations. The sum of ^{21}Ne and ^{22}Na cross sections was used rather than the corrected ^{22}Na cross sections. The results are given in Table 9 and shown in Fig. 14. At energies above $E_{c.m.}$=4 MeV, uncertainties arising from counting statistics alone are generally

±3%. At lower energies these uncertainties are consistent with the scatter of points. If the corrections for three-particle evaporation are neglected for the moment, systematic uncertainties in the total fusion cross sections should be less than the ±15% uncertainty in the individual reaction cross sections. Three-particle evaporations are calculated to contribute 20% to the total fusion cross section at the highest energy and only a few percent at the lowest. The contributions to the systematic error from three-particle evaporations are difficult to estimate. A 25% error in the calculation of each bound state fraction will be reflected as a 10% error in the fusion cross section at $E_{c.m.}=7.5$ MeV. Except for the three lowest energies where the statistical errors are relatively large, as shown in Fig. 20, the best estimate of the overall uncertainty in the total fusion cross section ranges from ±15% at the lowest energies to ±20% at the highest energies.

III.5 Comparison with Measurements of High and Čujec

High and Čujec (Hi 77a) have also measured the fusion reaction cross sections of $^{14}N + {}^{10}B$ using NaI(Tℓ) crystals from $E_{c.m.}=2.6$ to 6.0 MeV. Figure 14 compares the results of the present measurement of the total fusion cross sections with those of High and Čujec. Near $E_{c.m.}=3$ MeV, our data are approximately 20% higher. This is consistent, however, with the combined estimated uncertainty of 25% for the two measurements. At $E_{c.m.}= 6$ MeV. The present results are 40% higher than those of High and Čujec. The increasing discrepancy between the two sets of measurements may be attributed to our corrections for three-particle evaporations. If we neglect these corrections, our results are consistently higher than those of High and Čujec by 20-25%.

The agreement between cross sections measured by the two different experimental techniques has usually been better than in the present case (Hi 77a). It is likely that much of the discrepancy here stems from the corrections for unobserved transitions, including three-particle evaporations. The number of open three-particle evaporation channels is greater for the $^{14}N + {}^{10}B$ reactions than for the other cases studied by both techniques. High and Čujec make a maximum correction of 10% for all non-radiative transitions, while our corrections for three-body evaporations alone range up to 20%. High and Čujec use a (2J+1) relative population of bound final states to calculate their corrections. This is likely to underestimate the correction for the populations of ground states of evaporation residues since the transmission coefficients for particle evaporation to higher states decrease rapidly with excitation energy, particularly for those channels with small Q-values such as the three-particle evaporation channels.

In addition to determining the excitation function (yield vs energy) for the fusion cross section, it is clear that any other available information will help in understanding the reaction mechanism for heavy ions. Elastic scattering cross sections are relatively easier to measure than fusion cross sections, and contribute strongly to understanding the reaction cross section. Elastic scattering measurements for $^{14}N + {}^{10}B$ are described in the following chapter.

IV. ELASTIC SCATTERING MEASUREMENTS

IV.1 Targets

IV.1.A Target Preparation

Thin "transmission" targets were prepared by electron-beam evaporation of elemental boron, isotopically enriched to 96.2% ^{10}B. For the target employed in the scattering measurements at $\theta_{c.m.}=74.4°$, boron was evaporated onto a $BaCl_2$ -coated glass substrate. A gold layer approximately 2 $\mu g/cm^2$ thick was evaporated over the boron, and the composite foils were floated in water from the substrate onto the target holders.

Since the boron powder available for evaporation was very fine and did not self-adhere very well, the amount of boron that could be put onto the small evaporation container was too small for making good targets. Methanol was used to make the powder adhere better in order to make compressed boron discs. It was assumed that all methanol molecules were evaporated long before the sample was heated to high enough temperature to evaporate boron.

The evaporated boron layer became partially oxidized rather quickly in the air ($\sim$15min.), and became water-soluble boron oxide. It was therefore necessary to mount the self-supporting boron foil targets immediately after the evaporation procedures were finished. However, since the surface barrier detector used for the elastic scattering measurements was able to resolve the ^{14}N ions scattered from thin layers of boron, carbon and oxygen, it was possible to use thin targets containing oxygen and carbon, and thus other target preparation techniques were worth investigating.

For the targets used at $\theta_{c.m.}$=90°, the boron and gold layers were deposited on a glass substrate previously coated with a 5 $\mu g/cm^2$ carbon film. Films of this type, floated onto target holders in the same way as the films discussed in the previous paragraph, were considerably sturdier than those without the carbon films. The thicknesses of the deposited boron layers were monitored continuously during the boron evaporation, and were limited to values between 5 and 15 $\mu g/cm^2$.

IV.1.B Target Thickness Determination by α-scattering

The elemental compositions of the transmission targets were investigated by α-particle elastic scattering measurements at E_{lab}=1.5 MeV and θ_{lab}=60°. The targets were oriented so that the angle between the beam and the target normal was 30°. The scattered α-peaks from ^{10}B, ^{11}B, ^{12}C, ^{16}O and ^{197}Au were clearly resolved in the pulse height spectrum from the solid state detector. The energy and angle dependences of the elastic scattering yields were checked and found to be consistent with pure Coulomb scattering near E_{lab}=1.5 MeV. The Rutherford scattering cross sections were therefore used to deduce the compositions of the targets. To determine the number of incident α-particles, the equilibrium charge state of the α-particle after passing through the target foil is needed, and this was taken from Marion and Young (Ma 68). A typical carbon-backed foil target contained 12.8$\mu g/cm^2$ of ^{10}B, 8.0 $\mu g/cm^2$ of ^{12}C, 3.3 $\mu g/cm^2$ of ^{16}O, and 2.3 $\mu g/cm^2$ of ^{197}Au.

An aperture subtending a solid angle of 1.15×10^{-3} sr was used for the α-scattering detector and also for the proton scattering work of the next subsection. Deviations from the $1/\sin^4\frac{\theta}{2}$ law of Rutherford scattering were less than 2%. The statistical error of the ^{10}B peak was ±10% because of the poorly shaped peaks found in the spectrum.

IV.1.C Target Thickness Determination by p-scattering

The boron and gold contents of one of the targets were also verified in a proton elastic-scattering experiment at E_p=2.2 MeV and θ_{lab}=120°. Previously measured $^{10}B(p,p)^{10}B$ cross sections (Ov 61) were used to deduce the ^{10}B content, and the Rutherford cross section was used to deduce the gold content. The target compositions derived from the α-particle and proton scattering measurements were consistent within ±10%. The proton scattering gave 15.1 $\mu g/cm^2$ ^{10}B and 2.6 $\mu g/cm^2$ ^{197}Au, to be compared with 12.8 $\mu g/cm^2$ ^{10}B and 2.3 $\mu g/cm^2$ ^{197}Au from the α-scattering. Since the previously measured σ/σ_{Ruth} has an error of ±8%, the agreement between the two methods suggests that the target thickness measurements are reliable. A comparison of thick and thin target backings is provided by Fig. 4 (a copper-backed target) and Fig. 15 (a carbon-foil backed target).

The beam charge integration for the thin target measurements, for both α- and p-scattering, was carried out in a Faraday cup biased at +300V. An electron suppressor, biased at -300V, between the cup and the scattering chamber, prevents secondary electrons produced in the scattering chamber from reaching the Faraday cup.

IV.2 Experimental Procedure

All scattering measurements were made in the 61-cm diameter scattering chamber, with the incident beam collimated at the entrance to the chamber. An additional collimator immediately upstream of the target eliminated beam particles scattered from the collimator further upstream, and limited the possible excursions of the beam on the target.

Silicon surface-barrier detectors were used to detect the scattered particles. Two narrow, elliptical apertures were used. The first one, of size $\frac{1}{16}$" by $\frac{3}{16}$" was used to define the solid angle. The second one, of size $\frac{3}{32}$" by $\frac{1}{4}$", located between the first aperture and the detector, served to stop the particles scattered from the edge of the first aperture. The elliptical aperture was oriented so that the total θ angle subtended by the aperture was less than 0.6°, while the larger angle subtended in the ϕ direction increased the counting rate without appreciably broadening the θ resolution.

The angle scale for the detector was checked by observing the positions of the Mott-scattering minima and maximum near $\theta_{c.m.}=90°$ in the yield of ^{16}O ions scattered from the ^{16}O target contaminant, and was known to within ±0.1°.

An example of a detector pulse-height spectrum , obtained with a 16.4 MeV ^{14}N beam incident on a carbon-backed boron target at 35.5° laboratory angle is shown in Fig. 16. Another spectrum obtained with a 17.2 MeV ^{14}N beam incident on a self-supporting boron target at 30.0° laboratory angle is shown in Fig. 17. The peaks were identified by two methods: first, by the dependence of scattered particle energy on target mass for a fixed laboratory angle, and secondly, by the energy dependence on angle for fixed target mass.

The yields of ^{14}N ions scattered from ^{10}B were measured relative to the yields scattered from the gold layer, to avoid any possibility of an energy-dependent beam-current integration error. The uncertainties in the target thickness measurements do not affect the relative yield measurements. Scattering data were taken at $\theta_{lab}=30°$, in 0.2 MeV steps from $E_{lab}=10.5$ MeV to 22 MeV, and at $\theta_{lab}=35.5°$ from 8.0 MeV to 20.0 MeV. In the center of mass system, these angles correspond to 74.4° and 90.0°, respectively, and the center of mass energies range from 4 to 9 MeV.

IV.3 The Differential Cross Sections for Elastic Scattering

As previously noted, the yields Y of ^{14}N ions elastically scattered from ^{10}B were measured relative to those scattered from the gold layer. The ^{10}B differential scattering cross section is therefore

$$\left(\frac{d\sigma}{d\Omega}\right)_{^{10}B} = \frac{Y(^{10}B)}{Y(Au)} \left(\frac{d\sigma}{d\Omega}\right)_{Au} R \quad , \qquad \text{(IV-1)}$$

where R is the ratio of the number of gold atoms to the number of ^{10}B atoms in the target. Since the Coulomb barrier for ^{14}N + ^{197}Au is 66 MeV in the center of mass system, Rutherford scattering cross sections, $\left(\frac{d\sigma}{d\Omega}\right)_{Au}$, were used to describe the elastic scattering from gold.

Figure 18 displays the energy dependence of the ^{10}B scattering cross sections, presented as the ratio to Rutherford scattering. These results have been normalized to the assumed Rutherford scattering at low energies. If the measured ratio R from IV.1.B is used in Eq. (IV-1), the results are 10% higher. This error is consistent with the accuracy of the target thickness measurements determined by proton and α-particle scattering, and is compatible with an estimated systematic uncertainty of ±5% in the results shown. Although the deviation of the data points in Fig. 18 from the smooth curves are consistent with the ±5% statistical accuracy of the data, there is some weak evidence for a small oscillation about the smooth curves.

V. THE INCOMING WAVE BOUNDARY CONDITION (IWBC) CALCULATIONS

V.1 General Description of the IWBC Model

The IWBC model (Ra 63) has been used by Eisen and collaborators (Ei 72, Ei 74) for the analysis of elastic scattering at energies near the Coulomb barrier, and by Christensen and Switkowski for describing both elastic scattering and fusion cross sections for three reactions involving ^{12}C and ^{16}O (Ch 77b).

The basic assumption of the model is that most of the reaction cross section goes into compound nucleus formation, i.e., fusion, and that the direct reactions contribute negligibly (Sw 74). It is therefore possible to avoid the use of an imaginary potential, and instead impose the boundary condition that, at some particular radius R_B in the interior of the interaction region, each partial wave $f_\ell(r)$ is travelling "inwards" only.

The reaction cross section between nucleus Z_1,A_1 and Z_2,A_2 is therefore given by

$$\sigma_r = \pi\lambda\!\!\!^{-2} \sum_\ell (2\ell+1)\, T_\ell \quad , \qquad \text{(V-1)}$$

where $\lambda\!\!\!^{-}$ is the reduced wave length of the entrance channel, and T_ℓ the transmission coefficient corresponding to orbital angular momentum ℓ. T_ℓ is usually calculated by solving the radial Schrödinger equation, i.e.,

$$\frac{\hbar^2}{2\mu}\frac{d^2f_\ell}{dr^2} + \{E - V^\ell_{eff}(r)\}f_\ell = 0 \qquad \text{(V-2)}$$

where $f_\ell(r)$ is the partial wave function corresponding to angular momentum ℓ, μ is the reduced mass of the entrance channel, and E is the center of mass energy. The total effective potential for the ℓth partial wave V^ℓ_{eff} is given by

$$V^\ell_{eff}(r) = V_N(r) + V_c(r) + \frac{\ell(\ell+1)\hbar^2}{2\mu r^2} \quad , \qquad \text{(V-3)}$$

where $V_c(r)$ is the Coulomb potential and $V_N(r)$ is the real nuclear potential, which has been chosen to be of Woods-Saxon form for the present calculations. The local wave number $k_\ell(r)$ at r corresponding to μ,E and angular momentum ℓ is given by

$$E = \frac{\hbar^2 k^2_\ell(r)}{2\mu} + V^\ell_{eff}(r) \qquad \text{(V-4)}$$

Since R_B is the radius at which each partial wave f_ℓ is travelling "inwards" only, the incoming function $f_\ell(r)$ can be written as

$$f_\ell(r) = \frac{A}{\sqrt{k_\ell(r)}} \exp\{-i\int_{R_B}^{r} k_\ell(r)\, dr\} \qquad \text{(V-5)}$$

for $r \simeq R_B$. A is a constant determined by matching to the "external" wave function.

For ℓ=0, the effective potential has a maximum at a certain radius, R_b. As ℓ increases, the radius R_p at which the peak of the barrier occurs increases, and the range of r-values smaller than R_p in which the local wave number $k_\ell(r)$ can be real for high enough energy becomes smaller. The lowest value of ℓ for which $k_\ell(r)$ can no longer be real anywhere except for $r>R_p$ is called ℓ_{crit}. Any partial wave with angular momentum $\ell \geq \ell_{crit}$ cannot form a purely incoming wave, and thus does not contribute to the fusion cross sections. For the reaction cross section determined by Equation (V-1), the summation can only be carried up to an ℓ-value less than ℓ_{crit}.

However, for each center-of-mass energy, there is also a maximum ℓ-value, ℓ_{max}, for which $k_\ell(r)$ can be real somewhere within the potential well. The radius R_B is chosen (within the potential well) so that the W.K.B. approximation is valid, i.e.,

$$2\pi\frac{d(1/k)}{dr} << 1 \quad , \qquad \text{(V-6)}$$

for all $\ell \leq \ell_{max} < \ell_{crit}$ for some radius $r<R_B$. In the present calculations, the condition

$$2\pi\,\frac{d(1/k)}{dr} < 0.5 \qquad \text{(V-7)}$$

was used. R_B was thus chosen to be the largest radius within the potential well for which the WKB validity condition was fulfilled for all ℓ-values which make significant contributions to the cross section.

The radial Schrödinger equation (V-2) was integrated numerically outwards to a large radius R, at which the internal wave function was matched to a pure Coulomb wave function. The Coulomb wave function ψ_ℓ at R is given by

$$\psi_\ell(R) = F_\ell(R)+iG_\ell(R) + S_\ell[F_\ell(R) - iG_\ell(R)] \quad , \tag{V-8}$$

where F_ℓ, G_ℓ are the regular and irregular Coulomb functions. S_ℓ is the complex scattering-matrix element which is related to the transmission coefficients by

$$T_\ell = 1 - |S_\ell|^2 \quad . \tag{V-9}$$

S_ℓ can be calculated by matching $f_\ell(R)$ to $\psi_\ell(R)$, and $f'_\ell(R)$ to $\psi'_\ell(R)$ (the prime means the radial derivative).

$$S_\ell = \frac{f_\ell(R)[F'_\ell(R)+iG'_\ell(R)] - f'_\ell(R)[F_\ell(R)+iG_\ell(R)]}{f'_\ell(R)[F_\ell(R)-iG_\ell(R)] - f_\ell(R)[F'_\ell(R)-iG'_\ell(R)]} \tag{V-10}$$

For very small value of T_ℓ, this matching procedure may no longer be reliable because of rounding-off errors in the computation. Since $S_\ell \approx 1$, when T_ℓ is small, equation (V-8) can be approximated as

$$\psi_\ell(R) \simeq 2F_\ell(R) \quad . \tag{V-11}$$

The ingoing current density at $r=R_B$, $j_\ell(R_B)$ is given by

$$j_\ell(R_B) = k_\ell(R_B)\,\frac{|f_\ell(R_B)|^2}{|f_\ell(R)|^2}\,|2F_\ell(R)|^2 \quad , \tag{V-12}$$

where $f_\ell(R)$ is the internal wave function determined by integrating the Schrödinger equation. The ingoing current density at large R is given by

$$J_\ell(R) = k_\ell(R)\,[F_\ell(R)^2 + G_\ell(R)^2] \tag{V-13}$$

The transmission coefficient T_ℓ is then given by

$$T_\ell = \frac{j_\ell(R_B)}{J_\ell(R)}$$

$$= \frac{k_\ell(R_B)}{k_\ell(R)} \frac{|f_\ell(R_B)|^2}{|f_\ell(R)|^2} \frac{|2F_\ell(R)|^2}{[F_\ell(R)^2 + G_\ell(R)^2]} \qquad \text{(V-14)}$$

Equation (V-14) was used for $T_\ell \leq 10^{-5}$. For reactions in which the entrance channel consists of two identical bosons, for example, $^{12}C + {}^{12}C$ or $^{16}O + {}^{16}O$, Eq. (V-1) is replaced by

$$\sigma_r = 2\pi\lambda\!\!\!^{-2} \sum_{\ell \text{even}} (2\ell+1)T_\ell \qquad \text{(V-15)}$$

The Woods-Saxon potential

$$V_N(r) = -\frac{V_o}{1 + \exp(\frac{r-R_o}{a})} \qquad \text{(V-16)}$$

was used for the real ion-ion interaction potential. The radius parameter r_o is defined by $R_o = r_o(A_1^{1/3} + A_2^{1/3})$. Since the IWBC model calculates the wave functions only for $r>R_B$, the transmission coefficients are essentially only barrier-dependent. It is also true that the scattering of heavy ions is sensitive mainly only to the tail of the nuclear potential (Ig 59). Thus, the exponential term in the denominator is large compared with 1 and $V_N(r) \approx -V_o \exp(\frac{R_o-r}{a})$. A constant value of 50 MeV has been used for V_o in the present calculations.

The relationship between the radius of ℓ=0 barrier R_b and R_o is given by

$$R_o = R_b - a \ln (k - 1 + \sqrt{k^2 - 2k}) \qquad \text{(V-17)}$$

with

$$k = \frac{R_b^2 V_o}{2Z_1 Z_2 e^2 a} \qquad \text{(V-18)}$$

Therefore, R_b and a may be used as parameters for IWBC calculations instead of R_o and a.

The computer code IWBWS was designed to calculate elastic scattering and fusion cross sections, with r_b and a as input parameters, where r_b is defined by

$$R_b = r_b(A_1^{1/3} + A_2^{1/3}) \qquad \text{(V-19)}$$

V.2 IWBC Calculation for $^{14}N + {}^{10}B$ Elastic Scattering

The differential cross section for elastic scattering between the nuclei (Z_1, A_1) and (Z_2, A_2), with center of mass energy E, is

$$\frac{d\sigma}{d\Omega} = |A(\theta)|^2 \qquad \text{(V-20A)}$$

where $A(\theta)$ is the scattering amplitude given in terms of the scattering matrix S_ℓ and Legendre polynomials by

$$A(\theta) = f_c(\theta) + \frac{1}{2ik} \sum_\ell (2\ell+1)\ (S_\ell - 1)\ e^{2i\sigma_\ell}\ P_\ell(\cos\theta). \qquad \text{(V-21)}$$

For the case that the projectile and the target are identical particles, equation (V-20A) is replaced by

$$\frac{d\sigma}{d\Omega} = \alpha |A(\theta) + A(\pi-\theta)|^2 + \beta |A(\theta) - A(\pi-\theta)|^2 , \qquad \text{(V-20B)}$$

$$\alpha = \frac{S+1}{2S+1} \quad , \quad \beta = \frac{S}{2S+1} \ , \ S=0,1,2\ldots \text{for bosons} \ ,$$

$$\alpha = \frac{S}{2S+1} \quad , \quad \beta = \frac{S+1}{2S+1} \ , \ S=\frac{1}{2},\frac{3}{2} \ldots \text{for fermions.} \qquad \text{(V-22)}$$

In (V-21), f_c is the Coulomb scattering amplitude (Al 66b),

$$f_c(\theta) = - \frac{\eta \exp[-i\eta \, \ln(\sin^2 \frac{\theta}{2}) + 2i\sigma_0]}{2k \sin^2 \frac{\theta}{2}} \quad , \qquad \text{(V-23)}$$

σ_ℓ is the Coulomb phase shift, given by

$$\sigma_\ell = \arg \Gamma(\ell + 1 + i\eta) \quad , \qquad \text{(V-24)}$$

and

$$\eta = \frac{\mu Z_1 Z_2 e^2}{\hbar^2 k} = \frac{Z_1 Z_2 e^2}{\hbar} \left(\frac{\mu}{2E}\right)^{1/2}. \qquad \text{(V-25)}$$

The quantity μ is the reduced mass in the entrance channel.

Satisfactory fits to the elastic scattering data were obtained with R_b = 8.08 fm, corresponding to r_0 = 1.24 fm, and a = 0.50 fm. The results of the calculations are superimposed on the scattering data in Fig. 18. The corresponding potential barrier height is 5.85 MeV, as given by

$$V_b \approx \frac{Z_1 Z_2 e^2}{R_b} \left(1 - \frac{a}{R_b}\right) \qquad \text{(V-26)}$$

which has been derived from

$$V_b = V_N(R_b) + \frac{Z_1 Z_2 e^2}{R_b}$$

To see how sensitively the fit depends on the parameters r_b and a, the calculated differential cross sections are also shown in Fig. 19 for different r_b and a. The center-of-mass energy at which σ/σ_{Ruth} starts to deviate from 1.0 is mainly determined by r_b, while the steepness of the downwards slope of σ/σ_{Ruth} is mainly determined by a.

V.3 IWBC Fit to the Fusion Cross Sections

To reduce the strong energy dependence of fusion cross sections near the interaction barrier, it has become conventional to display the reaction S-factor defined as

$$S = \sigma(E) \quad E \quad \exp(2\pi\eta) \qquad \text{(V-27)}$$

where the Sommerfeld parameter $\eta = \frac{13.32}{\sqrt{E}}(\text{MeV})^{1/2}$ for the present case, and E refers to the center of mass energy. The S-factor for the fusion of ^{14}N and ^{10}B, as calculated from the present cross sections, is shown in Fig. 20. Because the energy dependence of the cross section is diminished in this type of display, structure, if any, in the cross section becomes more evident.

The fusion cross section S-factors calculated with the IWBC parameters R_b = 8.08 fm and a = 0.50 fm are superimposed on the present observations in Fig. 20. The agreement between the calculated and measured S-factors is excellent; the calculation is about 10% lower than the experimental data at 7.5 MeV, and 10% higher at lowest energies.

Since the IWBC model assumes that the main part of the reaction cross section goes into compound nucleus formation, this calculation should provide the most accurate indication of the fusion cross sections at energies near the barrier where the transfer or direct cross section is negligible. A few reactions, in which the transfer cross sections are high, have been studied earlier, $^{18}O + ^{10}B$ (Sw 74), $^{16}O + ^{9}Be$ (Appendix); these reactions have the general property that the transfer reaction dominates the cross sections at very low energies, and the fusion cross section overwhelms the transfer cross section as the energy increases. For the $^{14}N + ^{10}B$ reaction, transfer reactions appear to be of no importance, probably because of their non-optimum Q-values (Sw 74), since no γ-ray peak with energy corresponding to possible transfer reactions was found during the experiment. The IWBC calculation is thus expected to fit the fusion cross sections at least near the barrier. The divergence in slope between the calculations and experimental results above $E_{c.m.} = 6$ MeV (with the calculated results lower) may be evidence that we have overestimated the corrections for three-particle evaporations.

The discrepancy between the measurements and calculated cross sections at low energy region is understandable however, since the inelastic scattering process is not included in either of the measured cross sections. By conservation of flux, the calculated cross sections should be higher than the measured fusion cross sections by an amount corresponding to the inelastic scattering cross section. The cross section for Coulomb excitation was calculated to be approximately 78 μb at $E_{c.m.}$ = 3.97 MeV (II.2.B) while the fusion cross sections is 564 μb at the same energy.

Cross sections calculated for different parameters r_b and a are shown in Fig. 21. The absolute magnitude of the reaction S-factor depends strongly on the parameter r_b, while the shape of the energy dependence of the S-factors depends more on the diffuseness a.

VI. DISCUSSIONS AND CONCLUSIONS

VI.1 The $^{14}N + ^{10}B$ Fusion Cross Sections

The discrepancy between the present fusion cross sections and the work of High and Čujec (Hi 77a) has been noted above. The fusion cross sections measured previously with both NaI crystals and Ge(Li) detectors agree rather well for $^{12}C + ^{16}O$ (Ču 76, Ch 77a) and $^{12}C + ^{10,11}B$ (Hi 77a, Da 76a). However, the reaction Q-values for forming the compound nucleus are 16.75 MeV (for $^{12}C + ^{16}O$), 17.22 MeV (for $^{12}C + ^{10}B$) and 18.20 MeV (for $^{12}C + ^{11}B$). None of these three reactions has the possibility of three-particle evaporation. $^{14}N + ^{10}B$ populates the compound nucleus ^{24}Mg at an excitation energy of 28.25 MeV, and there are several open three-particle channels, $^{12}C + 3\alpha(Q=7.64$ MeV), $^{15}N + 2\alpha p(Q=2.68$ MeV), and $^{21}Ne + ppn(Q=-2.00$ MeV). Serious problems arise in estimating the non-radiative-transition corrections.

High and Čujec (Hi 77a) reported optical model fits to ten sets of fusion and elastic scattering cross sections for the reactions involving boron nuclei. One set, with a real potential well depth of 50 MeV, provided satisfactory fits to all of their data except their $^{14}N + ^{10}B$ fusion cross sections, for which the calculated cross sections were about 20% too high. This particular optical model calculation fits the present data well at 3 MeV, and lies between the present data and those of High and Čujec at 6 MeV.

The limited available evidence suggests that High and Čujec may have underestimated their non-radiative transition corrections, while we may have overestimated the three-particle evaporation corrections since no γ-ray peak from the first excited state of ^{12}C was observed (see III.3). More complete statistical model calculations of $^{14}N + {}^{10}B$ may not even resolve this problem, since the cross sections for α-emission predicted by statistical model calculations always seem to be too low compared with those of p- and n-channels. This means that it is very difficult to make a reliable estimate of the bound state fractions (III.3). The most sophisticated statistical model computer code available at present, "HAUSER*4", does not have the capability for calculating the cross sections for emitting three light particles.

More reliable measurements of fusion cross sections near the barrier can probably be performed by measuring the heavy fusion residues such as ^{23}Na, ^{20}Ne, ^{19}F, etc., although this is expected to be a very difficult measurement because of the large variety of residue particles, small cross sections, and especially some of them with extremely low energies. It appears to be well worthwhile to test the validity of the IWBC model more stringently by trying to obtain more reliable cross sections.

VI.2 The $^{14}N + {}^{10}B$ and $^{12}C + {}^{12}C$ Reactions

Fig. 20 shows the S-factors for the $^{14}N + {}^{10}B$ and $^{12}C + {}^{12}C$ reactions. Clearly, there is no structure in the $^{14}N + {}^{10}B$ fusion

S-factors of magnitude comparable with that shown by the $^{12}C+^{12}C$ reaction. This conclusion, which agrees with the observation of High and Čujec (Hi 77a), is not completely unexpected because of the high excitation energy in the ^{24}Mg compound nucleus and the nature of the interacting nuclei.

There are several major differences between the $^{14}N + ^{10}B$ and $^{12}C + ^{12}C$ reactions. $^{14}N + ^{10}B$ populates the compound nucleus at very high excitation energy, 15 MeV higher than $^{12}C + ^{12}C$. The open exit channels for $^{12}C + ^{12}C$ are α, p, and 2α, at zero center of mass energy. For the sub-Coulomb-barrier energy region (E_B=5.85 MeV for $^{14}N + ^{10}B$, and 6.02 MeV for $^{12}C + ^{12}C$), the number of open channels is much smaller for $^{12}C + ^{12}C$. It is possible that the resonances in $^{12}C + ^{12}C$ reaction reflect the behavior of rotational band in the ^{24}Mg nucleus (Ci 77). Since the level density in the compound nucleus ^{24}Mg formed by the $^{14}N + ^{10}B$ reaction is so much higher, it is reasonable to expect that any resonant structure will be averaged out.

A further difference between the $^{14}N + ^{10}B$ and $^{12}C + ^{12}C$ entrance channels is in the range of spins and parities in the compound nucleus formed by the reactions. For $^{12}C + ^{12}C$, because we have identical spinless bosons, only states of even spin and parity can be formed, while for $^{14}N + ^{10}B$, with spin and parity 1^+ and 3^+ for projectile and target, respectively, the compound nucleus can be formed with any spin and with even or odd parity. For some particular outgoing channels,

α + ^{20}Ne (g.s.) for example, only even ℓ-waves are allowed in the ^{12}C + ^{12}C reaction, while both even and odd orbital angular momenta are allowed for the ^{14}N + ^{10}B reaction.

Finally, there are some obvious differences in the internal structure of the reacting nuclei in the two reactions. It has been proposed that the ^{12}C nucleus has a large component of 3-α structure, and that the α-particle sub-structure becomes excited without being totally destroyed in reactions involving ^{12}C nuclei (Mi 72, Mi 73). This was used as an argument by Michaud for explaining the low energy S-factor trends of ^{12}C + ^{12}C, ^{12}C + ^{16}O, and ^{16}O + ^{16}O as "penetration under the barrier". Since the present experimental evidence does not require Michaud's penetration under the barrier, it consequently does not require α-structure of ^{12}C for this reason. There is much evidence that ^{12}C does have a 3-α structure from the Hartree-Fock calculations which have been carried out at Oak Ridge and elsewhere. It would be surprising if the sub-structure of the reacting nuclei did not have important effects on the kind of compound nucleus intermediate structure that could be formed, since one would expect that ^{10}B and ^{14}N would have many more nucleons free to readjust position as the nuclei coalesce than ^{12}C + ^{12}C.

PART II

FUSION CROSS SECTION MEASUREMENTS FOR THE REACTION $^{16}O + ^{16}O$

I. INTRODUCTION

I.1 The $^{16}O + {}^{16}O$ Reactions in Astrophysics

In the theory of nucleosynthesis, nuclear burning proceeds from hydrogen burning, the conversion of the most abundant element hydrogen to helium, to helium burning, the conversion of helium to carbon and oxygen, and then to the production of the heavier elements. The reactions responsible for the syntheses of ^{12}C and ^{16}O in helium burning are mainly the following : $3\alpha \rightarrow {}^{12}C$, $^{12}C(\alpha,\gamma)^{16}O$ and $^{16}O(\alpha,\gamma)^{20}Ne$. The relative rates of these three reactions at the appropriate effective interaction energies determine the relative abundances of carbon, oxygen, and neon left in the core at the end of helium burning. If the $^{12}C(\alpha,\gamma)$ rate is low compared with the $3\alpha \rightarrow {}^{12}C$ rate, a large ^{12}C fraction will remain at the end of helium burning; if the $^{12}C(\alpha,\gamma)^{16}O$ rate is fast enough, the end-product of helium burning will be ^{16}O, since the $^{16}O(\alpha,\gamma)^{20}Ne$ reaction rate is believed to be relatively small.

Following the evolutionary path of a star after core helium burning is completed, the core will contract, converting gravitational energy to heat until the temperature is high enough for further reactions to take place. Whether these reactions will happen explosively or quiescently depends on many factors, such as the mass of the star, the amount and the type of nuclei present, etc.

For stars in intermediate mass region, $4 < M/M_{\odot} < 10$, Arnett and Truran (Ar 69) have considered the evolution of a core consisting of comparable amounts of oxygen and carbon. High enough temperatures and pressures can be obtained in the core to ignite first the $^{12}C + ^{12}C$ reactions, and at higher temperatures the $^{16}O + ^{16}O$ reactions. The resultant energy production may trigger a great enhanced helium burning rate in a shell around the carbon-oxygen core and produce a rapid C-N-O cycle at the appropriate level in the star. The total energy output is calculated to be sufficient to give most or all of the material in the star escape velocity within a very short interval of time, i.e. the star will probably explode at this stage of evolution.

On the other hand, for a sufficiently massive star ($M/M_{\odot} > 10$), when the temperature becomes high enough ($\sim 6 \times 10^{8}$ °K), the $^{12}C + ^{12}C$ reactions will proceed. The α-particles, protons and neutrons produced by these reactions will react rapidly with the recoil products ^{20}Ne, ^{23}Na, ^{23}Mg, as well as with the unburned carbon and oxygen. In particular, $^{12}C(p,\gamma)^{13}N(\beta^{+})^{13}C$ and $^{13}C(\alpha,n)^{16}O$ produce more oxygen atoms rapidly. As the ^{12}C fuel becomes exhausted, and higher temperatures ($\sim 10^{9}$ °K) are reached, oxygen burning may proceed and this leads to reaction products such as ^{24}Mg, ^{27}Al, ^{28}Si, etc., which can be processed later in silicon burning. Eventually, of course, such a massive star must explode, possibly leaving a neutron star remnant.

For the reactions involved in nucleosynthesis, it is usually impossible to measure the cross sections at the energies appropriate for a star with presently available techniques, because the reaction rates are too low at these energies. The experimental cross sections must often be extrapolated down many orders of magnitude below the lowest measured point. For example, the reaction $^{12}C(\alpha,\gamma)^{16}O$ takes place at $T \simeq 2 \times 10^8$ °K (kT = 20 keV), and the most effective energy is 300 keV (c.m.), while the lowest energy for which the cross section has been measured was E_{cm} = 1.41 MeV (Dy 74). Although fusion cross sections for the $^{12}C + ^{12}C$ reactions have been measured down to E_{cm} = 2.5 MeV, the extrapolation to lower energy of the energy-averaged cross section remains ambiguous and the resonant structure in the S-factor leads to further ambiguities in the low energy S-factors.

In the case of the $^{16}O + ^{16}O$ reactions, the astrophysically interesting temperatures range from about 10^9 °K to 4×10^9 °K, and the cross sections are needed over an energy range of $E_{cm} \simeq 4$ to 14 MeV. The reaction cross sections have been measured by Spinka and Winkler from E_{cm} = 6.8 to 11.9 MeV (Sp 74). The fusion S-factor deduced from their cross sections varies smoothly as a function of energy, in contrast with that of the $^{12}C + ^{12}C$ reactions. Extrapolation of reaction cross sections may be somewhat less ambiguous because of the absence of resonances.

I.2 Measurements of $^{16}O + ^{16}O$ by Other Authors

As noted above, the $^{16}O + ^{16}O$ fusion cross sections have been measured by Spinka and Winkler (Sp 74) from 6.8 to 11.9 MeV in the center-of-mass frame. Particle measurements (α-particles and protons) were performed at several energies to give the fusion cross sections. Relative gamma-ray yields were also measured with a NaI scintillation counter over the same energy region, and then normalized to the cross section determined by particle counting at E_{cm} = 9.85 MeV. Their data are ambiguous since the fusion cross section near 7 MeV center of mass as determined by the relative γ-ray yields measurements was higher than that determined from the particle measurement at 7 MeV by approximately 40%.

Stokstad et al (St 76) have performed standard optical model calculations with V = 50 MeV, W = 10 MeV, r_o = 1.27 fm, a = 0.40 fm for the heavy-ion fusion S-factor over a 6 MeV energy interval around the interaction barrier, for nine different pairs of heavy ions. The parameters listed are those for a Woods-Saxon potential

$$V_N = \frac{-(V_o + iW_o)}{1 + e^{-(\frac{r - R_o}{a})}} , \qquad \text{(I-1)}$$

where $R_o = r_o(A_1^{1/3} + A_2^{1/3})$. The results, shown in fig. 1 of reference St 76, suggest that the measured $^{16}O + {}^{16}O$ fusion S-factors are much too high compared with other reactions.

More recently, Christensen and Switkowski (Ch 77b) have made a systematic study of the ability of incoming-wave boundary-condition (IWBC) calculations to fit both elastic scattering cross sections and fusion S-factors for the astrophysically important reactions $^{12}C + {}^{12}C$, $^{12}C + {}^{16}O$ and $^{16}O + {}^{16}O$. For each reaction, the IWBC parameters r_b and a (see chapter V of part 1) were determined by fitting the elastic scattering measurements of Spinka and Winkler (Sp 74), and the same set of parameters was used to calculate the fusion reaction S-factors. Good agreement between the measured and calculated

S-factors was obtained for both $^{12}C + ^{12}C$ and $^{12}C + ^{16}O$. For the case of $^{16}O + ^{16}O$, however, the measured fusion S-factors were higher than the results of the IWBC calculation by about 50%.

There are several possibilities:first, the $^{16}O + ^{16}O$ elastic scattering cross sections could be wrong. However, Christensen and Switkowski (Ch 77b) remeasured the elastic scattering cross sections for $^{16}O + ^{16}O$ over part of the range and agreed well with Spinka and Winkler (Sp 74). Secondly, the $^{16}O + ^{16}O$ fusion measurements could be wrong. Thirdly, the behavior of $^{16}O + ^{16}O$ could be anomalous for some as yet unknown reason,and not predictable by either the IWBC model or the optical model.

Fusion cross sections for the $^{16}O + ^{16}O$ reactions have been measured at still higher energies by using a Ge(Li) detector, by Kolata et al (Ko 77), and by Cheng et al (Ch 78a). The measured fusion cross sections for $E_{cm} \simeq 12.0$ MeV were lower by about a factor of two than those of Spinka and Winkler (Sp 74). The importance of the $^{16}O + ^{16}O$ reactions in astrophysics, in addition to the puzzle of the discrepant absolute cross sections, motivated the present measurements of $^{16}O + ^{16}O$ fusion cross sections near the Coulomb barrier.

Figure 22 shows the reaction Q-value for the energetically allowed channels in the $^{16}O + ^{16}O$ reactions. Compared with $^{12}C + ^{12}C$ (fig. 2) or $^{12}C + ^{16}O$ (Ču 76, Ch 77a), many more outgoing channels are open. In the present experiments, a large Ge(Li) detector was used to measure the fusion cross sections for the $^{16}O + ^{16}O$ reactions.

The cross sections for emitting α-particles, protons, neutrons, and two light particles sequentially together with the total fusion cross sections, were measured from E_{cm} = 7.0 MeV to 12.0 MeV. The results of the present measurements are compared with previous measured cross sections(Sp 74, Ko 77 and Ch 78a) in chapter V.

II. FUSION MEASUREMENTS

II.1 Experimental Set-Up

The details of the experimental set-up have been described in chapter II of part 1. Only the major points will be reviewed here.

An ^{16}O beam from the ONR-CIT tandem accelerator was magnetically analyzed, and bombarded the oxygen-containing target. The prompt γ-rays from the target were counted with a 73 cm^3 Ge(Li) detector located at 0°, about 1 cm from the target. A thin sheet of lead, of thickness 0.35 cm, was inserted between the target and the detector to attenuate very low-energy x-rays and γ-rays of no immediate interest. The detector was shielded with at least 10 cm of lead in all directions. Gamma-ray excitation functions (yield versus energy curves) were measured for ^{16}O beams with laboratory energies covering the range from 14.0 MeV to 24.0 MeV. The beam intensity used varied from about 2 μA at the lowest energies to about 20 nA at the highest energy. Data were acquired with both increasing and decreasing bombarding energies to check for carbon build-ups on the target. No delayed activities formed in the $^{16}O + ^{16}O$ reactions produce detectable γ-rays, since every unstable residual nucleus produced in the fusion of $^{16}O + ^{16}O$ decays into the ground state of its daughter nucleus (En 74). Occasional beam-off spectra were measured, nevertheless, to ensure that no correction was needed for any residual activities, or natural-background γ-rays.

II.2 Experimental Procedure

II.2.A γ-ray Identification

Fig. 23 shows a typical spectrum obtained at 0° with a thcik quartz target. Identification of the observed γ-rays was one of the difficulties encountered in this experiment. Doppler effects were frequently important since the lifetimes (typically $\sim$ 500 fs) of many first excited states from the residual nuclei were comparable with the stopping time of the heavy residual nuclei in the quartz. One spectrum was accumulated with the Ge(Li) detector at 90° to observe the unshifted γ peaks to assist in their identification.

Peaks were found at 1779 keV from ^{28}Si, 1248 keV from ^{31}S, 709 keV and others from ^{30}P, 844 keV and 1014 keV from ^{27}Al, 1369 keV from ^{24}Mg, 3498 keV from ^{30}Si, and at 1264 keV and 2234 keV, which will be discussed below. Spectra were also accumulated with lower amplifier gain, to ensure that the spectra contain no γ-ray of higher energy with significant intensity.

The γ-ray peak at or near 1264 keV can be attributed to γ-rays from various sources: (1) 1266 keV from p + ^{31}P, (2) 1263 keV from p + p + ^{30}Si and (3) 1264 keV from p + n + ^{30}P. Since the 1973 keV state of ^{30}P decays 41% to the ground state and 59% to the 709 keV state (En 74), it is possible to calculate the yield of 1264 keV γ-rays from the observed yield of 1973 keV γ-rays:

$$\begin{aligned} Y_{1973} &\propto 0.41\ \mathrm{Eff}^{p}(1973) + 0.59\ \mathrm{Eff}^{p}(1264)\ \mathrm{Eff}^{p}(709) \\ Y_{1264} &\propto 0.59\ \mathrm{Eff}^{p}(1264) \times (1 - \varepsilon^{t}_{709}), \end{aligned} \qquad \text{(II-1)}$$

where Eff^p is the photopeak efficiency and ε^t is the calculated total efficiency for the Ge(Li) detector. The possibility of simultaneous detection of both γ-rays from the 709 - 1264 keV cascade by the Ge(Li) detector is included in eq. (II-1).

Similar calculations were made for the yield of the 1263keV γ-ray from ^{30}Si, produced in the cascade decay of the 3498 keV state through the 2235 keV state. The branching ratio of the 3498 keV state for decay through the 2235 keV state is 53%, while the other 47% of the decays go to the ground state of ^{30}Si. The contributions of 1264 keV γ-rays were 12% from ^{30}P and 20% from ^{30}Si at the highest energy studied, and decrease to less than 10% total from both nuclei at 14.0 MeV incident energy. The possibility of Coulomb excitation on the 4.7% of ^{29}Si in quartz by the ^{16}O beam was considered, but the calculated Coulomb excitation yield of the 1273 keV state was less than 2% of the observed yield at E_{lab}= 14.0 MeV, and thus no correction was made for Coulomb excitation. The yield of 1266 keV γ-rays from ^{31}P was therefore used to determine the cross section for the reaction $^{16}O + {}^{16}O \rightarrow p + {}^{31}P$.

The γ-ray peak at or near 2234 keV may contain contributions of γ-rays as follows: (1) 2232 keV from ^{31}S, (2) 2234 keV from ^{31}P and (3) 2235 keV from ^{30}Si. The yields from ^{31}S and ^{31}P were calculated from the relative populations of the first and second excited states, by the statistical model calculation described in chapter III, with the assistance of measured photopeak efficiencies. Previous measurements of the reaction $^{14}N + {}^{10}B$ established that the cross sections deduced from different γ-rays of the same residual nucleus agree usually within about ± 10%. The 2236 keV γ-ray yields from ^{30}Si were therefore used to determine the production of $^{16}O + {}^{16}O \rightarrow p+p+ {}^{30}Si$, after the γ-ray yields from ^{31}P and ^{31}S were subtracted. The contribution to the γ-ray yield at 2234 keV from ^{30}Si was only 20% at the lowest energy, but was about 80% at the highest energy. The Coulomb excitation cross section for ^{16}O on the 3.1% ^{30}Si in the quartz target was calculated, and found to be negligible (less than 1% of the observed yield). The 2210 keV γ-ray from ^{27}Al was expected not to be important from the observed intensities of the 844keV and 1014keV γ-rays, and from the statistical model calculations.

The 1779keV γ-rays were completely from the first excited state of ^{28}Si. However, natural silicon contains 92.2% of ^{28}Si, thus the γ-rays from the first excited state of ^{28}Si could, in principle, be contributed from either the Coulomb excitation of ^{28}Si by the ^{16}O incident ions, or by the fusion reaction $^{16}O + {}^{16}O \rightarrow \alpha + {}^{28}Si$. The cross sections for the Coulomb excitations of ^{28}Si by ^{16}O ions were calculated from $E_{lab}(^{16}O) = 7$ MeV to 24 MeV, and the possible Coulomb excitation γ-ray yields were calculated by numerical integration of the cross section versus energy curve, assuming the chemical form of the quartz target to be SiO_2. The yields of the 1779keV γ-rays were used to determine the cross sections for production of ^{28}Si, after the Coulomb excitation yields were subtracted. The contribution to the 1779keV γ-rays from Coulomb excitation varied from 40% at the lowest energy (14 MeV lab.), to $\leq$6% at the highest energy (24 MeV lab.).

II.2.B Ge(Li) Photopeak Efficiencies

The Ge(Li) detector photopeak detection efficiencies for γ-rays with energies between 276keV and 1332keV were determined by placing calibrated sources ^{133}Ba, ^{22}Na and ^{60}Co at the target position for each of the targets used. The details of the γ-ray efficiency calibrations have been described in section (III.3.B) of part I. For the case of the quartz target, since the reaction cross section varies rapidly with energy, and since the range of ^{16}O ions in quartz is very short, the efficiencies were measured with the assumption that all the γ-rays come from the "upstream" face of the quartz target disc. The efficiency measured for use with the evaporated target, or the anodized tantalum target, is higher than that for the quartz target by 35% because of the difference in target-to-detector distance.

A ^{56}Co source with γ-rays of several energies between 847keV and 3.3 MeV was used to determine the relative efficiency of the Ge(Li) detector for each type of target used. The relative intensity for each γ-ray from the source is well-known (Ke74, Mc75), and the relative intensities are tabulated in table 2. Since the energies of the γ-rays used to determine the fusion cross sections vary from 709keV to 2236keV, there was no need to extend the efficiency calibrations to higher energies, for the ^{16}O + ^{16}O measurements.

II.3 Targets

Three different types of target were used : (1) Thin silicon monoxide targets evaporated onto 99.99% pure copper discs; (2) A 1/8-inch thick fused silica (quartz) disc; (3) An anodized tantalum target.

II.3.A Evaporated Silicon Monoxide Targets

The silicon monoxide targets for the fusion measurements were prepared by electron beam evaporation onto 99.99% pure copper discs of 0.25 cm thickness. In order to determine the silicon, oxygen and carbon composition of this target, silicon monoxide was also evaporated onto a glass slide coated with approximately 20 $\mu g/cm^2$ of carbon. Two different types of targets were made from the same glass substrate: (a) transmission carbon-backed silicon monoxide targets, and (b) carbon-backed silicon monoxide targets floated onto pure copper discs. The α-scattering measurements described below demonstrated that the carbon, silicon and oxygen thickness of different transmission targets from the same glass substrate were consistent to within ±2%. Each carbon-backed silicon monoxide target was made with a thin layer of gold flashed over it.

To determine the silicon monoxide-carbon composition of each trasmission target, α-particles of energy from 1.50 MeV to 1.70 MeV were used to bombard the target. The relative elastic scattering yields measured at $\theta_{lab.}=140^o$ from the oxygen and gold layers were consistent with Rutherford scattering. The data accumulated at E_α = 1.5 MeV and $\theta_{lab.}=140^o$ were used to determine the ^{12}C, ^{16}O and ^{28}Si contents of the target, assuming Rutherford scattering cross sections. The solid angle subtended by the counter aperture was 2.26×10^{-4} with an accuracy better than ±2%. An additional aperture 0.5 cm from the surface-barrier detector was used to stop particles scattered from the edge of the first aperture. The small subtended angle (0.48^o)

in the θ-direction requires practically no correction for the $1/\sin^4(\frac{\theta}{2})$ law. The beam current transmitted by the thin targets was collected in a magnetically-suppressed Faraday cup. The equilibrium charge state of the α-particles after passing through the target was obtained from Marion and Young (Ma 68). The transmission target contained typically 18.5 $\mu g/cm^2$ of ^{12}C, 8.56 $\mu g/cm^2$ of ^{16}O, and 12.73 $\mu g/cm^2$ of ^{28}Si.

To avoid possible uncertainties in the ^4He beam current integration arising from an error in equilibrium charge of the ^4He beam, the gold content of the transmission target was also measured by proton elastic scattering at $E_p = 1.0$ MeV. The gold content of the target was typically 2.96 $\mu g/cm^2$, and this amount agreed with that deduced from the α-scattering measurements to ±1.5%.

The copper-backed carbon-silicon monoxide layer with known silicon-oxygen-carbon composition was used to determine the thickness of the oxide layer of the target used for the fusion measurements, which was prepared by directly evaporating silicon monoxide onto the copper disc. ^{16}O beams with 22.0 MeV incident energy were used to bombard both targets, and the relative yields from the ^{30}P 709keV γ-rays were used to determine the ratio of oxygen contents. Because of the possibility of two particles being evaporated in the $^{16}O + {}^{16}O$ reactions, the γ-rays from ^{27}Al and ^{24}Mg can only be used to determine an upper limit on the amount of ^{12}C in the copper-backed target, which was 1.38 $\mu g/cm^2$. The 417keV γ-rays from the $^{16}O + {}^{12}C \rightarrow {}^{26}Al{+}p{+}n$ reaction were used to determine the relative amount of ^{12}C with a statistical error of ±30%. The target used for the fusion measurements contains 0.96 μg/cm^2 of ^{12}C and 10.20±0.41 μg/cm^2 of ^{16}O with the ^{28}Si amount 14.64 μg/cm^2, assuming the relative amount of ^{28}Si do not change from target to target. This assumption is believed to be better than ±3.5% from the investigation of target thicknesses by α-particle scattering using different targets prepared from different evaporations.

To determine the energy-loss thickness of the target used in the fusion cross section measurements, the hydrogen contamination in the evaporation layer was measured with the ^{1}H(^{19}F,αγ) reaction (Sw75). The resonance corresponding to ^{19}F beam energy of 6.42 MeV, with resonance width 45keV, was used (Ba 77). The data for these measurements were acquired with 80 nA of ^{19}F^{+2} beam. An unshielded 12.7 x 10.2 cm NaI(Tl) detector, mounted at 0°, with 0.36 cm lead placed between the target and detector to attenuate low-energy γ-rays, counted the 6 MeV γ-rays. Gamma-rays pulses with energies $\geq$ 2 MeV were integrated for a constant charge per point of 100 μC. A γ-ray excitation function for the ^{1}H(^{19}F,αγ)^{16}O reaction is shown in fig.24.

Earlier investigations of such hydrogen profiles (Appendix, and Ba 77) have also shown the existence of surface hydrogen peaks, which are usually ascribed to a few monolayers of water adsorbed on the target. The thickness of the silicon monoxide target was inferred from the difference in energy between the surface peak and the high-energy drop-off in the γ-yield. The energy where the γ-yield drops to half its plateau value was used as the indication of the surface between the evaporated SiO film and the copper backing. The energy-thickness of the 6.42 MeV ^{19}F ions in the target was 266±20 keV after removing the resonance width.

With the Si, O, C contents determined previously, the energy loss in the same target for 6.4 MeV ^{19}F ions was calculated to be 253±13 keV. The agreement between the two numbers is excellent. For the fusion measurements done with this target, the effective energies were calculated as the incident ^{16}O energies minus one-half the energy-loss of the ^{16}O ions in the Si-O-C layer assuming a homogeneous distribution through the layer.

Gamma-ray spectra were accumulated with this target at several energies between 17.0 and 24.0 MeV ^{16}O incident energy. Peaks identified as ^{23}Na (440keV), ^{26}Mg (1809keV), and others from the $^{16}O + {}^{12}C$ reaction were observed, because of a small amount of ^{12}C in the target. A study was made of the yields from the $^{12}C + {}^{16}O$ reaction using a ^{12}C incident beam, with energies from 12.0 MeV (lab.) to 18.0 MeV, on the target containing 10.2 μg/cm^2 of ^{16}O. The cross sections for the production of ^{24}Mg and ^{27}Al were found to be consistent with the earlier measurements by Christensen et al (Ch77a). The γ-ray yield excitation functions are shown in fig.25.

Cross sections for the production of ^{30}P+p+n by $^{16}O + {}^{16}O$ were determined from the yields of the 709keV γ-ray peaks and the measured target thickness. The results were compared with those from thick quartz measurements and found to be consistent. For isotropic γ-emission, the relation between the photopeak yield Y and the cross section is

$$\sigma = \frac{Y}{N \quad n_t \quad \varepsilon \, \beta} \qquad \text{(II-2)}$$

where N is the number of incident ions, n_t is the areal number density of ^{16}O target atoms, and ε is the photopeak detection efficiency described in section II.2.B. The summing and branching correction factor β is calculated as described in section III.1 of part I, from the relative population of final states calculated by the statistical model in section III.1, the tabulated branching ratio (En 74), and the calculated total detection efficiencies.

The γ-ray yields for ^{27}Al and ^{24}Mg were used to calculate upper limits for the cross section for α+p and α+α production from the ^{16}O + ^{16}O reactions. Because of the possibility of α or p transfer reactions between ^{16}O and ^{28}Si, and possible yields contributed by the ^{12}C contaminants in the target, the cross section for the production of ^{27}Al and ^{24}Mg at $E_{c.m.}$ = 12 MeV are determined as $\leq$243 mb and $\leq$124 mb, respectively. The cross section for the production of ^{28}Si from the ^{16}O + ^{16}O reaction, as well as other residual nuclei cannot be determined because of nearby γ-rays (for example, 1809keV γ-ray from ^{26}Mg), produced by the ^{16}O + ^{12}C reactions.

II.3.B Quartz Target

Because of the γ-rays produced by the ^{16}O + ^{12}C reaction arising from the carbon contamination in the evaporated target, a 1/8-inch thick quartz disc was tried as a carbon-free target. The target was heated in hydrochloric acid after cleaning with standard solvents, to remove any carbon left from the cleaning solution, and then mounted in the target chamber. It has been conjectured that during the runs, the target was slowly sputtered away by the ^{16}O beams, because of the low heat conductivity of quartz; in any case, no carbon build-up during running was found.

A γ-ray excitation function was measured for $E_{c.m.}$ from 7.0 MeV to 12.0 MeV, in steps of 250keV. An example of the spectra obtained by the Ge(Li) detector (placed at 0°) is shown in fig.23. In order to deduce the cross sections, the thick target yields were differentiated numerically and then corrected for the appropriate stopping power as given by Northcliffe and Schilling (No 70). The cross section was assumed to vary linearly with energy over a region of $\Delta E_{lab.} = 500keV$. The cross sections were thus estimated as

$$\tilde{\sigma}\left(\frac{E_1+E_2}{2}\right) = \frac{Y(2) - Y(1)}{n_t \ \varepsilon \ \beta} \qquad \text{(II-3)}$$

where Y(1) and Y(2) are the γ-ray yields per incident ^{16}O atom measured at the energies E_1 and E_2, with $E_2 > E_1$. ε is the photopeak detection efficiency. The calculated summing and branching correction β was also assumed to vary linearly with the energy, and a value of $[\beta(E_1)+\beta(E_2)]/2$ was thus adopted. n_t is the areal number density of ^{16}O target atoms in the energy interval of $\Delta E_{lab.} = E_2 - E_1$ at an energy of $(E_1+E_2)/2$, as calculated from the stopping power given by Northcliffe and Schilling (No 70)

To reduce the propagation of the errors in Y(2)-Y(1), especially when Y(1) ≃ Y(2), the calculated cross sections $\tilde{\sigma}$ were smoothed by assuming that

$$\sigma_f(E) = \exp(A_0 + A_1E + A_2E^2) \qquad \text{(II-4)}$$

where A_0, A_1, A_2 are parameters determined by a polynomial fit of $\ln\tilde{\sigma}(E)$. The <u>predicted</u> yield per incident ^{16}O atom, Y_p, at laboratory energy E is calculated as

$$Y_p = \int \sigma_f(E)\ \varepsilon\ \beta(E)\ ndx \qquad \text{(II-5)}$$

The areal number density ndx for ^{16}O in target (in unit of atoms/cm^2), in the interval dE is given by

$$dE = ndx\ \left(\frac{dE}{dx}\right)_O \frac{15.994 \times 10^3}{6.02 \times 10^{23}} + \frac{1}{2}\ ndx\ \left(\frac{dE}{dx}\right)_{Si} \frac{28.086 \times 10^3}{6.02 \times 10^{23}}$$

$$[\text{MeV}] = \left[\frac{\text{atom}}{\text{cm}^2}\right] \left[\frac{\text{MeV}}{\text{mg/cm}^2}\right] \left[\frac{\text{mg}}{\text{atom}}\right] \qquad \text{(II-6)}$$

The assumption has been made (for simplicity) that the silicon isotopic abundance distribution in the quartz is identical to that tabulated for average natural silicon, that the ^{16}O isotopic abundance is 100% (instead of 99.76%), and that the chemical form SiO_2 remains valid for the quartz even after being heated by the ^{16}O beams.

Numerical integrations were performed by Simpson's rule, with an energy interval of 0.01 MeV, and β was assumed to vary linearly with E, over each energy interval of 1.0 MeV laboratory energy. The cross section at laboratory energy $E_{lab.}$ is then

$$\sigma(E_{lab.}) = \sigma_f(E_{lab.}) \frac{Y(E_{lab.})}{Y_p(E_{lab.})} \qquad \text{(II-7)}$$

where Y and Y_p are the measured and calculated yields, respectively, and σ_f is the cross section calculated from the polynomial fitting in eq.(II-4).

Cross sections for the formation of the residual nuclei ^{28}Si, ^{31}P, ^{31}S and ^{30}P were calculated from the data accumulated with the quartz target. The data from measurements made with a 1/8" thick quartz agreed with those from a 1/16" thick quartz, after corrections were made for detector efficiency and β's, to better than 2%. The cross sections for the ^{30}P residual nucleus agreed well with the results obtained from the evaporated silicon monoxide target over the energy region from 18 to 24 MeV in the laboratory frame. The results are shown in chapter IV.

The cross sections for the formation of ^{24}Mg and ^{27}Al were calculated from the data obtained with the quartz target, and are compared with the data obtained from the anodized tantalum target in the section IV.2.

II.3.C Anodized Tantalum Target

Because of possible proton or alpha-particle transfer reactions between the incident ^{16}O and the ^{28}Si nuclei contained in the silicon monoxide or quartz targets (see IV.2), an anodized tantalum target was used to determine the cross sections for production of ^{24}Mg and ^{27}Al in the reaction, ^{16}O + ^{16}O. The anodized tantalum target was mounted in the target chamber, and spectra were accumulated over the ^{16}O energy region from 18.0 MeV to 24.0 MeV (lab. energy). This target contained less than 0.082 $\mu g/cm^2$ (±20%) of ^{12}C at the beginning of the experiment. This ^{12}C thickness was determined by assuming that all of the 1369keV γ-ray yield (from ^{24}Mg) was contributed by the reaction $^{16}O + {}^{12}C$. After 8 hours of ^{16}O bombardment, the carbon deposited on the target was approximately 0.26 $\mu g/cm^2$. The ^{12}C contamination determined from the 1014keV γ-rays of ^{27}Al agreed with that determined from the 1369keV ^{24}Mg γ-rays within statistical uncertainties. In spite of the ^{12}C contamination of the target, the cross sections for production of ^{24}Mg and ^{27}Al by the $^{16}O + {}^{16}O$ reactions could be determined since the excitation function of the $^{16}O + {}^{16}O$ reactions were found to be very different from those of the $^{16}O + {}^{12}C$ reactions described in section II.2.A and shown in fig. 25 and 26.

The γ-ray yields from the 1014keV state of ^{27}Al and the 1369keV state of ^{24}Mg were carefully corrected for ^{12}C contamination, by assuming that the yield of 1369keV γ-rays at $E_{lab.}(^{16}O) = 18$ MeV was completely due to the ^{12}C contamination. The relative contribution from ^{12}C at the highest energies was then calculated from the $^{12}C + {}^{16}O$ measurements described in section II.2.A. The correction for yield from the ^{12}C contaminant was 8% at $E(^{16}O) = 20$ MeV and less than 1% at $E(^{16}O) = 24$ MeV for the ^{27}Al γ-ray. For the 1369keV ^{24}Mg γ-ray the correction was 21% at $E(^{16}O) = 20$ MeV, and 3% at $E(^{16}O) = 24$ MeV.

The cross sections for evaporating α+p and α+α in the $^{16}O + {}^{16}O$ reactions were determined by eq.(II-2), with the target thickness determined by normalizing the yields of 709keV γ-rays from ^{30}P over the laboratory energy region from 18.0 MeV to 24.0 MeV. The cross section for $^{16}O + {}^{16}O \rightarrow \alpha+p+{}^{27}Al$ is 130 mb, while the cross section for $^{16}O + {}^{16}O \rightarrow \alpha+\alpha+{}^{24}Mg$ is 23 mb, at 24.0 MeV incident energy. The energy-loss thickness of this anodized tantalum target was estimated to be 500keV with 10% precision, when the chemical form Ta_2O_5 was assumed. The statistical uncertainties of the γ-ray peaks are approximately 7% for ^{27}Al and 5% for ^{24}Mg over the energy region studied.

III. THE STATISTICAL MODEL CALCULATIONS

The fundamental assumption of the compound nucleus model is that the mode of decay of a compound state of given spin and parity is independent of how the state was formed. The independence hypothesis, together with the reciprocity theorem, are sufficient conditions to derive the Hauser-Feshbach expression (Ha 52) for the energy averaged reaction cross section from an initial channel α to a final channel β (St 74),

$$\langle\sigma\rangle_{\alpha\beta} = \frac{\pi \lambda\!\!\!^{-2}}{(2I_1+1)\ (2I_2+1)} \sum_{J^\pi} \frac{(2J+1)[\sum_{\ell s} T_\ell(\alpha)]^{J\pi}\ [\sum_{\ell' s'} T_{\ell'}(\beta)]^{J\pi}}{[\sum_{\gamma\ell'' s''} T_{\ell'' s''}(\gamma)]^{J\pi}} \qquad \text{(III-1)}$$

J is the total angular momentum , given by $\vec{J} = \vec{\ell} + \vec{s} = \vec{\ell}' + \vec{s}'$, $\vec{s} = \vec{I}_1 + \vec{I}_2$, etc., I_1, I_2 are the spins of the projectile and target, respectively. T_ℓ is the transmission coefficient which is the probability for a compound nucleus formation when the projectile and the target interact with the orbital angular momentum ℓ.

T_ℓ's are usually computed by numerical integration of the radial Schrödinger equation, outwards from the origin, to a matching radius well outside the range of the nuclear interaction. The radial Schrödinger equation is

$$\frac{\hbar^2}{2\mu} \frac{d^2}{dr^2} f_\ell(r) + \{E - V^\ell_{eff}(r)\}\ f_\ell(r) = 0 \qquad \text{(III-2)}$$

The internal solution of this equation is matched to a pure Coulomb wave function at a large radius R. The effective potential, with the nuclear part usually chosen as the so-called Woods-Saxon form, is

$$V^{\ell}_{eff}(r) = V_{nuclear} + V_{Coulomb} + V_{centrifugal}$$

$$= -(V + iW) + V_c + \frac{\ell(\ell+1)\hbar^2}{2 \mu r^2} \quad . \qquad \text{(III-3)}$$

A pure Coulomb wave function is given by the expression,

$$\Psi_{\ell}(r) = F_{\ell}(r) + iG_{\ell}(r) + S_{\ell} [F_{\ell}(r) - iG_{\ell}(r)] \ , \qquad \text{(III-4)}$$

where the transmission coefficient T_{ℓ} is given in terms of the scattering matrix S_{ℓ} by

$$T_{\ell} = 1 - |S_{\ell}|^2 \qquad \text{(III-5)}$$

If the transmission coefficient T_{ℓ} is very small ($\lesssim 10^{-4}$), the usual matching procedure may no longer be sufficiently accurate because of rounding-off errors in the computation. The transmission coefficient can be related to the imaginary potential W,

$$T_{\ell} \propto \int W \, |\Psi_{\ell}(r)|^2 \, d^3r \qquad \text{(III-6)}$$

where the volume integral is performed over the region $r < R$.

For the $^{16}O + ^{16}O$ reactions, the transmission coefficients were calculated with the optical model, using the potential of Bechetti and Greenlees (Be 69) for the proton and neutron channels, and of McFadden and Satchler (Mc 66) for the α-particle channels. For the exit channels, the forms of the potential are summarized in table 4, and the parameters are given in table 11. To evaluate the cross sections by eq.(III-1), transmission coefficients were calculated for each channel (α, p, n, etc.) at several energies E_i, for different angular momentum ℓ. The value of $T_\ell(E)$ was then interpolated as

$$T_\ell(E) = \exp \{ (E-E_i) \times \frac{\ln T_\ell(E_{i+1}) - \ln T_\ell(E_i)}{E_{i+1} - E_i} \} \qquad \text{(III-7)}$$

where $E_i < E < E_{i+1}$. Errors can arise from this interpolation if the steps at which $T_\ell(E)$ is calculated are too large. It is desired to calculate $T_\ell(E_i)$ for different energies in such a way that no significant error is caused by the interpolation, and at the same time to keep the computation within the capacity of the computer program "HAUSER*4" (Ma 76a). Figure 27 shows an example of calculated transmission coefficients T_ℓ vs energy. The errors introduced by the logarithmic interpolation were estimated as $\leq$30% at all energies. For the entrance channel, $^{16}O + ^{16}O \rightarrow ^{32}S^*$, transmission coefficients were calculated at those energies for which the relative cross sections for residual nuclei were computed.

In the evaluation of eq.(III-1), the denominator is usually summed over the discrete states, and integrated over the continuum region, of all residual nuclei. The level densities of the various residual nuclei are determined as described in the following section. Level density parameters for the various residual nuclei produced in the $^{16}O + ^{16}O$ reactions are given in table 12. A small energy interval of 0.2 MeV was used for the numerical integration over the continuum states. Transmission coefficients and level densities do not change more than about 5% over the interval.

III.1 The Level Density Parameters

The level density formulation of Gilbert and Cameron (Gi 65) has been used. The level density $\rho(E)$ at low excitation energies can be written as

$$\rho(E) = \frac{1}{T} \exp[(E-E_0) / T] \qquad \text{(III-8)}$$

for $E < U'$, where U' is defined below. The parameter E_0 and T can be found relatively easily by plotting the log. of the cumulative number of levels up to energy E vs E. The integral of eq.(III-8) is

$$N(E) = \exp [(E-E_0) / T] \qquad \text{(III-9)}$$

An example of determining the parameters E_0 and T to fit the observed number of levels for ^{31}P nucleus is given in fig. 28.

At high excitation energies, the level density is given by

$$\rho(U) = \frac{\sqrt{\pi}}{12} \frac{\exp 2\sqrt{aU}}{a^{1/4}\, U^{5/4}} \frac{1}{\sqrt{2\pi}\ \sigma} , \qquad \text{(III-10)}$$

where a is an adjustable parameter, $U=E-\Delta$ with Δ a correction for pairing and shell effects (Di 73), and

$$\sigma^2 = \frac{I}{\hbar^2} \left(\frac{U}{a} \right)^{1/2} . \qquad \text{(III-11)}$$

in eq. (III-11), I is the moment of inertia and taken to be the rigid rotation value $2/5\ mR^2$. A value of $R = 1.04\ A^{1/3}$ was chosen, and the level density expression is then reduced to

$$\rho(U) = \frac{0.579}{A^{5/6}} \frac{\exp 2\sqrt{aU}}{U^{3/2}} \qquad \text{(III-12)}$$

It is now required that the level density be continuous at a particular energy U' = 2.5 + 150/A MeV, a suitable matching energy chosen by Gilbert and Cameron (Gi 65). The matching condition then leads to the following values of a and Δ :

$$a = U' \left(\frac{1}{T} + \frac{3}{2U'} \right)^2 \tag{III-13}$$

$$\Delta = E_0 - U' + T \left[2\sqrt{aU'} + \ln\left(\frac{0.579\ T}{A^{5/6}\ U'^{3/2}} \right) \right] \tag{III-14}$$

For the spin dependent energy level distribution, the relation

$$\begin{aligned} \rho(U,J) &= \rho(U)\ \rho(J) \\ &= \rho(U)\ \frac{2J+1}{2\ \sigma^2}\ \exp[-J(J+1)/2\sigma^2] \end{aligned} \tag{III-15}$$

was adopted.

III.2 Statistical Model Calculation for $^{16}O + ^{16}O$

For the $^{16}O + ^{16}O$ reactions, ^{28}Si, ^{31}P and ^{31}S can be formed at such high excitation energy that another particle can be evaporated. Statistical model calculations for heavy ion reactions with open two-particle evaporation channels have been performed previously (Ol 74, Ch 77a). The computer code "HAUSER*4" provides the capability for this kind of two-stage calculation. The successive evaporation of light particles was calculated without additional approximations. First, the population distribution of the intermediate excited nucleus (^{28}Si, ^{31}P or ^{31}S) was calculated as a function of excitation energy, spin, and parity, and these quantities were then considered explicitly in the statistical model calculation of the decay of the intermediate system. In other words, the evaporation of two particles can take place as

$$
\begin{aligned}
{}^{16}O + {}^{16}O \rightarrow\ & {}^{28}Si + \alpha \\
\text{or } & {}^{31}P + p \\
\text{or } & {}^{31}S + n
\end{aligned}
$$

and then,

$$
\begin{aligned}
{}^{28}Si \rightarrow\ & {}^{24}Mg + \alpha \\
\text{or } & {}^{27}Al + p \\
\text{or } & {}^{27}Si + n \\
\text{or } & {}^{28}Si + \gamma
\end{aligned}
\qquad \text{(III-16)}
$$

etc.. The probability for the production of the ^{24}Mg ground state, as a function of ^{28}Si excitation energy, spin, and parity was calculated by inverting the decay, and treating α + ^{24}Mg as the entrance channel for forming ^{28}Si, followed by the emission of protons, neutrons and gamma rays. Similar computations were performed for p + ^{30}Si and p + ^{30}P as entrance channels for ^{31}P and ^{31}S, respectively. No width fluctuation corrections were included in the second stage calculation, because this phenomenon enhances elastic scattering cross sections from the entrance channel and elastic scattering is not relevant for the problem at hand. The cross section for production of 2α+^{24}Mg(g.s.) from ^{16}O + ^{16}O reaction was then calculated as

$$\sigma(2\alpha + {}^{24}Mg(g.s.)) = \int \sum_{J^\pi} \sigma(\alpha + {}^{28}Si, E_x, J_x^{\pi_x})\ P(E_x, J_x^{\pi_x}; \alpha + {}^{24}Mg(g.s.))\, dE_x \qquad \text{(III-17)}$$

Here, $\sigma(\alpha+{}^{28}\mathrm{Si},E_x,J_x^{\pi_x})$ is the cross section for production of the reaction ${}^{16}\mathrm{O} + {}^{16}\mathrm{O} \rightarrow \alpha + {}^{28}\mathrm{Si}$, calculated from eq. (III-1) for ${}^{28}\mathrm{Si}$ at excited energy E_x, with spin and parity $J_x^{\pi_x}$. The integral over dE_x is performed over the energy region of ${}^{28}\mathrm{Si}$ allowed by conservation of energy. Since the probability of producing $\alpha + {}^{24}\mathrm{Mg}$(g.s.), as a function of ${}^{28}\mathrm{Si}$ excitation energy, spin, and parity was calculated at several excitation energies of ${}^{28}\mathrm{Si}$, and then interpolated linearly, it is also necessary to calculate the probabilities with small excitation energy intervals, but also stay within the capacity of the computer program "HAUSER*4". For each E_x and $J_x^{\pi_x}$ of ${}^{28}\mathrm{Si}$, the total probabilities for emitting alpha-particles, protons, neutrons, and γ-rays, to the various discrete and continuum states of all the exit channels sum to unity. An example of the probabilities as a function of intermediate nucleus excitation energy, spin, and parity is shown in fig. 29. The probability function was calculated in 0.5MeV steps.

For some residual nuclei, such as ${}^{27}\mathrm{Al}$, two light particles can be evaporated sequentially in either order. The cross sections for α+p and p+α emissions were calculated separately, and the results were summed. For ${}^{30}\mathrm{P}$, the cross sections were summed for the population by p+n, n+p, and deuteron emission.

III.3 Bound State Fractions

The bound state fraction is defined as the probability that, when a residual nucleus is formed, it is formed in a state which can not decay by another particle emission. The bound state fraction for

^{28}Si is thus determined by

$$F(^{28}\mathrm{Si}) = \frac{\sigma_\gamma}{\sigma_\alpha + \sigma_p + \sigma_n + \sigma_\gamma} \quad , \qquad \text{(III-18)}$$

where σ_α is the cross section calculated from eq. (III-17) and summed over all final discrete and continuum states of ^{24}Mg. σ_p, σ_n and σ_γ are calculated similarly.

Such two stage calculations were performed for ^{28}Si, ^{31}P and ^{31}S over the energy region of the present experiment, and the results are shown in fig. 30. The bound state fractions were used to give a rough estimate of the total fusion cross section in the manner described by Dayras et al for the reaction of ^{12}C + ^{13}C (Da 76b). The results are given in section IV.4.

IV. FUSION CROSS SECTIONS

IV.1 Cross Sections for ^{28}Si, ^{31}P, ^{31}S, ^{30}Si and ^{30}P

The cross sections for the production of ^{28}Si, ^{31}P, ^{31}S, ^{30}Si and ^{30}P were determined from the data obtained with the (thick) quartz target, by numerical differentiation, as described in section II.2.B. The summing and branching corrections β, needed in eq. (II-3) and (II-4), were calculated on the basis of the relative cross sections calculated from the statistical model, as described in section III.2. The summing and branching corrections, which represent the probability that the production of a particular residual nucleus results in the detection of a specific γ-ray in the photopeak were calculated as a function of center of mass energy, and are shown in fig. 31. More details of the calculation of the summing and branching correction have been given in section III.1 of part I.

The summing and branching correction factors are not particularly sensitive to the results of the statistical model calculation for one-particle evaporation processes. For two-particle evaporations, this correction factor usually increases with increasing energy of the outgoing second particle, and approaches the value given by the (2J+1) populations of the final states, for large outgoing energy.

Final states with excitation energies up to 8.90 MeV in ^{28}Si, 5.99 MeV in ^{31}P and 4.08 MeV in ^{31}S were considered. These limitations are imposed by the availability of information on the spins, parities, and branching ratios of the excited states (En 74). The thresholds for emitting a strongly interacting particle are 9.98 MeV for ^{28}Si, 7.30 MeV for ^{31}P and 6.08 MeV for ^{31}S. These thresholds are all higher than the highest energy considered in the calculation of β's. Thus none of the states under consideration can evaporate a second light particle (in contrast with the case of ^{20}Ne in part I), which would cause errors in the value of β's. The 1779keV, 1266keV and 1248keV γ-rays were used to determine the cross sections for the ^{28}Si, ^{31}P and ^{31}S channels, respectively. Cross sections for single-particle evaporation from the reaction of ^{16}O + ^{16}O,(^{28}Si, ^{31}P and ^{31}S), are shown in fig. 32, and tabulated in table 13. The overall systematic uncertainty in these results is estimated as 13%, resulting from the quadratic combination of 5% uncertainties in beam current integration, photopeak efficiency, and the numerical polynomial fitting, and a 10% uncertainty in the β-values. An additional uncertainty of 5% results from the Coulomb excitation corrections for the 1779keV γ-rays. Similarly, an additional 5% uncertainty, for the 1266keV γ-rays of ^{31}P, arises from subtracting the 1262keV γ-rays of ^{30}Si and 1263keV γ-rays of ^{30}P (see section II.2). Higher statistical uncertainties obtain for the 1248keV γ-rays. Purely statistical errors are below 2% for the 1266keV and 1779keV γ-rays, and below 5% for the 1248keV γ-rays, except where indicated in fig.32.

The 2236keV γ-ray yields of ^{30}Si were used to determine the cross sections for the production of ^{30}Si. Final states with excitation energies up to 7.00 MeV in ^{30}Si were considered in the calculations of β. The relative cross section for producing excited states are considerably smaller than for the ground state, because of the decreasing energy available for evaporating protons. Only a very small fraction of ^{30}P(0.09%) decays into the first excited state of ^{30}Si; thus no correction was made for the delayed ^{30}P activity. The statistical uncertainties for the 2236keV γ-rays were below 1% for most of the energies studied, and increase to about 15% for the lowest energies as indicated in fig. 32. The overall uncertainties in the cross sections for ^{30}Si production are estimated as 15%, which includes a 5% uncertainty arising from subtracting the 2234keV γ-rays of ^{31}P and the 2232keV γ-rays of ^{31}S. For the lowest two energies, this additional uncertainty increases to 15% and 11%, respectively. The cross sections for the ^{30}Si channel are also shown in fig. 32, and listed in table 13.

The 709keV γ-ray yields were used to determine the cross sections for production of ^{30}P. Final state excitation energies up to 3.83 MeV in ^{30}P were considered in the calculation of β. This limit is imposed by the lack of knowledge of the spins of higher excited states. In the calculations of β, the relative cross sections for the ground state and the excited states were calculated as the summation of p+n, n+p and d- emissions. States with isospin T=1 were not included in the calculation of single deuteron emission, because isospin conservation is a reasonably strong conservation law. The cross sections obtained with the thick quartz target and the evaporated silicon monoxide target agreed well, as shown in fig. 33. The excitation function of the 709keV γ-rays obtained with the anodized tantalum target agreed with the other measurements on a relative scale, as also shown in fig. 33.

The cross sections for the production of ^{30}P are tabulated in table 13. The overall uncertainty is 13%, arising simply from the uncertainties in charge integration, Ge(Li) detection efficiency, numerical fitting, and β-values.

It is of some interest to compare our ^{30}P and ^{31}S cross sections with those of Spinka and Winkler. The procedure for determining the cross sections for production of ^{30}P and ^{31}S have been described above. However, since ^{30}P and ^{31}S are radioactive nuclei, it is possible to measure the amount of ^{30}P and ^{31}S, produced in the ^{16}O + ^{16}O reaction, by the activation method (counting the residual radioactivity). Cross sections for the production of ^{30}P and ^{31}S were measured previously by Spinka and Winkler using the activation technique at several energies (Sp 74). The results of their measurements for ^{30}P are compared with the present results in fig. 33. Good agreement was found between the two different methods of measurements over the energy region from 9 MeV to 12 MeV for the center of mass system. The results for ^{31}S do not agree so well, but the cross sections for the production of ^{31}S are small compared with those for the other residual nuclei.

IV.2 The Cross Sections for ^{24}Mg and ^{27}Al

Two different kinds of contamination counts can contribute to the γ-ray yields of the ^{24}Mg and ^{27}Al residual nuclei. First, for targets which contain ^{28}Si, such as evaporated silicon monoxide and quartz, transfer reactions can take place between ^{16}O and ^{28}Si. The Q-values for proton, neutron and α-particle transfer reactions are

$$
\begin{aligned}
{}^{16}O + {}^{28}Si \rightarrow\ & {}^{17}F + {}^{27}Al && Q = -\ 10.99\ \text{MeV} \\
& {}^{17}O + {}^{27}Si && Q = -\ 13.03\ \text{MeV} \qquad \text{(IV-1)} \\
& {}^{20}Ne + {}^{24}Mg && Q = -\ 5.26\ \text{MeV}
\end{aligned}
$$

For the lowest energy measured, i.e., $E_{lab}(^{16}O)$ = 14.0 MeV, the excess energy available for an α-transfer reaction is 3.65 MeV. The α-binding energy of ^{28}Si (9.98 MeV) leads to an optimum Q-value of 3.91 MeV for the α-transfer reaction at this energy (Sw 74). Because of the highly negative Q-values of the transfer reactions listed in (IV-1), it would be expected that all of these transfer reactions will have very small cross sections at the energies of the present experiment.

To check whether the quartz target γ-ray yields at 1369keV for ^{24}Mg and 844keV, 1014keV for ^{27}Al were due to transfer reactions, an anodized tantalum target was used to measure the yields of these three γ-ray peaks. The cross section for the production of ^{24}Mg and ^{27}Al were determined for $E_{lab}(^{16}O) \geq 20$ MeV only (see section II.3.C for details). The determination of these cross sections for lower energies was limited by the ^{12}C contamination in the target, and by the low γ-ray yields from two-particle evaporation processes. The cross sections from the anodized tantalum target showed that the cross sections for the production of ^{24}Mg and ^{27}Al could also be determined from the quartz targets with good precision for $E_{lab}(^{16}O) \geq 20$ MeV. The cross sections from the anodized tantalum and quartz targets are both shown in fig. 34.

The second problem encountered for the γ-rays from the ^{24}Mg and

^{27}Al residues was caused by the carbon contamination in the target. For the same ^{16}O energy, the cross sections for $^{16}O + ^{16}O \rightarrow 2\alpha + ^{24}Mg$ and $^{16}O + ^{16}O \rightarrow \alpha + p + ^{27}Al$ are predicted from the statistical model to be much smaller than those of $^{16}O + ^{12}C \rightarrow \alpha + ^{24}Mg$ and $^{16}O + ^{12}C \rightarrow p + ^{27}Al$ at low incident energies. In addition, the relative cross sections for excited states are much lower for the production of ^{24}Mg and ^{27}Al from $^{16}O + ^{16}O$, and lead to smaller summing and branching factors. The ^{24}Mg and ^{27}Al γ-ray yields from $^{16}O + ^{16}O$ may therefore be overwhelmed by the yields from $^{16}O + ^{12}C$ at low bombarding energy. From the cross sections for α and p production from the $^{16}O + ^{12}C$ reactions measured previously (Ch 77a), it can be calculated that the ^{12}C thickness needed to produce a ^{24}Mg or ^{27}Al γ-ray yield equal to that from $^{16}O + ^{16}O$, for $E(^{16}O) \lesssim 17$ MeV, is less than one atomic layer on the quartz disc.

Although it is believed that the quartz disc was continuously sputter-cleaned by the incident beam during the run, no cross section for ^{24}Mg and ^{27}Al was determined for $E(^{16}O) \leq 18$ MeV, because of the large statistical uncertainties ($\geq 30\%$). Difficulties arose especially in the polynomial fitting of the numerically differentiated yields, described in section II.3.B. In order to estimate the cross sections for ^{24}Mg and ^{27}Al, at energies below those for which measurements were made, the statistical model was used to extrapolate downwards in bombarding energy from the energy region where reliable measurements could be made, as shown in fig. 34.

The 1014keV and 1369keV γ-rays were used to determine the production cross sections for ^{27}Al and ^{24}Mg at high bombarding energies. Final states up to energies of 5.25 MeV in ^{27}Al and 9.30 MeV in ^{24}Mg were considered in the calculation of the summing and branching correction factors. The relative cross sections of the various final states were calculated from the statistical model as described in section III.1, in order to evaluate the β's.

IV.3 Total Fusion Cross Sections

The total fusion cross sections were obtained by summing the cross sections for single-particle evaporations (^{28}Si, ^{31}P and ^{31}S) and two-particle evaporations (^{30}Si, ^{30}P, ^{27}Al and ^{24}Mg). The results are shown in fig. 35, and tabulated in table 13. The cross sections measured from proton and α-particle yields by Spinka and Winkler (Sp 74) are also shown in fig. 35. Inspection of the Q-value diagram (fig. 22) shows that there are additional open channels over the energy region studied, such as ^{27}Si+α+n and ^{12}C + ^{20}Ne, for which the cross sections have been ignored. The cross sections for the production of ^{27}Si are very small because of the small kinetic energy available for the α-particle and neutron. Peaks corresponding to the first or second excited states of ^{27}Si were not found in any of the runs. A statistical model calculation has also shown that the cross section for the production of ^{27}Si is less than 0.1% of the total cross section, even at the highest bombarding energy.

The α-transfer reaction ^{16}O + ^{16}O $\rightarrow$ ^{12}C + ^{20}Ne is expected to have a very low cross section. Spinka and Winkler have measured the cross section of $^{16}O + ^{16}O \rightarrow ^{12}C(g.s.) + ^{20}Ne(g.s.)$ by detecting ^{12}C and ^{20}Ne nuclei in coincidence, at energies well above the barrier (Sp 74). The cross section for the production of $^{12}C + ^{20}Ne$, both in the ground state, was determined to be (8±3)mb at E_{cm}= 11.95 MeV. The cross section for the α-transfer reaction to the ground states and the excited states was estimated to give a total transfer cross section for $^{16}O + ^{16}O \rightarrow ^{12}C + ^{20}Ne$ of 10mb, at this energy. This is only 2% of the total cross section at this energy.

Transfer reactions may have different energy dependence from fusion cross sections, and may become relatively more important as the bombarding energy decreases. Earlier investigations have demonstrated that an upper limit for the yield of the α-transfer reaction $^{12}C + ^{16}O \rightarrow ^{8}Be + ^{20}Ne$ is 10% of the total reaction cross section for $^{12}C + ^{16}O$, for energies at and below the Coulomb barrier (Ču 76, Sw 74). A similar conclusion was drawn earlier from purely theoretical arguments for the reaction $^{12}C + ^{12}C$ (Ko 70). The reason why these transfer cross sections are so small at low energies is because of their non-optimal Q-values; in fact their Q-values are negative. Because of the negative Q-value of the $^{16}O(^{16}O,^{12}C)^{20}Ne$ reaction (-2.4 MeV), it is certain that the α-transfer will be a negligible fraction of the total reaction cross section at all energies below 12 MeV, and that the transfer reaction cross sections can be neglected without serious error.

Dayras et al (Da 76b) have calculated the total cross sections for $^{12}C + ^{13}C$ by measuring the cross sections for single α-, p- and n-emissions, and then converting these to total cross sections with the assistance of the bound state fractions described in section III.3. Figure 36 shows the total cross sections for $^{16}O + ^{16}O$, as calculated from the cross sections for ^{28}Si and ^{31}P by the relation

$$\sigma_{total} = \frac{\sigma(^{28}Si)}{F(^{28}Si)} \quad \frac{\sigma_{\alpha}}{\sigma_{t}} \qquad \text{(IV-2)}$$

and the corresponding relation for ^{31}P. In eq.(IV-2), F is the bound state fraction factor, which converts the measured cross sections of ^{28}Si into total cross sections for emitting α-particles. σ_{α} and σ_{t} are the calculated α-channel and total cross sections as obtained from the statistical model. For the $^{16}O + ^{16}O$ reactions, the total cross sections obtained from the α-channel are higher than those from p-channel by almost a factor of 2; while in the case of $^{12}C + ^{13}C$ reaction (Da 76b), for the center of mass energies between 3 MeV and 12 MeV, the total cross sections determined by this technique from the α- and p-channels agreed to 30%, with the cross sections calculated from the α-channel data higher. For the $^{12}C + ^{13}C$ reactions, the total cross sections determined by direct summation of the cross sections for single-particle evaporations and two-particle evaporations also agree well with the cross sections determined from the bound state fractions.

A different behavior for the total cross sections determined for the $^{16}O + ^{16}O$ reaction from the alpha and proton channels than was the case for $^{12}C + ^{13}C$ may not be too surprising. It is known from earlier work (Vo 64) that reactions between "α-conjugate" nuclei result in cross sections for α-particle production which appear to be enhanced over those expected from a statistical model. For the present reaction, $^{16}O + ^{16}O$, the measured cross sections for the production of ^{28}Si, ^{31}P and ^{31}S are in the ratio 8.0:7.9:1.0, while a statistical model calculation predicts a ratio of 2.7:4.2:1.0 at E_{cm}=10MeV. A similar phenomenon was found for the reaction $^{16}O + ^{12}C$ in earlier work (Ch 77a). This tendency to underestimate α-particle production cross sections in statistical model calculations, especially for reactions between α-conjugate nuclei, may explain the factor of two cross section discrepancy noted in fig. 36.

Since calculations have been reported which successfully account for observed (p,n) and (α,n) yields for (s,d)-shell target nuclei using similar potentials and the code "HAUSER*4" (Ma 76b, Ma 75b), it is unlikely that the average optical model parameters for the calculation of the proton and alpha transmission coefficients can be much different from one reaction to another. Nevertheless, when both target and projectile are α-conjugate nuclei, there is the possibility of a non-statistical component in the α-particle yield. Christensen et al have tried to overcome the discrepancy between the calculated and observed ratio of α-particle to proton cross sections for the $^{16}O + ^{12}C$ reactions, by simply multiplying the calculated transmission coefficients for the $\alpha + ^{24}Mg$ channel by a factor of 2 (Ch 77a). The result of this procedure in statistical model calculations is not very successful : an increase in the α-production by 65% and a decrease in the p-production by 16%. For the present reaction, no effort has been made thus far to pursue the question of the large apparent alpha yield.

The total fusion cross sections as given by direct summation over the final residual nuclei are compared with those given by the α-, and p-channels with the assistance of eq. (IV-2) in fig. 36. The good agreement among the three methods of determining the total fusion cross sections verifies that the calculations of the α-α and α-p cross sections have been carried out correctly.

IV.4 The Fusion Cross Section S-factors

In comparing the predictions of various models with the experimental cross sections, it is convenient to remove the strong energy dependence arising from simple s-wave penetration arguments, and define the nuclear reaction S-factor as

$$S(E) = \sigma(E)\, E \exp(2\pi\eta) \, , \qquad \text{(IV-3)}$$

where the Coulomb parameter is defined by

$$\eta = \frac{Z_1 Z_2 e^2}{\hbar v} = \frac{179.13}{\sqrt{E}} \qquad \text{(IV-4)}$$

with $Z_1 = Z_2 = 8$. v is the relative velocity between the two heavy ions (when far apart), and E is the center-of-mass energy (in MeV).

The experimental S-factor curve for $^{16}O + {}^{16}O$ is shown in fig. 37, and tabulated in table 13. The cross sections adopted here were obtained by summing the single-particle evaporations producing ^{28}Si, ^{31}P and ^{31}S, and the two-particle evaporations which produce ^{30}Si, ^{30}P, ^{24}Mg and ^{27}Al. The uncertainties of the S-factors are about 15%, arising from roughly the same uncertainty in the formation cross section for each residual nucleus. The reaction S-factors measured previously for $^{16}O + ^{16}O$ (Sp 74) by detecting the proton, neutron and alpha-particle yields are also shown in fig. 37. The general trends of the S-factors determined by the two methods agree well over the entire energy region, with the present data lower by roughly 15% for energies below 10 MeV. No evidence for significant oscillation of the S-factors were found in the excitation functions. The present measurements and other available results are discussed in the following chapter.

V. DISCUSSION

V.1 Comparison of the Present Data with Those of Spinka and Winkler

Figure 35 and 37 give the total cross sections and the S-factors of the present measurements, with those of Spinka and Winkler (Sp 74). The total cross sections agree within the combined uncertainties of the two measurements. At low energies, the present S-factor measurements are lower than those from the Spinka and Winkler particle measurements, while the Spinka and Winkler S-factors obtained from γ-ray yields measured with a NaI crystal are higher than the particle-yield measurements by 50% to 60% at some energies.

In the present measurements, the cross sections for the ^{24}Mg and ^{27}Al channels were measured at high energies, and then extrapolated to low energies, following the trend of the statistical model. This procedure for dealing with the low-energy reaction cross sections for the ^{24}Mg and ^{27}Al channels could possibly lead to a significant systematic error in the total cross sections. Because of the small Q-values of the ^{24}Mg and ^{27}Al channels, the cross sections for producing these two residual nuclei in their ground states are relatively high, especially in the low bombarding energy region. With the present technique of measuring γ-rays from the residual nuclei, it is not possible to precisely measure the cross sections for ^{24}Mg and ^{27}Al production at energies below 10 MeV center of mass. Counting the light particles, as done by Spinka and Winkler, leads to an uncertainty arising from the possibility of double counting of two-particle evaporations (Ch 77b). Thus the cross sections for the production of ^{24}Mg and ^{27}Al can apparently not be measured more precisely by counting evaporating particles, than by the technique of the present thesis.

In their particle yield measurements, Spinka and Winkler determined the cross section by computing lower limits and upper limits, and then adopting their average as the fusion cross section. The lower limits were obtained by assuming that all counts in the proton and alpha spectra were from two-particle evaporations except for the particles in the higher energy peaks arising from ground state and low excited state particle emission. The upper limits were obtained by assuming that all protons and alphas were from single-particle evaporation processes.
It does not seem likely that Spinka and Winkler have made serious errors in their NaI measurements at the higher energies, because the NaI measurements were normalized to the particle measurements at E_{cm}=9.85 MeV, where the two-particle evaporations do not dominate the total cross section.

In the present measurements, the cross sections were determined from the γ-ray yields from a thick quartz target. The numerical differentiation and integration process could result in some uncertainty. In the first estimate of the cross sections with eq.(II-3), the cross sections were assigned to average energies, assuming that the cross section varies linearly with energy. Since the cross sections usually have stronger energy dependences than linear, especially in the low energy region, the polynomial fitting may lead to a slower energy dependence than the "true" cross section curve. The assumption that the summing and branching correction factors β vary linearly with energy will also contribute some error.

A serious problem encountered in all of the measurements was carbon contamination in the target. The $^{16}O + ^{12}C$ reaction cross sections are much higher than those for $^{16}O + ^{16}O$ at the same ^{16}O energy. As mentioned in section IV.2, one atomic layer of ^{12}C is sufficient to overwhelm the γ-ray yield from the production of ^{24}Mg and ^{27}Al by the $^{16}O + ^{16}O$ reactions for $E_{cm} \leq 10$ MeV. In the present experiment, the contamination of ^{12}C was treated carefully. For the measurements by Spinka and Winkler (Sp 74), high purity (99.99% by volume) oxygen gas was used as the target. Nevertheless, a small amount of carbon-containing vapor could come from the pumps in their experiment, or carbon could deposit on any surfaces near the target which were struck by beam. As a result, γ-rays from the $^{16}O + ^{12}C$ reaction could be produced, and these would be detected by the NaI crystal which could not resolve individual γ-rays. The relative cross sections would then be too high for the low energy measurements. Extra protons and alpha-particles would also be produced by the carbon contamination, and give higher cross sections in the particle yield measurements. However, since the $^{16}O + ^{12}C$ reaction has lower Q-values in general than $^{16}O + ^{16}O$, the evaporated protons and α-particles would have lower kinetic energies, and a larger portion of these light particles would be lost in the foils inserted to stop the elastically scattered particles and the fusion residue nuclei. As a result, the cross sections measured from the particle yield could still be somewhat too high at low energies, but would likely be lower than the cross sections from the NaI detector.

Spinka and Winkler also measured the γ-ray yields for the $^{12}C + {}^{12}C$ reactions between E_{cm}= 3.7 MeV and 7.5 MeV with a NaI crystal. The relative cross sections determined by the γ-ray yields with $E_{\gamma} \geq 1.4$ MeV reproduced the cross section fluctuations of the $^{12}C + {}^{12}C$ reaction, both in center-of-mass energy and magnitude, when compared with the measurements made by detecting charged particles (Pa 69). The conclusion was drawn that the γ-ray yields with the NaI crystal gave a good relative measure of the total reaction cross sections. Oxygen contamination would be unlikely to give a significant yield of extra γ-rays in the study of $^{12}C + {}^{12}C$ reactions, because of the higher nuclear charge of ^{16}O. On the other hand, small amounts of ^{12}C could contribute an enormous yield of γ-rays when studying the $^{16}O + {}^{16}O$ reactions, Carbon contamination may provide the explanation of why the NaI crystal measurements of Spinka and Winkler lead to higher cross sections in the low energy region, than their particle measurements or the present measurements.

V.2 Comparison of the Present Data with Other Measurements at 12.0 MeV

During the present measurements, other cross section measurements for $^{16}O + {}^{16}O$ have been made (mostly at higher energies where the yields are larger) by counting γ-rays with a Ge(Li) detector. The cross sections determined near 12.0 MeV center of mass energy are 240mb±7% at 12.25 MeV by Kolata et al (Ko 77), and 200±15 mb at 12.25 MeV by Cheng et al (Ch 78a), to be compared with the cross section determined from the present work — 438mb±15% at 12.0 MeV, and the (400±100)mb at 11.85 MeV by Spinka and Winkler (Sp 74).

The basic assumption of Cheng et al (and Kolata et al, also) was " When γ-rays from all important channels are observed, resolved, and summed, the reaction cross sections can be obtained directly without relying on major assumptions of the statistical model" (Ch 78a). It is clear that such measurements will lead to much lower cross sections. First of all, γ-rays with energies higher than 4.0 MeV can hardly be detected by the Ge(Li) crystal because of a detection efficiency which decreases rapidly with increasing γ-energy. Besides, the production of residual nuclei at high excitation energies will result in cascades through the lower-lying states, to the ground states. One should not ignore these cascades, which have various branching ratios, and which can frequently cause the loss of γ-rays through summing in the detector.

Both of the measurements by Kolata et al, and by Cheng et al, make no corrections for the ground state cross sections. The direct production of the ground states is expected to be most important near reaction thresholds. For the $^{16}O + ^{16}O$ reactions at $E_{cm} = 12$ MeV, there are still quite large populations for the ground states, especially for the ^{24}Mg and ^{27}Al (two-particle evaporation) residual nuclei. It may be true that, as the center of mass energy increases, measurements such as those of Kolata et al, and Cheng et al will become more reliable, since a larger portion of the γ-rays will be detected, yet summing effects become worse, and eventually three-particle evaporation channels will be open, at higher energies.

Cheng et al made a comparison of their measured cross sections at E_{cm}= 30 MeV with those of Kolata et al, and Weidinger et al (We 76). At E_{cm}= 30 MeV, the cross sections are 956±40mb by Cheng et al, 851±60mb by Kolata et al, and 1000±150mb by Weidinger et al. The last number was measured by detecting the heavy fusion residues. The cross section for ^{24}Mg formation at this energy was 400±5mb by Cheng et al, compared with 251±19mb by Weidinger et al. This may suggest ^{12}C contamination in the target of Cheng et al.

To give a clearer idea of how well one can determine a cross section by detecting γ-rays with a Ge(Li) crystal, relative to the "real" cross section, values of the summing and branching correction factors are given below. For the ^{16}O + ^{12}C reactions at E_{cm}= 6.86 MeV, γ-ray peaks are only found at 1369keV for ^{24}Mg, and at 844keV and 1014keV, together with 2210keV for ^{27}Al. From the ^{12}C + ^{16}O Q-value diagram, one can see that the compound nucleus energy is well above the alpha-particle and proton thresholds. The probability of detecting a 1369keV γ-ray as predicted by the statistical model is 0.63, while the detection probabilities for the three γ-rays from the ^{27}Al residual nucleus sum to 0.64 at this particular center-of-mass energy. The deduced cross sections would thus be 35% too low if one followed the technique of Kolata et al, or Cheng et al.

If the cross sections for the ^{24}Mg and ^{27}Al channels have been overestimated in the present measurements, the total cross section still sums to 265mb at E_{cm}=12.0 MeV, without including any yield from the ^{24}Mg and ^{27}Al channels, the lower limit of the fusion cross section given by Spinka and Winkler was 328mb at E_{cm}=11.85 MeV (Sp 74). Averaging these two together, a lower limit of at least 300mb can be set for E_{cm}=12 MeV, while the cross sections measured by Kolata et al and Cheng et al are well below this limit. As a further check, the total cross section was calculated from the present data at E_{cm}=12.0 MeV by following the technique of Cheng et al, at the request of Dr. Paul Bonche (Bo 78), and a cross section of 226mb was obtained.

V.3 Comparison with the Calculated Cross Sections

Stokstad et al performed an optical model calculation for nine heavy ion reactions involving nuclei from ^{10}B, ^{11}B, ^{12}C, up to ^{16}O (St 76). A standard parameter set suggested by Michaud and Vogt was used (Mi 72, Mi 73). These parameters are V_o= 50 MeV, W_o= 10 MeV, r_o= 1.27 fm and a = 0.40 fm for the effective potential

$$V_{eff}^{\ell} = \frac{-(V_o + iW_o)}{1 + \exp\left(\frac{r-R_o}{a}\right)} + V_{Coulomb} + \frac{\ell(\ell+1)\,\hbar^2}{2\,\mu r^2}\,, \qquad (V\text{-}1)$$

with

$$R_o = r_o\,(A_1^{1/3} + A_2^{1/3})\ . \qquad (V\text{-}2)$$

The shapes of the calculated S-factor vs. energy curves reproduced the features of the measurements for most of the reactions. Especially at energies about 1 MeV above the barrier, it was found that there was good overall agreement between the measured amd calculated S-factors except for the $^{12}C + {}^{12}C$ and $^{16}O + {}^{16}O$ reactions. The suggestion was made that the absolute normalization for $^{16}O + {}^{16}O$ should be redetermined, because the measured S-factor was about 50% higher than the calculated value just above the barrier.

More recently, calculations were carried out by Christensen and Switkowski (Ch 77b) with the IWBC model (see chapter V of part I for details). The parameters R_0 and a of this model were determined by fitting the experimental elastic scattering data. The parameter set, V_0=50MeV, R_0=5.70fm and a=0.62fm, for a Woods-Saxon potential, was obtained for the $^{16}O + {}^{16}O$ reaction. Calculations of the predicted fusion cross sections were then carried out with this parameter set, and the calculated fusion S-factors over the energy region near and below the Coulomb barrier were found to be consistently lower than the measured S-factors of Spinka and Winkler (Sp 74).

Conservation of total flux requires that a proper fit to the measured elastic scattering should also reproduce the fusion cross section at the same energy (in the absence of direct reactions).
It is not clear at the present time what causes this apparent discrepancy between measurement and "theory" as represented by the optical and IWBC models. The elastic scattering cross sections for $^{16}O + {}^{16}O$ have been remeasured by Christensen and Switkowski (Ch 77b), and the fusion cross sections of the same reaction have been remeasured in the present work; both of the later measurements agree well with the older data by Spinka and Winkler. A similar discrepancy was found for the $^{12}C + {}^{12}C$ reaction, with both an optical model calculation by Stokstad et al (St 76), and an

IWBC model calculation by Christensen and Switkowski (Ch 77b), with the calculated S-factors only 20% lower than the measurements for the energy region near and above the Coulomb barrier in both calculations.

Kolata et al (Ko 77) performed an optical model calculation with the parameters given by Gobbi et al. This parameter set was determined by simultaneously fitting the elastic scattering excitation function, and the elastic scattering angular distributions for $^{16}O + ^{16}O$ in the center of mass energy region from 10 MeV to 40 MeV (Go 73). The parameters for their optical model potential are V = 17 MeV, $W = 0.4 + 0.1\ E_{cm}$ MeV, $R_0 = 6.8$fm and a= 0.49fm. The calculated cross section was approximately 430mb at E_{cm}=12.0 MeV, which agrees much better with the present fusion cross section than with those of Kolata et al at the same energy.

The systematic optical model calculations of Stokstad et al (St 76) seemed to work well for all reactions, except for the identical α-conjugate nuclear reactions $^{12}C + ^{12}C$ and $^{16}O + ^{16}O$. To the same extent, the IWBC model has worked very well in simultaneously fitting both elastic scattering and fusion cross sections, for example, $^{12}C + ^{16}O$ (Ch 77b), and $^{14}N + ^{10}B$ (part I). Because of the simplicity of the IWBC model, it would be really remarkable if a "global" parameter set with only general features could be used to predict fusion cross sections near the Coulomb barrier successfully for a wide range of nuclei and energies. Some efforts have been made previously (Sw 77b), and the conclusion was that slight modifications, such as in the energy dependence of the radius and diffuseness, etc., were necessary in order to achieve a systematic fitting for various reactions simultaneously.

The optical model parameter set by Gobbi et al (Go 73) gave a very good prediction of fusion cross sections near and above the Coulomb barrier. However, since the optical model has four to six independent parameters, it should be able to fit data better than the IWBC model. For example, High and Čujec (Hi 76) were able to fit elastic scattering and fusion cross sections simultaneously for many heavy ion reactions, with two independent sets of parameters. Aside from certain well-known ambiguities, the relatively large number of parameters available for adjustment in fitting data means that an optical model fit can certainly be found, but causes a corresponding loss of understanding what is really happening in heavy ion reactions.

V.4 Suggestions for Further $^{16}O + ^{16}O$ Measurements

More measurements are necessary for energies near and above the Coulomb barrier ($E_{cm} \geq 10$MeV) to finally clear up the normalization and systematic problems which are evident in the published literature. It appears, from the present work, that the experimental data of Spinka and Winkler (Sp 74) are correct, and that the results of Kolata et al (Ko 77) and Cheng et al (Ch 78a) are somehow wrong. However, before more sophisticated theoretical work is done, it seems advisable to measure the fusion cross sections near the top of the barrier by some independent technique. The fusion cross section of $^{16}O + ^{16}O$ has been measured at E_{cm}= 30 MeV by identifying the evaporation residues (We 76), using combined time-of-flight and E-ΔE techniques. A similar technique has been used to measure the fusion cross sections of $^{16,17,18}O$ + ^{12}C reactions at E_{cm}= 7 - 14 MeV (Ey 76). With this technique, angular distributions of the various cross sections for each residual nucleus need to be measured, and then integrated over angle in order to determine the total fusion cross sections. Thin self-supporting oxide targets such as SiO, NiO would probably be necessary. The residual nuclei from two- and three-particle evaporations have very small kinetic energy, and are thus very difficult to detect and identify. Contamination counts could probably still arise from the small amount of carbon in the target. Especially when the cross sections are to be measured down to lower energies, the cross sections of the ^{16}O + ^{12}C reactions are many times higher than the ^{16}O + ^{16}O cross sections. The elastic scattering cross section also increases rapidly as the center of mass energy decreases. Resolving the residual nuclei from an enormous yield of elastically scattered ^{16}O nuclei will become difficult.

It is not recommended to remeasure the fusion cross sections with the present techniques of detecting the light charged particles or the prompt γ-rays from the residual nuclei. For the former technique, as pointed out by Christensen and Switkowski (Ch 77b), "double-counting" may result in relatively large uncertainties in determining the cross sections. As the energy increases, channels for evaporating three light particles will open, and start to give "triple-counting" problems! The technique of detecting the prompt γ-rays becomes more difficult for high energy runs, as the spectra become more complicated, and even more dependent on the statistical model calculations, when the three-particle evaporation channels open. Bound state fractions can not be determined as accurately as one would like, as encountered in the reaction of $^{14}N + ^{10}B$ in part I. The computer program "HAUSER*4" needs to be further modified to make three-stage calculations possible.

The $^{16}O + ^{16}O$ fusion cross sections are needed at energies somewhat lower than the energies at which data are available at present. Carbon contamination will be a major problem to overcome. Measurements even with gas targets can easily be overwhelmed by a very small amount of carbon in the gas, or deposited on the window foil, or on the differential pumping apertures. Thick quartz discs seem to be good carbon-free targets, except that Coulomb excitation of ^{28}Si will give the dominant γ-ray contribution at 1779keV, and the cross sections for producing the $\alpha+^{28}Si$ channel cannot be accurately determined. At still lower energies, Coulomb excitation of ^{29}Si and ^{30}Si will begin to give dominant yields of 1273keV γ-rays and 2236keV γ-rays, and even the cross sections for ^{31}P formation determined from the 1264keV γ-rays in the present work will become impossible to measure.

It might be worthwhile to try a gas target with an upstream liquid-nitrogen cold trap to minimize the carbon deposition on the window foil. On the other hand , the anodized tantalum target was found initially to be quite carbon-free. More effort should be made to minimize the carbon deposition. This will require a cleaner beam line, and better target cooling, in addition to the present ultrahigh vacuum system. It is likely that a switch to cryogenic (4°K) pumping will be required to get large-volume "clean" vacuum systems.

APPENDIX

^{9}Be + ^{12}C, ^{9}Be + ^{16}O, ^{9}Be + ^{19}F REACTIONS AT ENERGIES BELOW THE BARRIER

Published in Nuclear Physics
A289 (1977) 236-252

2.N

Nuclear Physics **A289** (1977) 236–252; © *North-Holland Publishing Co., Amsterdam*

^{9}Be + ^{12}C, ^{9}Be + ^{16}O, ^{9}Be + ^{19}F REACTIONS AT ENERGIES BELOW THE BARRIER [†]

Z. E. SWITKOWSKI [††]
The Niels Bohr Institute, University of Copenhagen, Copenhagen Ø, Denmark
and
W. K. Kellogg Radiation Laboratory, California Institute of Technology, Pasadena, California 91125
and
SHIU-CHIN WU, J. C. OVERLEY [†††] and C. A. BARNES
W. K. Kellogg Radiation Laboratory,
California Institute of Technology, Pasadena, California 91125

Received 22 November 1976
(Revised 6 June 1977)

Abstract: The ^{16}O + ^{9}Be reactions have been studied from $E_{c.m.} = 2.0$ MeV to 5.1 MeV, an energy near the top of the Coulomb barrier. The cross section for the neutron transfer reaction ^{9}Be(^{16}O, ^{17}O* (0.87 MeV))^{8}Be has been measured over this range by detecting the prompt 0.87 MeV γ-rays. The total fusion cross section has been determined from $E_{c.m.} = 2.8$ to 5.1 MeV by observing individual γ-ray transitions in the evaporation residues with a Ge(Li) detector, and then summing the separate yields. Direct processes are found to dominate the reaction yield below $E_{c.m.} = 4$ MeV. A comparison of the energy dependence of the fusion cross section for this reaction and the ^{12}C + ^{13}C reaction, which proceeds via the formation of the same compound nucleus, ^{25}Mg, reveals differences at sub-barrier energies. Optical model and incoming-wave boundary condition calculations are presented. Data have also been obtained for the near optimum Q-value neutron-transfer reactions ^{9}Be(^{12}C, ^{13}C*)^{8}Be and ^{9}Be(^{19}F, ^{20}F)^{8}Be, and these are discussed in terms of a simple model of sub-barrier direct reactions.

E

NUCLEAR REACTIONS ^{9}Be(^{16}O, ^{8}Be), (^{16}O, n), (^{16}O, p), (^{16}O, pn), (^{16}O, α), (^{16}O, nα), E = 5–14.5 MeV; measured γ-yields; deduced n-transfer, fusion $\sigma(E)$. ^{9}Be(^{12}C, ^{13}C), E = 3.5–9.5 MeV; ^{9}Be(^{19}F, ^{20}F), E = 7–16 MeV; measured $\sigma(E)$. Optical model, incoming wave analysis. Ge(Li) detector sub-barrier energies.

1. Introduction

Within the last few years increased attention has been directed to the study of heavy-ion reactions at energies far below the Coulomb barrier. Systematic investigations of the reactions involving targets and projectiles between ^{10}B and ^{16}O have

---

[†] Supported in part by the National Science Foundation [PHY76-83685].

[††] Present address: School of Physics, University of Melbourne, Parkville 3052, Australia.

[†††] Permanent address: Physics Department, University of Oregon, Eugene, Oregon 97403.

indicated that the fusion cross sections at energies near the barrier are generally well understood. However, as the beam energy is lowered, significant differences emerge in the energy dependences of the fusion cross sections for different systems. These have been summarized in ref. ^{1}) where it was concluded that the fusion mechanism at very low energies may depend on the microscopic properties of the interacting nuclei.

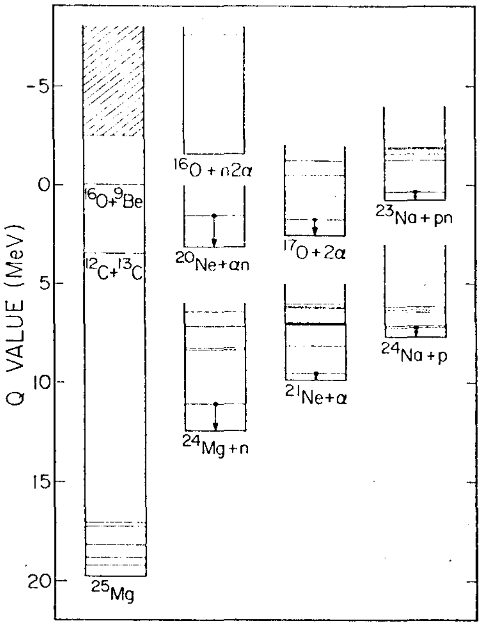

Fig. 1. The Q-values for reactions following ^{16}O+^{9}Be fusion. The γ-ray transitions in the evaporation residues which were observed in the present work are indicated. The cross-hatched region represents the range of excitation energies in ^{25}Mg studied in the present experiment.

A comparison of the ^{12}C+^{12}C and ^{12}C+^{13}C reactions at low energies perhaps illustrates one such microscopic effect. Since the charges of the interacting nuclei are the same in these cases, those entrance channel phenomena dominated by the Coulomb barrier should be similar. However, the presence of an additional neutron in ^{13}C might be expected to damp any intermediate structure such as that which might arise from α-cluster exchange. In fact, the ^{12}C+^{13}C fusion cross section exhibits no evidence for the intermediate structure displayed by the ^{12}C+^{12}C reaction but does have an energy dependence similar to the averaged energy dependence of the ^{12}C+^{12}C yield ^{2}). Such observations have proved to be important in providing guidelines for the extrapolation of heavy-ion cross sections down to astrophysically-interesting energies ^{3}).

In the present paper, we report an investigation of the ^{16}O+^{9}Be reactions. The Q-values for the most prominent decay channels are shown in fig. 1. The ^{16}O+^{9}Be system is of special interest for two reasons. The ^{25}Mg compound nucleus is populated at an excitation energy only 3.5 MeV higher than by the ^{12}C+^{13}C reaction, at the same incident c.m. energy, as shown in fig. 1. In addition, the distribution of spins of the ^{25}Mg compound states should be similar for the two reactions as their respective channel spins differ by only one unit. Therefore, those features of the ^{16}O+^{9}Be and ^{12}C+^{13}C reactions which are determined by barrier penetration considerations should be much the same for the two reactions and a comparison of the cross section trends might reveal differences which could be attributed to the different microscopic features of the interacting nuclei.

Secondly, the neutron transfer reaction ^{9}Be(^{16}O, ^{17}O)^{8}Be is expected to be important at low energies because of its positive Q-value of 2.48 MeV. Thus it is of further interest to study the behavior of the fusion process in the presence of an increasing and, at sufficiently low energies, dominating competition from direct channels. Such an investigation was reported earlier by Switkowski *et al.* [4]) in the ^{14}N+^{14}N system but, because of the very low yields, fusion data were not obtained at energies where the direct channels accounted for most of the reaction cross section.

In sect. 2 we describe briefly the experimental details for the ^{16}O+^{9}Be measurement. Additional studies were conducted for two other neutron-transfer reactions with optimum Q-values involving the ^{9}Be target, ^{9}Be(^{12}C, ^{13}C) and ^{9}Be(^{19}F, ^{20}F), and details for these reactions are also included in sect. 2. The results for the ^{16}O+^{9}Be reactions are presented in sect. 3, and a theoretical analysis of the present measurements and complementary elastic scattering data, are given in sect. 4. Sect. 5 deals further with the neutron-transfer data and the final section of the paper summarizes the present work.

2. Experimental details

2.1. TARGET

An elemental beryllium target (^{9}Be is the only stable isotope of beryllium) was prepared by electron-beam evaporation of 98 % spectroscopic grade Be onto a 0.25 mm copper backing. With the possible exception of hydrogen all significant impurities in the beryllium were high-Z elements and consequently were not serious because of their large Coulomb barrier for interaction with the ^{16}O beam. The target thickness was determined by measuring the profile of hydrogen in the Be layer [5]). Earlier investigations had shown that the hydrogen content of copper was typically small ($<$ 0.05 % by atomic concentration), and would not interfere with the detection of hydrogen in the Be layer. The ^{1}H(^{19}F, $\alpha\gamma$) resonance at $E(^{19}\mathrm{F}) = 6.4$ MeV was selected for our purposes, as the usually employed $E(^{19}\mathrm{F}) = 16.45$ MeV resonance was at a sufficiently high energy that the yield of 6–7 MeV γ-rays from the ^{19}F+^{1}H reaction was completely overwhelmed by γ-rays from the ^{19}F+^{9}Be reactions. The lower energy resonance has a yield smaller by a factor of $\approx$ 10 (ref. [6])) but virtually no γ-ray background problem from other nuclear reactions. An additional advantage of the lower energy resonance is its narrower width, 46 keV for the ^{19}F beam [6]).

A γ-ray excitation function for the $^1H(^{19}F, \alpha\gamma)^{16}O$ reaction is shown in fig. 2. The data for these measurements were acquired with 300 nA of $^{19}F^{3+}$ beam for an integrated charge of 30 μC at each point. A $12.7 \times 10.2\ cm^2$ NaI detector, mounted at 0° about 1.5 cm from the target, counted the γ-rays. A more complete discussion of the technique is given in ref. [5]).

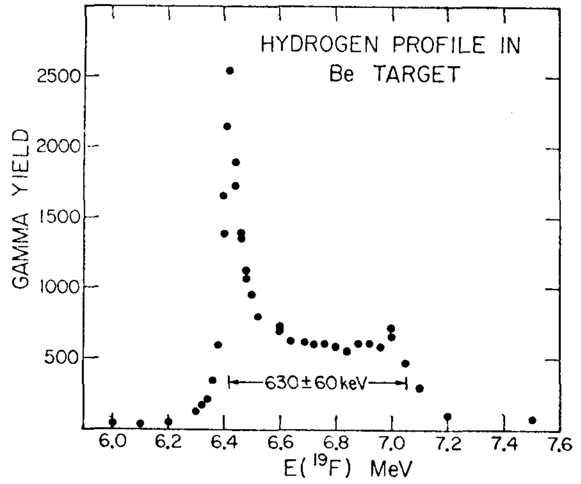

Fig. 2. Profile of the hydrogen distribution in the beryllium target. The ordinate represents the integrated number of events in a γ-pulse height window of $3.5 < E_\gamma < 8$ MeV normalized per 10 particle μC. Converting the ^{19}F beam energy loss provides a value of $52 \pm 6\ \mu g/cm^2$ for the Be target thickness.

Inspection of fig. 2 shows a concentration of hydrogen at the surface. This surface peak, with width determined by the resonance width, is usually caused by a few monolayers of water adsorbed on the target, and usually diminishes upon heating the target with the beam. A small decrease of the surface peak as a function of running time was noted but no special effort was made to reduce the hydrogen content. Comparison of the γ-yield from the hydrogen in the bulk of the ^9Be with that obtained from thick hydrogen-containing Lexan and Kapton targets indicated an average hydrogen content in the ^9Be target of 0.6 at. %. This abundance of hydrogen is not sufficient to cause difficulties in our measurements of the neutron-transfer cross sections, although (d, p) reactions arising from the deuterium in the target produce the same states as the neutron-transfer reactions.

The thickness of the ^9Be target is inferred from the difference in energy between the surface peak and the high-energy drop-off in the γ-yield. There is an uncertainty in the present thickness measurement caused by the small peak around $E(^{19}F) = 7$ MeV. This peak could arise, as has sometimes been observed in other targets, from a hydrogen containing layer trapped between the Be film and the Cu backing. If so, the position of this peak would define the inner surface of the Be layer. On the other hand, if this small peak represents simply a slightly higher hydrogen concentration near the inner Be surface, the energy where the γ-yield drops to half its plateau value would be a more appropriate choice. We have selected an energy midway between these alternatives, and assigned an uncertainty in thickness which includes both possibilities. Thus the ^{19}F beam energy loss in the target was 630 ± 60 keV, from which we deduce a Be thickness of 52 ± 6 μg/cm^2 (including a 5 % uncertainty in $\mathrm{d}E/\mathrm{d}x$) using the stopping power tables of Northcliffe and Schilling [7]).

Extreme non-uniformities in the Be deposit could invalidate this thickness measurement. However, the mirror finish of the target surface and the uniform hydrogen concentration between the peaks of fig. 2 indicate uniformity. The width of the high-energy edge of the excitation function in fig. 2 is also completely consistent with beam straggling through a uniform thin film [5]).

Tests were made to determine whether there was sufficient carbon or oxygen content in the target to invalidate our Be thickness determination. The target was bombarded with a 24 MeV oxygen beam where the cross sections for ^{16}O induced reactions on Be, C and O are comparable. At this energy the reaction cross sections are: (i) $^{16}\mathrm{O}+{}^{9}\mathrm{Be}-620$ mb (calculated as discussed later), (ii) $^{16}\mathrm{O}+{}^{12}\mathrm{C}-400$ mb (ref. [8])), and (iii) $^{16}\mathrm{O}+{}^{16}\mathrm{O}-400$ mb (ref. [9])). A detailed examination of the measured γ-spectrum for γ-ray peaks which could be ascribed to reactions on ^{12}C or ^{16}O did not reveal any significant yield. We conclude that the abundance of carbon and oxygen contamination in our target is $\lessapprox 2$ %, which causes a negligible uncertainty in target thickness.

2.2. THE $^{16}\mathrm{O}+{}^{9}\mathrm{Be}$ MEASUREMENTS

The ^{16}O beams from the ONR-CIT tandem accelerator were magnetically analyzed and bombarded the Be target. Details of the ultra-high vacuum system in which the target was mounted are given elsewhere [10]). Prompt γ-rays were counted with a 73 cm^3 Ge(Li) detector located at 0° at a distance of about 1 cm from the target. The detector was shielded with 10 cm of lead. Gamma-ray excitation functions were measured for ^{16}O beams with energies in the range from 5 to 14.5 MeV. Beam currents varied from 1 μA (3^+) at the lowest energies to 50 nA (4^+) at the higher energies. Data were acquired in the direction of increasing energy in order to minimize the effects of the accumulated ^{24}Na activity ($\tau_{\frac{1}{2}} = 15$ h) produced by the ^{9}Be(^{16}O, p)^{24}Na reaction. The presence of this activity, which would interfere with identification of prompt γ-rays from the ^{9}Be(^{16}O, n)^{24}Mg reaction of interest, was regularly monitored by observing the yield of 1.369 MeV γ-rays with the beam stopped upstream of the target. When extracting the yield of prompt 1.369 MeV γ-rays, a correction was applied for the delayed component. This correction was never more than a few percent.

2.3. NEUTRON TRANSFER MEASUREMENTS

In order to study the ^{9}Be(^{12}C, ^{13}C)^{8}Be neutron-transfer reaction, the ^{9}Be target was bombarded with ^{12}C beams, and prompt γ-rays de-exciting the first three excited states of ^{13}C were measured by a 50 cm^3 or a 73 cm^3 Ge(Li) detector. Data were acquired for the ^{12}C bombarding energy range 3.5–9.5 MeV with beam intensities that were typically 60 nA (3^+). No attempt was made to accumulate sufficient statistical precision for the yields of other γ-rays arising from ^{9}Be+^{12}C reactions and the fusion cross section was not determined.

For the ^{9}Be(^{19}F, ^{20}F)^{8}Be reaction study, we took advantage of the convenient half-life ($\tau_{\frac{1}{2}}$ = 11 sec) and decay properties (100 % β^- decay to the 1.634 MeV state in ^{20}Ne) of ^{20}F. The target was irradiated with a ^{19}F beam for approximately one mean life (15.8 sec); the beam was then interrupted and the delayed 1.634 MeV γ-yield was measured for one mean life, This cycle was repeated until sufficient statistical precision was achieved, With a 1.5 μA 3^+ beam bombarding the target, 10 cycles were adequate except at the lowest energies. An excitation function was obtained for ^{19}F beam energies in the range of 7–16 MeV.

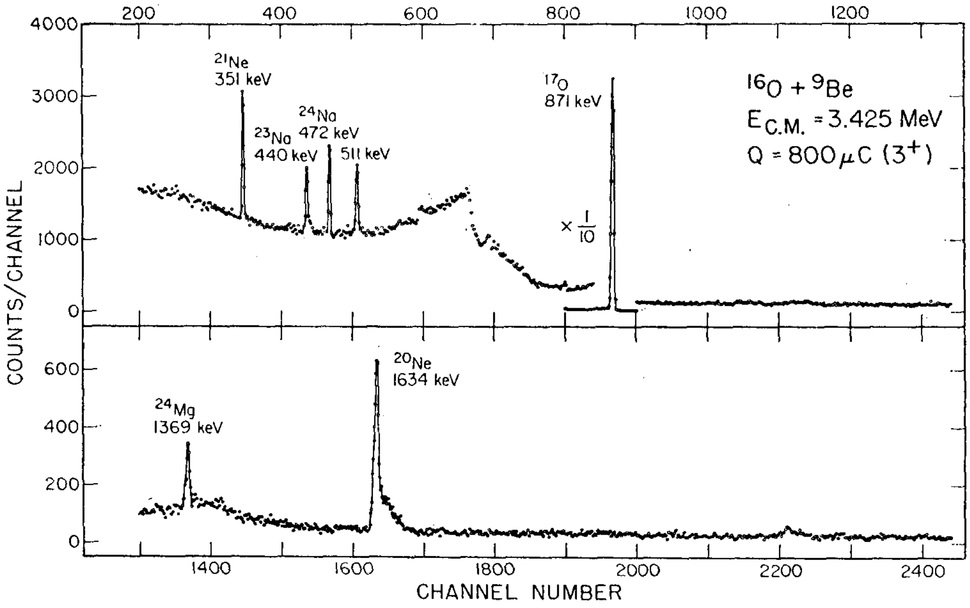

Fig. 3. Example of the γ-ray spectrum obtained with 9.8 MeV ^{16}O beam incident on a thin beryllium target. The γ-ray photopeak energy is noted along with the identity of the evaporation residue in which the transition occurs. The 871 keV γ-ray is the result of neutron pick-up from ^{9}Be to the first excited state of ^{17}O.

3. The ^{16}O+^{9}Be results and data reduction

An example of a γ-ray spectrum is shown in fig. 3. The pulse-height distribution exhibits peaks associated with particle evaporation from the compound nucleus ^{25}Mg and includes the following channels: ^{20}Ne+α+n, ^{21}Ne+α, ^{23}Na+p+n, ^{23}Na+d, ^{24}Na+p, and ^{24}Mg+n. The strong peak at 871 keV arises from neutron transfer to the

Table 1

Summing and branching factors, β

Exit channel	γ-energy (keV)	β
^{21}Ne+α	351	0.70
^{24}Na+p	472	0.50
^{24}Mg+n	1369	0.68
^{20}Ne+αn	1634	0.76
^{23}Na+pn	440	0.49

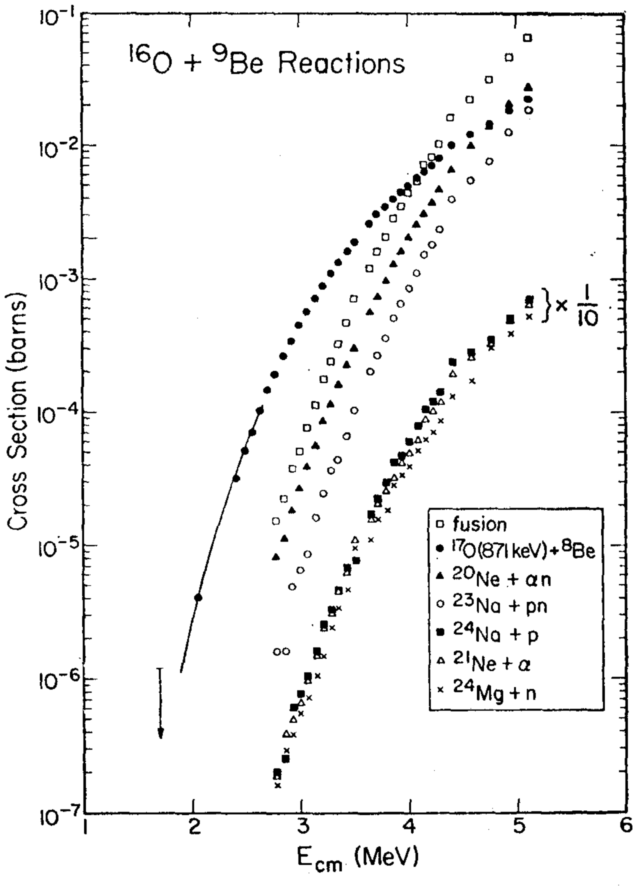

Fig. 4. The ^{16}O+^{9}Be partial reaction cross sections. The points representing the total fusion yield were obtained by summing the partial cross sections, excluding the ^{17}O*+^{8}Be channel. The uncertainty in the absolute cross sections is typically 20 % except at the lower energies where statistical errors increase the total uncertainty to 30 %.

first excited state of ^{17}O. The observation of these lines is consistent with the Q-values for the individual exit channels shown in fig. 1.

The relative distribution of yield into the various open channels is qualitatively similar to that reported for the ^{12}C+^{13}C reaction ^{2}), if a comparison is effected at the same excitation energy in the compound nucleus, ^{25}Mg. A notable exception is the ^{17}O+^{8}Be (or ^{17}O+2α) channel which, in the ^{16}O+^{9}Be case, is produced primarily by a favored neutron transfer whereas, in the ^{13}C+^{12}C case, ^{17}O is primarily produced by the sequential evaporation of α-particles from the excited compound nucleus. By assuming that one may infer the ***compound nucleus*** contribution to ^{17}O production by the ^{16}O+^{9}Be reactions from the fractional yield of ^{17}O from the ^{12}C+^{13}C reactions, we find that the 871 keV γ-yield has an insignificant (i.e. < 5 %) component from compound nucleus processes. This small correction was ignored when deducing the transfer cross sections. Furthermore, the work of Dayras *et al.* ^{2}) indicates that the ^{17}O+2α channels would be expected to account for less than 5 % of the cross section for the total fusion yield. Consequently, no attempt was made to include the ^{17}O+2α channels in the fusion yield which was subsequently inferred from the data.

TABLE 2

Total fusion cross sections and S-factors for ^{16}O+^{9}Be

$E_{c.m.}$ (MeV)	σ (b) ^{a})	S (MeV · b) ^{a})	$E_{c.m.}$ (MeV)	σ (b) ^{a})	S (MeV · b) ^{a})
2.78	1.5 (−5)	2.6 (15)	3.80	2.0 (−3)	6.6 (14)
2.86	2.2	2.1	3.87	2.8	6.5
2.93	3.7	2.1	3.94	3.5	5.8
3.00	5.2	1.8	4.01	4.3	5.3
3.07	7.6	1.6	4.09	5.6	4.8
3.15	1.1 (−4)	1.4	4.16	7.2	4.5
3.22	1.8	1.4	4.23	8.3	3.9
3.29	2.4	1.2	4.30	1.0 (−2)	3.7
3.36	3.3	1.1	4.41	1.6	3.7
3.44	4.6	1.0	4.59	2.2	2.6
3.51	6.8	9.9 (14)	4.77	3.1	1.9
3.65	1.2 (−3)	8.3	4.95	4.7	1.6
3.72	1.6	7.7	5.13	6.4	1.2

^{a}) The numbers in parentheses are powers of 10.

Gamma-ray photopeak yields were converted to cross sections with the aid of calculated summing and branching coefficients, β, and measured photopeak efficiencies. The coefficients, β, take into account the probability that a specific γ-ray is produced during the de-excitation of the states populated in the evaporation residue, that the full energy of the γ-ray is recorded by the detector and that this event is not in coincidence with other members of a cascade [2, 4, 10, 11]). The values for β, listed in table 1, were calculated by assuming a $(2J+1)$ population of final states [4]) rather than determining populations through a complete Hauser-Feshbach calculation, and by using computed total detection efficiencies and published branching ratios [6]).

Fig. 4 shows excitation functions for $^{16}O+{}^{9}Be$ reactions. The data are plotted as a function of the c.m. energy at the center of the target. Half the energy loss thickness of the target was used in determining this energy. Corrections arising from defining the effective beam energy at the center of the target were at most a few keV [refs. [4, 8])], and are smaller than the uncertainty in energy arising from the uncertainty in target thickness. The total fusion cross section was determined by adding the partial cross sections for $^{20,\,21}Ne$, $^{23,\,24}Na$ and ^{24}Mg production. The uncertainty in the absolute fusion cross section is typically $\pm 20\,\%$ obtained by quadratically combining uncertainties of 11 % in target thickness, 8 % in photopeak efficiencies, 5 % in beam current integration and 15 % in β. Experimental fusion cross sections are given in table 2.

The neutron transfer cross section measured in the present work is that for transfer to the first excited state of ^{17}O. Since this is a $\frac{1}{2}^{+}$ level, the γ-ray angular distribution is isotropic. Gamma rays were also observed which correspond to neutron transfers to the second and third excited states of ^{17}O; these yields were typical smaller by two orders of magnitude and these contributions were neglected.

4. Interpretation of the experimental data for $^{16}O+{}^{9}Be$ fusion

As an important motivation for the present work was to compare the behavior of the fusion reactions $^{16}O+{}^{9}Be$ and $^{12}C+{}^{13}C$, we show in fig. 5 their respective nuclear reaction *S*-factors [12]),

$$S(E) = \sigma(E)\,E\,\exp(2\pi\eta),$$

with

$$2\pi\eta = \begin{cases} 76.0/E^{\frac{1}{2}} & \text{for} \quad {}^{9}Be+{}^{16}O, \\ 89.0/E^{\frac{1}{2}} & \text{for} \quad {}^{12}C+{}^{13}C, \end{cases}$$

and E is the c.m. energy in MeV. Inspection of the trends of the *S*-factor immediately shows significant differences at low energies. The logarithm of the *S*-factor for $^{19}O+{}^{9}Be$ fusion has a steeper slope at low energies and shows no evidence for the flattening seen in the $^{12}C+{}^{13}C$ reaction and possibly also in the $^{12}C+{}^{16}O$ reaction [8, 10]).

The differences in the energy dependence of the *S*-factor curves are emphasized when standard optical model predictions are included in fig. 5. The curves shown are the results of optical model calculations using the average strong-absorption potential parameters of Michaud [1, 13]), given as sets 1 and 4 in table 3. We emphasize that these calculations were not intended as fits to the data, but rather to provide a basis of comparison between two different heavy-ion systems. As has been previously observed for other heavy-ion reactions [1]), the optical model prediction agrees with the experimental data for $^{16}O+{}^{9}Be$ in the vicinity of the barrier, and also with the

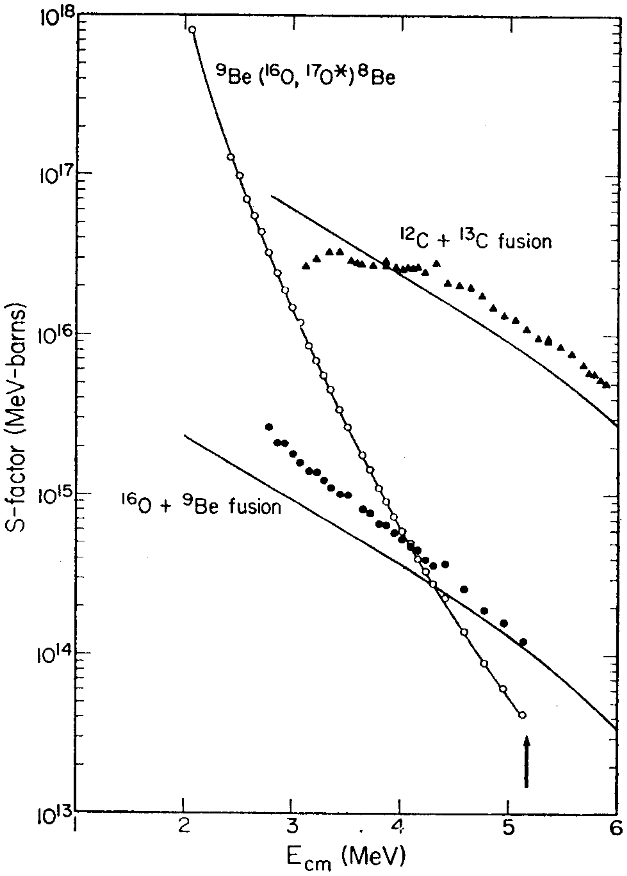

Fig. 5. Nuclear reaction S-factors for ^{16}O+^{9}Be and ^{12}C+^{13}C. Data for the ^{12}C+^{13}C reaction are taken from ref. ^{2}). The filled circles are the ^{16}O+^{9}Be fusion data while the joined open circles give the S-factor for the ^{16}O+^{9}Be → ^{17}O* (0.87 MeV)+^{8}Be reaction. The curves are optical model predictions as discussed in the text. The arrow indicates the height of the interaction barrier for ^{16}O+^{9}Be calculated from the real potential set 3 of table 3. For the case of ^{12}C+^{13}C, the barrier is 6.1 MeV [ref. ^{2})].

TABLE 3

OM and IWB parameters for fusion calculations

Channel	Set	V (MeV)	R_r (fm)	a_r (fm)	W (MeV)	R_W (fm)	a_W (fm)	Ref.
^{16}O+^{9}Be	1	50	5.80	0.4	10	5.8	0.4	^{13})
	2	60	6.21	0.5	14	6.21	0.3	^{15})
	3	50	5.78	0.52	IWB condition			present work
^{12}C+^{13}C	4	50	5.89	0.4	10	5.89	0.4	^{13})

data for $^{12}C+^{13}C$ for energies just above the barrier [2]. The $^{16}O+^{9}Be$ S-factor curves for both fusion and neutron transfer are much steeper than the optical model predictions of the total reaction cross section, while the $^{12}C+^{13}C$ fusion S-factor curve is flatter at low energies than the theoretical optical model results. Both reactions are characterized by near-optimum Q-value neutron-transfer channels, although for $^{12}C+^{13}C$, this process produces the same nuclei as the elastic scattering channel and is not accessible experimentally at low energies. The present study demonstrates that there is a significant difference in the energy dependence of the fusion of the $^{16}O+^{9}Be$ and $^{12}C+^{13}C$ systems at sub-barrier energies. This difference may arise from entrance channel effects, since the properties of the intermediate compound nucleus are similar, with the following exception. The ^{25}Mg level density is a factor of ≈ 3 higher for the $^{16}O+^{9}Be$ reaction than for the $^{12}C+^{13}C$ reaction at the same c.m. energy. However, even at the lowest energy for which the $^{12}C+^{13}C$ reaction has been measured, the calculated density of states in ^{25}Mg exceeds 1600 MeV^{-1}.

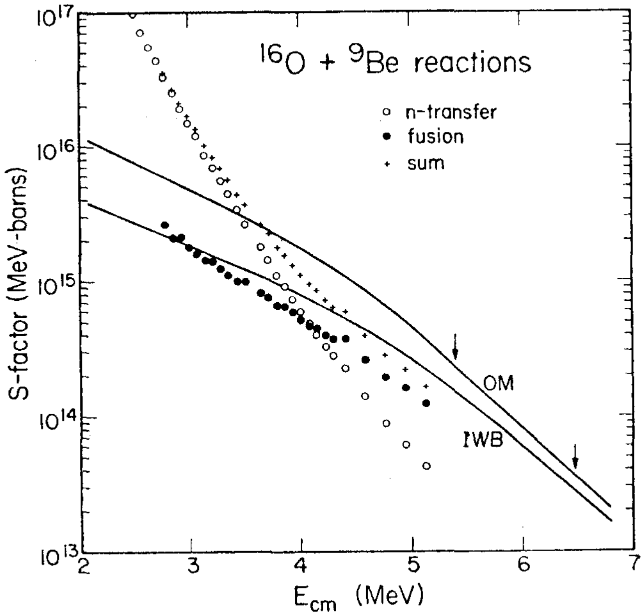

Fig. 6. Comparison of the $^{16}O+^{9}Be$ reaction data with model calculations, described in the text. The arrows indicate the two lowest energies for which elastic scattering data are available.

Optical model calculations of the kind discussed above using average parameters fit the experimental data remarkably well for five other low energy fusion reactions [refs. [11, 14]] ($^{10,11}B+^{10,11}B$, $^{12}C+^{10,11}B$), and usually overpredict the magnitude of the low-energy cross section for reactions involving still heavier nuclei. The $^{16}O+^{9}Be$ case is the first example among the cases studied where the low-energy fusion cross section exceeds predictions of the optical model with average parameters. In principle, optical model calculations should predict total *reaction* cross sections including both fusion and direct processes. In the ^{16}O+^{9}Be case, a comparison of theory with the sum of the fusion and direct components results in gross disagreement, especially at lower energies. Of course, the complex part of the optical model potential is supposed to represent absorption into many channels. When the reaction cross section is dominated by a contribution from only one channel, the appropriateness of a conventional optical model calculation may be questionable.

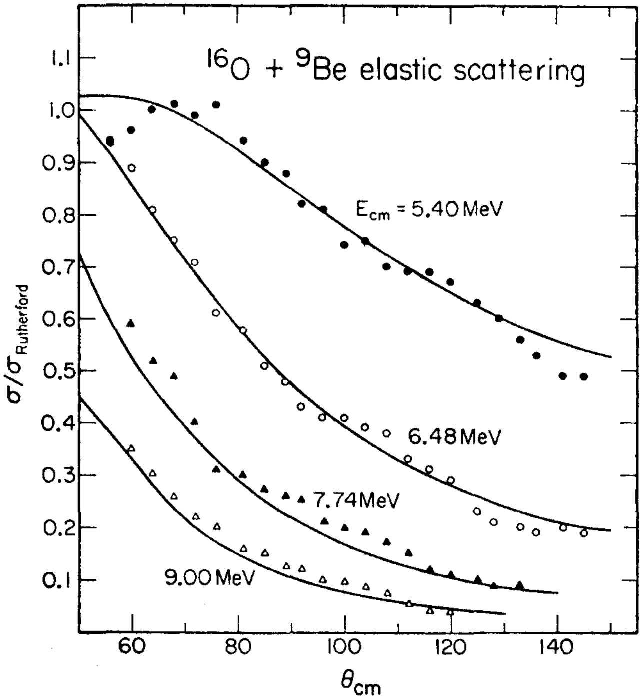

Fig. 7. Fits to ^{16}O+^{9}Be elastic scattering. The data are taken from ref. [15]). The curves are the results of IWB calculations discussed in the text.

Instead of using average potential parameters, a more direct approach is to derive the potential parameters from elastic scattering data at as low an energy as available. An analysis has been published by Barker *et al.* [15]) of their ^{16}O+^{9}Be elastic scattering data measured at 5.4, 6.48, 7.74 and 9.0 MeV c.m. The optical model parameters from their analysis are given in table 3 as set number 2, and the *S*-factor calculated from their parameters is shown by the curve labelled OM in fig. 6. In the figure, we show also the fusion and neuteron-transfer data, as well as the sum of these reactions, which should be a good representation of the total reaction cross section. The only other direct channel likely to be of any significance is the ground state neutron transfer. However, experimental measurements [15]) indicate that this cross section is down by a factor of ≈ 5 from the neutron transfer to the first excited state of ^{17}O. This is consistent with the fact that the Q-value for the ground state neutron transfer is further from the optimum value.

The agreement between the optical model calculations and the data is poor. This is rather disturbing since conservation of flux requires that the analysis of elastic scattering should lead to a reliable prediction of reaction cross sections at nearby energies. Christensen and Winther [16]) have recently drawn attention to the fact that elastic scattering is most sensitive to the strength of the nuclear potential at a distance a little outside the interaction barrier. Providing the nuclear potential at this point is kept fixed, the shape and depth of the potential may be varied over a considerable range without significantly altering the elastic scattering predictions. This property of the interaction potential was also found empirically in earlier analyses of the $^{12}C+^{13}C$ system [2]). In an attempt to identify a parameter set which describes both the elastic scattering and fusion we have reanalyzed the $^{16}O+^{9}Be$ elastic scattering data within the framework of the incoming-wave boundary condition model [17]). Details of the calculations are given elsewhere [18]). The scattering data, which were taken from fig. 5 of ref. [15]), are shown in fig. 7, together with the fits obtained. Agreement with the experimental scattering data within the errors of the data is achieved with the parameters of set 3 in table 3.

The S-factor curve which results from these calculations is shown in fig. 6 as the curve labelled IWB. Since the incoming-wave boundary condition replaces the imaginary absorptive term of the optical model with strong absorption at distances where there is a large matter overlap, the cross sections calculated from the IWB model should give a good prediction of only the fusion component of the reaction cross section at very low energies. Processes such as absorption in the long-range tail of the optical potential [13, 19]) are excluded. At higher energies (nearer the barrier), where both transfer and fusion reactions occur near the nuclear surface, the IWB calculation will more nearly represent the entire reaction cross section. Inspection of fig. 6 shows that this appears to be the case for the $^{9}Be+^{16}O$ reactions. It seems possible, therefore, to obtain a consistent description of both the elastic scattering and sub-barrier fusion data within the IWB framework.

Below $E_{c.m.} = 4$ MeV, the neutron transfer, shown as open circles in figs. 5 and 6, clearly dominates the reaction yield by a factor which increases as the energy is lowered. Such an effect was predicted earlier by Switkowski *et al.* [20]) for those transfer reactions having a near-optimum Q-value, as discussed in more detail in the next section, and an example was reported recently in ref. [4]). Whether the presence of such an overwhelming direct process significantly affects the behavior of the fusion cross section remains unclear, and the present data do not settle the question of whether there is a relation between the transfer and fusion cross sections.

5. Neutron transfer reactions

For the case of neutron transfer reactions at sub-barrier energies, the optimum

Q-value has been shown to be [20])

$$Q_{\text{opt}} = \hbar^2\kappa^2/2\mu,$$

where μ is the reduced mass in the entrance channel and κ is related to the binding energy of the transferred neutron, E_n, by the relation

$$\hbar\kappa = (2mE_n)^{\frac{1}{2}},$$

where m is the neutron reduced mass. For direct processes involving neutron pick-up from ^9Be by ^{12}C, ^{16}O and ^{19}F projectiles, Q_{opt} is $\approx$ 0.5 MeV. (Although we have usually employed the prior representation, we have verified by numerical calculations employing the post representation that detailed balance is satisfied.)

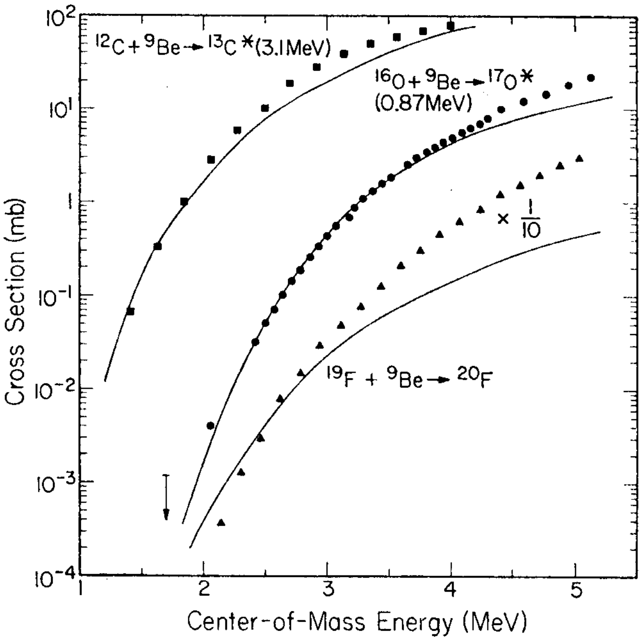

Fig. 8. Excitation functions for neutron pick-up reactions from ^9Be. The curves are transfer calculations described in the text.

The ground state Q-values for the neutron-transfer reactions $^9Be(^{12}C, ^{13}C)$, $^9Be(^{16}O, ^{17}O)$ and $^9Be(^{19}F, ^{20}F)$ are 3.28, 2.48 and 4.94 MeV, respectively. Consequently these systems should be good candidates for large neutron-transfer yields to low-lying states at low bombarding energies. Angular distributions for the first two of these reactions have been studied earlier at energies near the barrier [15]). The Q-values for neutron transfer to the first excited states of ^{13}C and ^{17}O are 0.19 and 1.61 MeV, respectively, and these channels are expected to have still larger cross sections than the ground state neutron transfers. ^{20}F has a high density of low-lying states which may be selectively populated by neutron transfer.

Fig. 8 shows the measured excitation functions for the (^{12}C, ^{13}C*), (^{16}O, ^{17}O*) and (^{19}F, ^{20}F) reactions. Gamma-ray photopeaks were converted to cross sections using measured photopeak efficiencies as described earlier. In the (^{19}F, ^{20}F) case, which was studied by observing the ^{20}F decay, corrections were made for the decay of the ^{20}F prior to the counting period [21]). For the (^{12}C, ^{13}C*) reaction, γ-rays were observed from the decay of the 3.68 and 3.85 MeV excited states of ^{13}C, as well as from the 3.09 MeV first excited state, but the yields from the two higher states were negligible at the lowest energies and rose only to 6 % and 12 %, respectively, of the 3.09 MeV γ-yield at the highest beam energy used in the present work.

In order to describe the energy dependence of the data, we have used a very simple transfer model [20]) in which the cross section for a reaction of the type $a+A \rightarrow b+B$ is proportional to the square of the matrix element

$$M = \int_0^\infty F_{l\beta}(\kappa_\beta r)\exp(-\kappa r)F_{l\alpha}(\kappa_\alpha r)\mathrm{d}r,$$

between the regular Coulomb waves, F_l, in the entrance and exit channels, α and β, respectively. This integral was computed numerically for each partial wave, and the theoretical calculations, normalized to the data at low energies, are shown in fig. 8. For the case of the (^{19}F, ^{20}F) reaction, the calculation refers to the optimum Q-value case, only.

There is good agreement between the calculations and the data for the (^{12}C, ^{13}C*) and (^{16}O, ^{17}O*) reactions. The ability of such a simple model to describe low-energy transfer reactions has been noted earlier [4, 20]). The discrepancy at high energies in the (^{19}F, ^{20}F) case can be readily understood. Since the ground-state Q-value is 4.94 MeV and the density of low-lying states in ^{20}F is high, neutron transfers will occur to many levels of ^{20}F and our activation technique effectively sums all the contributions. Separate calculations show that at very low energies ($E_{\mathrm{c.m.}} \lessapprox 2$ MeV), only states with optimum Q-values are important. However, as the beam energy is increased, transfers to other levels become proportionally more significant. (The present discussion neglects the role of the detailed spectroscopy of the levels.) The net result will be an energy dependence of the yield which is somewhat steeper than that calculated for the optimum Q-value case, consistent with the observations. The energy dependence of the (^{12}C, ^{13}C) neutron-transfer process to the second and third excited states (which have non-optimum Q-value) are also calculated to be much steeper and this was experimentally observed.

Finally, we note that the evaporation of two α-particles from the compound nucleus will eventually become important at higher bombarding energies, rendering an unambiguous assignment of the measured ^{17}O* or ^{13}C* yields to the neutron-transfer process impossible. In order to estimate the energies at which this ambiguity might arise, we have performed optical model calculations of the total fusion cross sections (with the average potential parameters) [1, 13]) and have determined the energy at which the predicted fusion cross section was twice the measured neutron-transfer cross sections. For the systems ^{12}C+^{9}Be, ^{16}O+^{9}Be and ^{19}F+^{9}Be, these calculated energies were 4.0, 4.8 and 5.5 MeV, respectively. Our previous experience of the behavior of heavy-ion reactions, as well as an examination of Q-values, suggests that 2α evaporation will rarely comprise more than about 25 % of the total fusion cross section and usually much less. For the ^{16}O+^{9}Be reaction in particular, the discussion of sect. 3 indicates that the 2α reaction contributes less than 5 % to the fusion cross section in the energy range under investigation. Therefore, for the energy ranges studied in the present work, the observed yields of ^{17}O*, ^{13}C* and ^{20}F may be safely attributed to the neutron transfer reaction.

6. Conclusions

In the present work, experimental data have been obtained for ^{16}O+^{9}Be reactions extending down in energy to about half the interaction barrier. Neutron transfer was found to dominate the reaction yield below $E_{\text{c.m.}} = 4$ MeV, and, at the lowest energy studied, exceeded the extrapolated fusion yield by two orders of magnitude. This appears to be the first reported sub-barrier heavy-ion reaction where direct reactions greatly exceed the fusion process. The fusion S-factor was found to exhibit an energy dependence quite different from ^{12}C+^{13}C which forms the same intermediate compound nucleus. Both systems, ^{16}O+^{9}Be and ^{12}C+^{13}C, have favored neutron-transfer reactions, but the possible influence of such direct processes on the low-energy fusion yield is not clear from the present study.

Calculations of the reaction cross section have been presented using both an optical model and the IWB model where the potential parameters were deduced by fitting elastic scattering data. The results of the IWB calculations approximately account for the reaction cross section near the barrier and are in reasonable agreement with the fusion data at lower energies. The study of the ^{16}O+^{9}Be system where the reaction cross section may be characterized by both compound nucleus and direct components has provided an important test of the IWB model. It seems that the fusion interaction may be simply described by strong absorption. This feature is also evident in the deep imaginary potential which emerges from the OM calculations.

Neutron transfer data have been presented for ^{12}C, ^{16}O and ^{19}F projectiles incident on a ^{9}Be target. The near-optimum nature of the neutron transfer Q-values have enabled data to be taken down to extremely low energies. A satisfactory description of the neutron-transfer energy dependences is given by a simple Coulomb-wave Born approximation calculation.

We would like to thank Professors A. Winther and T. A. Tombrello and Dr. R. G. Stokstad for interesting and helpful discussions of this work.

References

1) R. G. Stokstad, Z. E. Switkowski, R. A. Dayras and R. M. Wieland, Phys. Rev. Lett. **37** (1976) 888
2) R. A. Dayras, R. G. Stokstad, Z. E. Switkowski and R. M. Wieland, Nucl. Phys. **A265** (1976) 153
3) W. A. Fowler, G. R. Caughlan and B. A. Zimmerman, Ann. Rev. Astron. and Astrophys. **13** (1975) 69
4) Z. E. Switkowski, R. G. Stokstad and R. M. Wieland, Nucl. Phys. **A274** (1976) 202
5) Z. E. Switkowski and R. A. Dayras, Nucl. Instr. **128** (1975) 9;
C. A. Barnes, J. C. Overley, Z. E. Switkowski and T. A. Tombrello, Appl. Phys. Lett., in press
6) F. Ajzenberg-Selove, Nucl. Phys. **A190** (1972) 1;
P. M. Endt and C. van der Leun, Nucl. Phys. **A214** (1973) 1
7) L. C. Northcliffe and R. F. Schilling, Nucl. Data Tables **A7** (1970)
8) B. Čujec and C. A. Barnes, Nucl. Phys. **A266** (1976) 461
9) H. Spinka and H. Winkler, Nucl. Phys. **A233** (1974) 456
10) P. R. Christensen, R. A. Dayras and Z. E. Switkowski, Nucl. Phys. **A280** (1977) 189
11) R. A. Dayras, R. G. Stokstad, Z. E. Switkowski and R. M. Wieland, Nucl. Phys. **A261** (1976) 478
12) C. A. Barnes, Advances in nuclear physics, vol. 4, ed. M. Baranger and E. Vogt (Plenum Press, NY, 1971) p. 133
13) G. J. Michaud, Phys. Rev. **C8** (1973) 525
14) M. D. High and B. Čujec, Nucl. Phys. **A259** (1976) 513
15) P. H. Barker, A. Huber, H. Knoth, U. Matter, A. Gobbi and P. Marmier, Nucl. Phys. **A155** (1970) 401
16) P. R. Christensen and A. Winther, Phys. Lett. **65B** (1976) 19
17) G. H. Rawitscher, Nucl. Phys. **35** (1963) 337
18) P. R. Christensen and Z. E. Switkowski, Nucl. Phys. **A280** (1977) 205
19) G. J. Michaud and E. W. Vogt, Phys. Rev. **C5** (1972) 350
20) Z. E. Switkowski, R. M. Wieland and A. Winther, Phys. Rev. Lett. **33** (1974) 840
21) S. Bashkin, R. W. Kavanagh and P. D. Parker, Phys. Rev. Lett. **3** (1959) 518

REFERENCES

Aj 72	Ajzenberg-Selove, F., Nucl. Phys. A214 (1972) 1
Aj 74	Ajzenberg-Selove, F. and T. Lauritsen, Nucl. Phys. A227 (1974) 1
Aj 77	Ajzenberg-Selove, F., Nucl. Phys. A281 (1977) 1
Al 56	Alder, K., A. Bohr, T. Huus, B. Mottelson, and A. Winther, Rev. Mod. Phys. 28 , 4 (1956) 432
Al 66a	Alder, B., S. Fernbach and M. Rotenberg, Methods in Computational Physics, Vol. 6, Acad. Press. (1966)
Al 66b	Alder, K. and A. Winther, Coulomb Excitation, Acad. Press. (1966)
An 61	Andreev, D. S., V. D. Vasilev, G. M. Gusinskii, K. I, Erokhina, and I. K. Lamberg, Izvestia Akad. Nauk. (USSR) Bull. Fiz. Ser. 25 (1961) 842
Ar 69	Arnett, W. D. and J. W. Truran, Ap. J. 157 (1969) 339
Ba 71	Barnes, C. A. Nucleosynthesis by Charge-Particle Reaction Advances in Nuclear Physics, Vol. 4 (1971) p. 133
Ba 77	Barnes, C. A., J. C. Overley, Z. E. Switkowski, and T. A. Tombrello, Appl. Phys. Lett. 31 (1977) 239
Be 69	Bechetti, F. D. Jr. and G. W. Greenlees, Phys. Rev. 182 (1969) 1190
Bo 74	Boydell, S. Y.,Ph.D. Thesis, Univ. of Melbourne (1974), unpublished.
Bo 78	Bonche, P., Private Communication (1978)

Ch 77a Christensen, P. R., Z. E. Switkowski and R. A. Dayras, Nucl. Phys. A280 (1977) 189

Ch 77b Christensen, P. R. and Z. E. Switkowski, Nucl. Phys. A280 (1977) 205

Ch 78a Cheng, V. K. C., A. Little, H. C. Yuen, S. M. Lazarus and S. S. Hanna, to be published,and Stanford Univ. Progress Report, (1977), unpublished

Ch 78b Chung, H. C., M. D. High and B. Čujec, Nucl. Phys. A296 (1978) 333

Ci 77 Cindro, N., F. Cocu, J. Uzureau, Z. Basrak, M. Cates, J. M. Fieni, E. Holub, Y. Patin and S Plattard, Phys. Rev. Lett. 39 (1977) 1135

Cl 68 Clayton, D. D., Principles of Stellar Evolution and Nucleosynthesis, McGraw-Hill, Inc. (1968)

Co 74 Conlon, T. W., Nature 247 (1974) 268

Ču 76 Čujec, B. and C. A. Barnes, Nucl. Phys. A266 (1976) 461

Da 76a Dayras, R. A., R. G. Stokstad, Z. E. Switkowski and R. M. Wieland, Nucl. Phys. A261 (1976) 478

Da 76b Dayras, R. A., R. G. Stokstad, Z. E. Switkowski and R. M. Wieland, Nucl. Phys. A265 (1976) 153

Di 73 Dilg, W., W. Schantl, H. Vonach and M. Uhl, Nucl. Phys. A217 (1973) 269

Dy 74 Dyer, P. L. and C. A. Barnes, Nucl. Phys. A233 (1974) 495

Ei 72 Eisen, Y., E. Albramson, G. Engler, M. Smilansky and Z. Vager, Nucl. Phys. A236 (1972) 327

En 74 Endt, P. M. and C. Van der Leun, Nucl. Phys. A214 (1973) 1

Ey 76 Eyal, Y., M. Beckerman, R. Chechik, Z. Fraenkel and H. Stocker, Phys. Rev. C13 (1976) 1527

Fo 64 Fowler, W. A. and F. Hoyle, Ap. J. Supp. No. 91, 9 (1964) 201

Gi 65 Gibert, A. and A. G. W. Cameron, Can. J. Phys. 43 (1965) 1446

Go 73 Gobbi, A., R. Wieland, L. Chua, D. Shapira and D. A. Bromley, Phys. Rev. C7 (1973) 30

Ha 52 Hauser, W. and H. Feshbach, Phys. Rev. 87 (1952) 366

Hi 76 High, M. D. and B. Čujec, Nucl. Phys. A259 (1976) 513

Hi 77a High, M. D. and B. Čujec, Nucl. Phys. A278 (1977) 149

Hi 77b High, M. D. and B. Čujec, Nucl. Phys. A282 (1977) 181

Ig 59 Igo, G., Phys. Rev. 115 (1959) 1665

Ke 74 Kern, J., *Gamma Standards , in Charged Particle-Induced Radiative Capture* (Intern. Atomic Energy Agency, Vienna), (1974) p. 345

Ke 77 Kettner, K. -U., H. Lorenz-Wirzba, C. Rolfs and H. Winkler, Phys. Rev. Lett. 38 (1977) 377

Ko 70 Kozlousky, B. -Z., Astrophys. Space Sci. 8 (1970) 144

Ko 77 Kolata, J. J., R. C. Fuller, R. M. Freeman, F. Haas, B. Heusch and A. Gallmann, Phys. Rev. C16 (1977) 891

Ma 68 Marion, J. B. and F. C. Young, *Nuclear Reaction Analysis*, North-Holland Publishing Com. (1968)

Ma 73 Mazarakis, M. G. and W. E. Stephens, Phys. Rev. C7 (1973) 1280

Ma 74 Marquardt, N., R. Volders, C. Cardinal and J. L'Eaiyer, Phys. Rev. Lett. 33 (1974) 1389

Ma 75a Mann, F. Ph.D. Thesis, California Institute of Technology (1975) unpublished

Ma 75b Mann, F. and R. W. Kavanagh, Nucl. Phys. A255 (1975) 287

Ma 76a Mann, F., Hanford Engineering and Development Laboratories Report No HEDL-TIME-7680 (1976) unpublished

Ma 76b Mann, F. D. W. Kneff, Z. E. Switkowski and S. E. Woosley, Nucl. Phys. A256 (1976) 163

Mc 66 McFadden, L. and G. R. Satchler, Nucl. Phys. 84 (1966) 177

Mc 75 McCallum, G. J. and G. E. Coote, Nucl. Instr. and Methods 124 (1975) 309

Me 69 Meyer, M. A. and N. S. Wolmarans, Nucl. Phys. A136 (1969) 663

Mi 72 Michaud, G. J. and E. W. Vogt, Phys. Rev. C5 (1972) 350

Mi 73 Michaud, G. J., Phys. Rev. C8 (1973) 525

No 70 Northcliffe, L. C. and R. F. Schilling, Nucl. Data Table A7 (1970) no.3

Ol 74 Olmer, C., R. G. Stokstad, D. L. Hanson, K. A. Sachs and D. A. Bromley, Phys. Rev. C10 (1974) 1722

Ov 61 Overley, J. C., Ph.D. Thesis, California Institute of Technology (1961), unpublished

Ov 62 Overley, J. C. and W. Whaling, Phys. Rev. 128 (1962) 315

Pa 69 Patterson, J. R., H. Winkler and C. S. Zaidins, Ap. J. 157 (1969) 367

Po 62 Powell, J. L. and B. Chasemann, Quantum Mechanics, Addison-Wesley Publishing Com. (1962)

Pü 77 Pühlhofer, F., Nucl. Phys. A280 (1977) 267

Ra 63 Rawitscher, G. H., Nucl. Phys. 85 (1963) 337

Sp 74 Spinka, H. and H. Winkler, Nucl. Phys. A233 (1974) 456

St 74 Stokstad, R. G., Proc. Int. Conf. on Reactions between Complex Nuclei, Nashville, Tenn., June 10-14 (1974)

St 76 Stokstad, R. G., Z. E. Switkowski, R. A. Dayras and R. M. Wieland, Phys. Rev. Lett. 37 (1976) 888

Sw 74 Switkowski, Z. E., R. M. Wieland and A. Winther, Phys. Rev. Lett. 33 (1974) 840

Sw 75 Switkowski, Z. E. znd R. A. Dayras, Nucl. Instr. and Meth. 128 (1975) 9

Sw 76 Switkowski, Z. E., R. G. Stokstad and R. M. Wieland, Nucl. Phys. A274 (1976) 202

Sw 77a Switkowski, Z. E., R. G. Stokstad and R. M. Wieland, Nucl. Phys. A279 (1977) 502

Sw 77b Switkowski, Z. E. and S. -C. Wu, (1977) unpublished

Vo 64 Vogt, E. W., D. McPherson, J. Kuehner and E. Almqvist, Phys. Rev. 136 (1964) B99

Wa 77 Wapstra, A. H. and K. Bos, Atomic Data and Nuclear Data Tables 19 (1977) 177

We 76 Weidinger, A, F. Buch, G. Gaul, W. Trautmann and W. Zipper, Nucl. Phys. A263 (1976) 511

Table 1

Fusion γ-ray Photopeak Identification for the ^{14}N + ^{10}B Reaction

For the γ-ray spectrum shown in fig. 6, the numbered peaks are identified as follows. The peaks used in the cross section determinations are marked with an asterisk. Because of the ^{12}C and ^{16}O impurities in the ^{10}B target, the ^{22}Na residual nucleus (peaks #1, 11,14, 17, 18, 19, 20) may also be formed by the reaction $^{12}C(^{14}N,\alpha)^{22}Na$. The nucleus ^{24}Mg (peak #17) may be formed by the reaction $^{12}C(^{14}N, pn)^{24}Mg$, and ^{25}Mg (peak #11) may be formed through either $^{12}C(^{14}N,p)^{25}Mg$ or $^{16}O(^{14}N, \alpha p)^{25}Mg$. The 6.13 MeV γ-ray peak from ^{16}O,and its escape peaks also, are not included in figure 6. For additional details, see page 14, 18.

Peak#	E_γ (keV)	Reaction Products	Peak#	E_γ (keV)	Reaction Products
1	74	^{22}Na(2 → 1) + pn	12	671	^{63}Cu Coulomb Exc.
		Pb X-ray	13	718	^{10}B Coulomb Exc.
2	85	Pb X-ray	14*	890	^{22}Na(3 → 0) + pn
3*	110	^{19}F(1 → 0) + αp	15	1233	^{19}F(3 → 1) + αp
4*	197	^{19}F(2 → 0) + αp		1236	^{19}Ne(3 → 2) + αn
5*	238	^{19}Ne(1 → 0) + αn	16*	1275	^{22}Ne(1 → 0) + pp
6*	275	^{19}Ne(2 → 0) + αn	17	1369	^{22}Na(6 → 1) + pn
7*	351	^{21}Ne(1 → 0) + ppn		1369	^{24}Mg(1 → 0)
8*	440	^{23}Na(1 → 0) +p	18	1400	^{22}Na(7 → 1) + pn
9*	451	^{23}Mg(1 → 0) + n	19	1528	^{22}Na(4 → 0) + pn
10	511	β^+ annihilation	20	1554	^{22}Na(8 → 2) + pn
11*	583	^{22}Na(1 → 0) + pn	21	1634	^{20}Ne(1 → 0) + α
	585	^{25}Mg(1 → 0)	_*	6131	^{16}O(2 → 0) + $\alpha\alpha$

Table 2

Relative Intensities of the γ-ray Used in the Photopeak Efficiency Calibration

(A) The relative γ-ray intensities produced by a ^{56}Co source are given below. The intensities are taken from Nucl. Inst. and Methods 124 (1975) 309. For details, see pages 24 and 73.

(B) The decay branching ratios for the 12.54 MeV state of ^{28}Si nucleus (the resonance at E_p = 992 keV from the reaction of ^{27}Al(p,γ)) are given below. The branching ratios were measured by Boydell (Bo 74). For additional details, see page 24.

(A)

Gamma-ray intensities from a ^{56}Co source

E (MeV)	Relative Intensity
0.847	1000.0
1.038	133.4
1.175	21.2
1.238	686.0
1.360	42.7
1.772	157.2
2.015	29.8
2.305	77.7
2.559	175.1
3.202	33.6
3.254	81.2
3.273	18.1
3.451	9.6
3.548	2.0

(B)

Branching ratios for the 12.54 MeV state of ^{28}Si

Final State (MeV)	Branching Ratio
1.78	(80 ± 3.3)%
4.62	(5 ± 0.5)%
6.28	(2.3 ± 0.2)%
7.78	(9.1 ± 0.3)%
7.93	(4.2 ± 0.2)%

Table 3

Summing Branching Correction Factors for the $^{14}N + ^{10}B$ Reaction

The summing and branching correction factors, β are defined as the probability that a particular γ-ray (E_γ) is emitted after the residual nucleus is formed, and that no other member of a deexcitation cascade from the same residue is detected in coincidence in the detector. Column 3 lists the number of levels considered in the calculation of the β's. Usually levels with energies up to 2 MeV above the first particle emission thresholds are included in this calculation. For the ^{16}O nucleus, five unnatural parity states between 10 and 13 MeV were included in the evaluations of the β's. Values of β calculated from the statistical model are given in column 5 and 6. Most of these differ by only a few percent from the β- valus in column 4, which were calculated by assuming a (2J +1) population for the bound states of each residual nucleus. For additional details, see page 28.

Residual Nucleus	E_γ (keV)	No. of levels considered	$\beta_{(2J+1)}$	$\beta_{\text{Statistical}}$	
				E_{cm} = 2.5 MeV	E_{cm} = 7.5 MeV
^{16}O	6131	11	0.498	0.436	0.474
^{19}F	110	16	.312	.337	.321
	197	16	.517	.486	.505
^{19}Ne	238	8	.521	.530	.529
	275	8	.251	.228	.317
^{20}Ne	1634	8	.867	.874	.874
^{21}Ne	351	10	.674	.473[a)]	.648
^{22}Ne	1275	10	.839	.840	.839
^{22}Na	583	16	.463	.393	.451
	890	16	.158	.186	.163
^{23}Na	440	12	.608	.608	.608
^{23}Mg	451	8	.658	.642	.642

a) E_{cm} = 4 MeV

Table 4

The Optical Model Parameters

The optical model potential employed in the statistical model calculation has the form,

$$U(r) = -Vf(r,R_r,a_r) - iW_vf(r,R_v,a_v) + 4ia_sW_s\frac{d}{dr} f(r,R_s,a_s)$$

where $f(r,R_i,a_i) = [1 + \exp((r-R_i)/a_i)]^{-1}$,

and $R_i = r_iA^{1/3}$ for $i = r,v,s.$

Z and A are the atomic number and total number of nucleons in the target nucleus, and N = A - Z. The Coulomb potential is the potential given by a sphere of uniform volume charge density of radius $r_cA^{1/3}$. For more details, see pages 30 and 85.

Protons (parameters from Bechetti and Greenlees)

$V = 54 - 0.32E + 24(N - Z)/A + 0.4\ Z/A^{1/3}$ (MeV)

$r_r = r_c = 1.17$ (fm)

$a_r = 0.75$ (fm)

$W_s = 11.8 - 0.25\ E + 12(N - Z)/A$ (MeV)

$W_v = 0$

$r_s = 1.32$ (fm)

$a_s = 0.51 + 0.7(N - Z)/A$ (fm)

Neutrons (parameters from Bechetti and Greenlees)

$V = 56.3 - 0.32\ E - 24(N - Z)/A$ (MeV)

$r_r = r_c = 1.17$ (fm)

$a_r = 0.75$ (fm)

$W_s = 13 - 0.25\ E - 12(N - Z)/A$ (MeV)

$W_v = 0$

$r_s = 1.26$ (fm)

$a_s = 0.58$ (fm)

Alphas (parameters from McFadden and Satchler)

$V = 185$ (MeV)

$r_r = r_c = 1.40$ (fm)

$a_r = 0.52$ (fm)

$W_v = 25$ (MeV)

$W_s = 0$

$r_v = 1.40$ (fm)

$a_v = 0.52$ (fm)

Table 5

Optical Model Parameters for $^{14}N + ^{10}B$ Reaction

The potential parameters needed in the optical model were summarized in table 4. The values used as input information in the computer code HAUSER*4, in order to evalute the transmission coefficients of the $^{14}N + ^{10}B$ reactions, are given below. For definitions of each parameter, see table 4. All potentials (V, W) are given in MeV, while radii (r) and diffusenesses (a) are given in fm (1 fm = 10^{-13}cm). For additional details, see page 30

Channel	V	W_v	W_s	r ($r_{r,v,c}$)	r_s	a($a_{r,v}$)	a_s
$^{14}N + ^{10}B$	50	10		2.68		0.40	
$\alpha + ^{20}Ne$	185	25		1.40		0.52	
$p + ^{23}Na$	56.59-0.32E		12.32-0.25E	1.17	1.32	0.75	0.54
$n + ^{23}Mg$	57.34-0.32E		13.52-0.25E	1.17	1.26	0.75	0.58
$\alpha + ^{16}O$	185	25		1.40		0.52	
$\alpha + ^{19}F$	185	25		1.40		0.52	
$\alpha + ^{19}Ne$	185	25		1.40		0.52	
$p + ^{19}F$	56.61-0.32E		12.43-0.25E	1.17	1.32	0.75	0.55
$p + ^{22}Ne$	57.61-0.32E		12.89-0.25E	1.17	1.32	0.75	0.57
$p + ^{22}Na$	55.57-0.32E		11.8-0.25E	1.17	1.32	0.75	0.51
$n + ^{19}Ne$	57.56-0.32E		13.63-0.25E	1.17	1.26	0.75	0.58
$n + ^{22}Na$	56.30-0.32E		13.0-0.25E	1.17	1.26	0.75	0.58

Table 6

Level Density Parameters for the $^{14}N + ^{10}B$ Reactions

The definitions of the level density parameters tabulated below are given in section III.1 of part II. For additional information, see pages 31 and 87.

Nucleus	T (MeV)	E_0 (MeV)	U' (MeV)	a $(MeV)^{-1}$	Δ (MeV)
^{16}O	3.09	2.74	11.9	2.40	7.08
^{19}F	2.96	-3.89	10.4	2.15	-0.68
^{19}Ne	3.85	-6.05	10.4	1.70	-3.99
^{20}Ne	2.61	1.65	10.0	2.84	5.02
^{22}Ne	2.70	-2.21	9.3	2.27	-0.02
^{22}Na	2.68	-3.75	9.3	2.66	-1.08
^{23}Na	2.16	-0.54	9.0	3.57	2.67
^{23}Mg	1.92	0.37	9.0	4.25	4.00

Table 7

Calculated Cross Sections for the Formation of ^{28}Si Excited States from the ^{16}O + ^{16}O Reaction

The cross sections for $^{16}O(^{16}O,\alpha_i)^{28}Si$ at E_{cm} = 6 MeV, calculated with the computer code HAUSER*4, are listed in column 2. Columns 3 and 4 list the excitation energy, and the spin and parity for each state of ^{28}Si, included in the cross section calculations. The deviations of the ratio $(\frac{\sigma}{2J+1} / \frac{\sigma_0}{2J_0+1})$ (given in column 5) from unity reflect the decrease in transmission coefficients arising from the decrease in kinetic energy for the α-particles. For additional details, see page 31.

E_{cm}(MeV)	σ(barns)	E_x(MeV)	J^π	$(\frac{\sigma}{2J+1} / \frac{\sigma_0}{2J_0+1})$
6.00	.44413E-05	0.000	0^+	1.0000
6.00	.18257E-04	1.779	2^+	0.8221
6.00	.22962E-04	4.618	4^+	0.5745
6.00	.29499E-05	4.979	0^+	0.6642
6.00	.14308E-04	6.277	3^+	0.4602
6.00	.22897E-05	6.691	0^+	0.5155
6.00	.11855E-04	6.879	3^-	0.3813
6.00	.14375E-04	6.889	4^+	0.4347
6.00	.84207E-05	7.381	2^+	0.3792
6.00	.83666E-05	7.417	2^+	0.3768
6.00	.10041E-04	7.799	3^+	0.3230
6.00	.76888E-05	7.933	2^+	0.3462
6.00	.65597E-05	8.259	2^+	0.2954
6.00	.39273E-05	8.328	1^+	0.2948
6.00	.89523E-05	8.413	4^-	0.2240
6.00	.98674E-05	8.543	6^+	0.1709
6.00	.62429E-05	8.589	3^+	0.2008
6.00	.26832E-05	8.904	1^-	0.2014

Table 8

Calculated Bound State Fractions for the ^{16}O Residual Nucleus as Produced in the Reaction ^{14}N + ^{10}B

The bound state fractions, defined in section III.3, were calculated in two different ways: First, by using the actual observed levels of ^{16}O, and classifying them as bound or unbound according to whether they can decay by α-emission. Secondly, by using a level density formula (calculated with the parameters given in Table 6) and treating all unnatural parity states as bound. E_{cm} refers the center of mass energy for ^{14}N + ^{10}B entrance channel and F_1 and F_2 refer to the two methods of treating the level density. For details, see page 38.

E_{cm}(MeV)	F_1	F_2
3.0	0.92	0.92
4.0	0.86	0.87
5.0	0.77	0.81
6.0	0.68	0.75
7.0	0.60	0.70
7.5	0.56	0.68

Table 9

$^{14}N + ^{10}B$ Reaction Cross Sections

The cross sections for the production of each fusion residue are given. The cross sections are given in barns and the number in parentheses is the power of ten. For details, see pages 33, 35 and 38.

E_{cm}	Partial Cross Sections (b)									σ_{fus}
(MeV)	^{16}O	^{19}F	^{19}Ne	^{20}Ne	^{21}Ne	^{22}Ne	^{22}Na	^{23}Na	^{23}Mg	(b)
2.89	1.76(-6)	1.09(-6)					9.27(-7)	1.79(-7)		4.07(-6)
3.10		2.43						5.90		
3.22	2.43	3.46		5.05(-7)		4.36(-7)	2.43(-6)	1.26(-6)		1.07(-5)
3.31	6.14	4.93		7.83		1.67(-6)	4.18	2.48	9.06(-8)	2.09
3.39	9.78	7.71		7.39		2.95	7.21	2.72	5.52(-7)	3.26
3.47	1.61(-5)	1.14(-5)		1.01(-6)		3.42	1.10(-5)	4.08	6.78	5.21
3.56	2.28	1.37		2.11		6.75	1.83	6.94	8.81	7.47
3.64	3.64	2.10	3.22(-6)	3.00		1.09(-5)	2.80	8.72	1.41(-6)	1.15(-4)
3.72	4.79	3.37	3.99	4.55	4.00(-6)	1.68	3.86	1.42(-5)	2.09	1.72
3.81	7.39	4.96	4.39	9.46	7.15	2.28	6.98	1.79	2.53	2.68
3.89	1.12(-4)	6.81	7.78	1.05(-5)	4.52	3.46	9.38	2.64	6.80	3.81
3.97	1.71	1.04(-4)	1.14(-5)	1.47	9.91	5.23	1.29(-4)	3.76	5.56	5.64
4.06	2.47	1.53	1.86	1.76	1.34(-5)	7.14	2.00	4.94	1.19(-5)	8.25
4.14	3.57	2.15	2.38	2.70	2.33	1.03(-4)	2.70	6.96	1.22	1.17(-3)
4.23	4.67	3.02	3.79	4.39	3.17	1.39	3.85	9.40	1.57	1.61
4.31	5.86	4.18	5.19	5.30	5.41	1.99	5.42	1.36(-4)	2.76	2.19
4.39	8.00	5.75	6.63	7.37	5.85	2.90	7.11	1.77	3.02	2.96
4.48	1.12(-3)	7.60	1.02(-4)	8.23	9.32	3.61	9.75	2.28	4.28	4.03

Table 9

E_{cm} (MeV)	Partial Cross Sections (b)									σ_{fus}
	^{16}O	^{19}F	^{19}Ne	^{20}Ne	^{21}Ne	^{22}Ne	^{22}Na	^{23}Na	^{23}Mg	(b)
4.56	1.44	1.03(-3)	1.41	1.32(-4)	1.25(-4)	4.80	1.29(-3)	3.03	5.82	5.34
4.64	1.94	1.34	1.80	1.60	1.55	6.03	1.69	3.83	7.99	7.03
4.73	2.34	1.72	2.19	2.10	2.32	8.01	2.23	4.91	8.89	8.98
4.81	2.85	2.23	2.97	2.40	3.01	9.97	2.82	6.13	1.12(-4)	1.13(-2)
4.89	3.89	2.80	3.75	2.97	3.91	1.27(-3)	3.59	7.54	1.65	1.47
4.98	4.78	3.60	5.04	3.87	5.42	1.63	4.36	9.56	1.93	1.85
5.06	5.52	4.31	6.18	4.55	6.60	1.97	5.48	1.11(-3)	2.34	2.24
5.14	6.95	5.20	7.46	5.65	8.41	2.39	6.75	1.33	2.94	2.75
5.23	7.32	6.35	9.24	6.89	9.98	2.90	8.20	1.61	3.67	3.21
5.31	9.84	7.66	1.12(-3)	7.99	1.30(-3)	3.41	9.73	1.89	4.11	4.00
5.39	1.14(-2)	9.12	1.33	9.03	1.60	4.02	1.16(-2)	2.17	4.55	4.72
5.48	1.34	1.08(-2)	1.60	1.13(-3)	1.94	4.43	1.35	2.49	5.40	5.54
5.56	1.59	1.26	1.95	1.26	2.40	5.51	1.58	2.85	6.75	6.59
5.65	1.86	1.46	2.29	1.44	2.82	6.43	1.81	3.14	8.02	7.68
5.73	2.10	1.68	2.66	1.65	3.36	7.41	2.06	3.59	8.57	8.80
5.81	2.39	1.97	3.23	1.80	4.19	8.28	2.33	4.15	1.05(-3)	1.02(-1)
5.90	2.64	2.22	3.69	2.15	5.04	9.23	2.64	4.68	1.09	1.15
5.98	2.90	2.49	4.08	2.44	5.86	1.06(-2)	2.95	5.06	1.25	1.28
6.06	3.22	2.77	4.60	2.42	6.92	1.21	3.29	5.40	1.37	1.44

Table 9 (continued)

E_{cm}	Partial Cross Sections (b)									
(MeV)	^{16}O	^{19}F	^{19}Ne	^{20}Ne	^{21}Ne	^{22}Ne	^{22}Na	^{23}Na	^{23}Mg	(b)
6.15	3.56	3.06	5.04	2.79	8.01	1.30	3.55	5.96	1.46	1.59
6.23	3.75	3.35	5.73	2.87	9.29	1.40	3.78	6.41	1.75	1.72
6.31	4.31	3.69	6.36	3.35	1.06(-2)	1.54	4.40	6.77	1.71	1.95
6.40	4.35	4.03	7.06	3.75	1.19	1.72	4.58	7.14	1.88	2.07
6.48	5.14	4.27	7.64	3.82	1.33	1.79	5.04	7.78	2.16	2.31
6.56	5.20	4.61	8.38	3.84	1.47	1.93	5.63	8.49	2.40	2.48
6.65	5.80	4.93	9.04	4.27	1.74	2.08	6.10	8.60	2.28	2.73
6.73	6.09	5.26	9.41	3.64	1.93	2.17	6.63	8.85	2.67	2.91
6.81	6.19	5.60	1.06(-2)	4.30	2.08	2.30	7.01	9.03	2.40	3.07
6.90	6.81	5.92	1.04	5.45	2.24	2.43	7.47	9.94	2.60	3.32
6.98	6.89	6.20	1.17	5.28	2.45	2.53	7.79	1.00(-2)	2.75	3.47
7.06	7.57	6.48	1.24	5.16	2.62	2.62	8.51	1.04	2.65	3.74
7.15	7.75	6.77	1.27	5.56	2.73	2.70	8.49	1.09	3.03	3.87
7.23	8.09	7.12	1.38	6.04	2.99	2.78	9.22	1.12	2.73	4.11
7.32	8.48	7.42	1.43	6.56	3.29	2.93	9.46	1.21	2.92	4.33
7.40	8.69	7.67	1.44	6.28	3.53	2.93	9.84	1.16	2.75	4.49
7.48	9.10	7.93	1.62	7.01	3.62	3.14	1.02(-1)	1.21	3.12	4.72

Table 9 (continued)

Table 10

Identification of the Gamma-rays from the $^{16}O + ^{16}O$ Reactions

The γ-ray transitions observed in the $^{16}O + ^{16}O$ reactions, as full energy peaks in the spectrum of fig. 23, are identified in this table. In the terminology $^{16}O + ^{16}O \rightarrow X + Y$, X denotes the evaporated light particle, while Y is the heavy residue. For more details, see page 70.

E (keV)	X	Y	Transition of Y	Possible contamination
511			β^+ annihilations	
677	pn	^{30}P	1 → 0	
709	pn	^{30}P	2 → 0	
844	αp	^{27}Al	1 → 0	$^{12}C(^{16}O,p)^{27}Al$
1014	αp	^{27}Al	2 → 0	$^{12}C(^{16}O,p)^{27}Al$
1248	n	^{31}S	1 → 0	
1263	2p	^{30}Si	2 → 0	
1264	pn	^{30}P	4 → 0	
1266	p	^{31}P	1 → 0	
1369	2α	^{24}Mg	1 → 0	$^{12}C(^{16}O,\alpha)^{24}Mg$
1454	pn	^{30}P	3 → 0	
1779	α	^{28}Si	1 → 0	
1973	pn	^{30}P	4 → 0	
2232	n	^{31}S	2 → 0	
2234	p	^{31}P	2 → 0	
2236	2p	^{30}Si	1 → 0	
3498	2p	^{30}Si	2 → 0	

Table 11

Optical Model Parameter for $^{16}O + ^{16}O$ Reactions

The optical model potential parameters were defined in table 4. The values used as input parameters to evaluate the transmission coefficients of the $^{16}O + ^{16}O$ reaction are given below. All potentials (V, W) are given in MeV, while the radii (r) and diffusenesses (a) are given in fm. For additional details, see page 85.

Channel	V	W_v	W_s	$r(r_{r,v,c})$	r_s	$a(a_{r,v})$	a_s
$^{16}O+^{16}O$	50	10		2.639		0.40	
$\alpha+^{28}Si$	185	25		1.40		0.52	
$p+^{31}P$	56.68-0.32E		12.19-0.25E	1.17	1.32	0.75	0.53
$n+^{31}S$	57.07-0.32E		13.39-0.25E	1.17	1.26	0.75	0.58
$\alpha+^{24}Mg$	185	25		1.40		0.52	
$\alpha+^{27}Al$	185	25		1.40		0.52	
$\alpha+^{27}Si$	185	25		1.40		0.52	
$p+^{27}Al$	56.62-0.32E		12.24-0.25E	1.17	1.32	0.75	0.54
$p+^{30}Si$	57.4-0.32E		12.6-0.25E	1.17	1.32	0.75	0.56
$p+^{30}P$	55.93-0.32E		11.8-0.25E	1.17	1.32	0.75	0.51
$n+^{27}Si$	57.19-0.32E		13.44-0.25E	1.17	1.26	0.75	0.58
$n+^{30}P$	56.3-0.32E		11.8-0.25E	1.17	1.26	0.75	0.58

Table 12

Level Density Parameters for the $^{16}O + ^{16}O$ Reactions

The definitions of the level density parameters are given in section III.1 of part II. The parameters needed in the statistical model calculation of the residual nuclei produced by the $^{16}O + ^{16}O$ reaction are listed below. For additional information, see page 86.

Nucleus	T (MeV)	E_0 (MeV)	U' (MeV)	a $(MeV)^{-1}$	Δ (MeV)
^{24}Mg	2.33	2.12	8.75	3.15	4.80
^{27}Al	2.30	-1.52	8.06	3.11	0.58
^{27}Si	2.02	-0.64	8.06	3.75	1.92
^{28}Si	2.48	1.70	7.86	2.78	3.35
^{30}Si	2.61	-1.03	7.50	2.54	0.09
^{30}P	2.01	-0.73	7.50	3.64	1.33
^{31}P	1.93	-0.19	7.34	3.82	1.86
^{31}S	2.04	-0.57	7.34	3.53	1.29

Table 13

$^{16}O + ^{16}O$ Reaction Cross Sections

The cross sections for the production of residual nuclei are listed below. The cross sections for ^{24}Mg and ^{27}Al for $E_{cm} \leq 10$ MeV were determined by first calculating relative cross sections with a statistical model calculation, and then normalizing to the cross sections measured at higher energy. Total fusion cross sections were obtained by directly summing the cross sections for the various residual nuclei. For additional details, see pages 93 to 102.

E_{cm} (MeV)	Cross Sections (mb)								
	^{28}Si	^{31}P	^{31}S	^{24}Mg	^{27}Al	^{30}Si	^{30}P	σ_{tot}	S(MeV-b)
7.00	0.00309	0.00357	0.000381			0.000743	0.00243	0.0104	1.86(25)
7.25	0.00816	0.00867	0.000769			0.00828	0.00646	0.0332	1.89
7.50	0.0297	0.0248	0.00449			0.0325	0.0143	0.109	2.09
7.75	0.0712	0.0661	0.00831			0.0944	0.0384	0.289	1.98
8.00	0.170	0.150	0.0282			0.263	0.102	0.747	1.92
8.25	0.326	0.306	0.0521			0.576	0.201	1.54	1.56
8.50	0.575	0.516	0.0827			1.03	0.386	2.80	1.15
8.75	1.097	0.966	0.160			1.84	0.687	5.24	9.16(24)
9.00	1.70	1.55	0.246			3.05	1.10	8.78	6.78
9.25	3.00	2.71	0.390			5.78	2.25	16.3	5.73
9.50	4.40	3.97	0.632			8.79	3.81	25.6	4.25
9.75	6.29	5.24	0.888			13.0	5.94	38.8	3.11
10.00	8.29	8.15	1.03	4.43	12.4	16.7	8.26	56.9	2.28
10.25	11.4	11.3	1.45		15.5	23.0	12.3	78.1	1.60
10.50	16.0	16.4	1.82	7.27	29.2	31.8	17.4	117.	1.26
10.75	18.1	17.9	2.62		40.4	36.9	22.2	145.	8.34(23)
11.00	22.0	22.8	2.92	12.3	57.1	50.4	30.6	196.	6.19
11.25	27.8	28.3	3.25		75.4	58.9	37.9	249.	4.39
11.50	34.2	30.2	4.06	17.1	98.2	76.7	47.3	308.	3.10
11.75	39.9	37.0	4.02	20.1	135.	88.1	58.6	379.	2.21
12.00	46.3	42.7	4.03	22.7	150.	100.	72.1	438.	1.51

Figure 1

The Reaction S-factor of the ^{12}C + ^{12}C Reaction

The filled circles are the data of Spinka and Winkler (Sp 74), while the open circles were measured by High and Čujec (Hi 77b). Strong resonant structure was observed at, and below the Coulomb barrier ($E_B \simeq 6$ MeV). For details, see page 2.

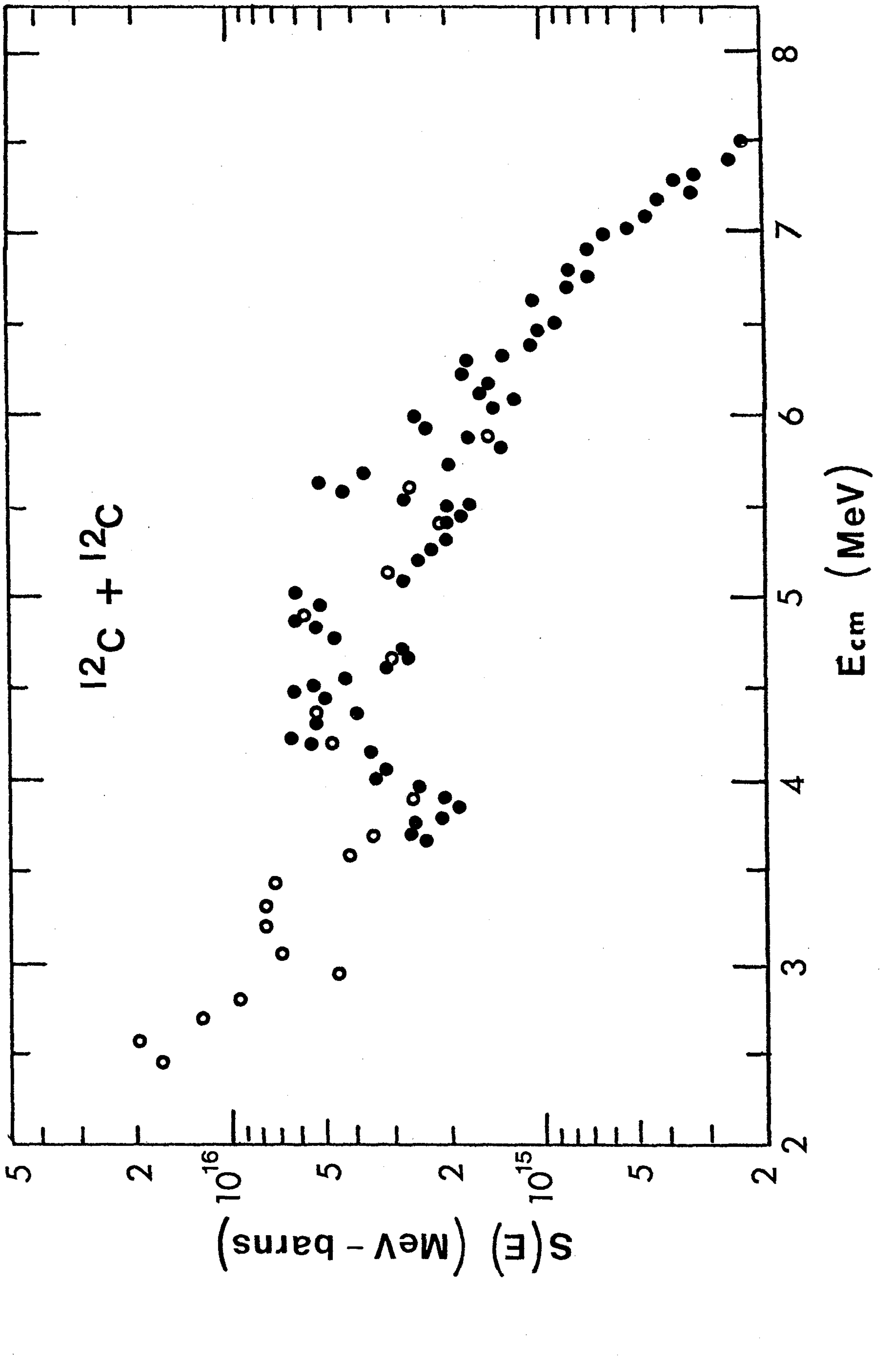

$^{12}C + ^{12}C$
S(E) (MeV - barns)
5
2
10^{16}
5
2
10^{15}
5
2
2
3
4
5
6
7
8
E_{cm} (MeV)

Figure 2

Partial Q-value Scheme for the Open Reaction Channels Intiated by ^{14}N + ^{10}B Fusion

The cross-hatched area represents the region of excitation in ^{24}Mg populated in the present work. All one-, two- and three-particle evaporation channels which are allowed by the reaction Q-values are shown. The dominant γ-ray transitions observed in the deexcitation of the evaporation residues are indicated by arrows. For details, see page 3.

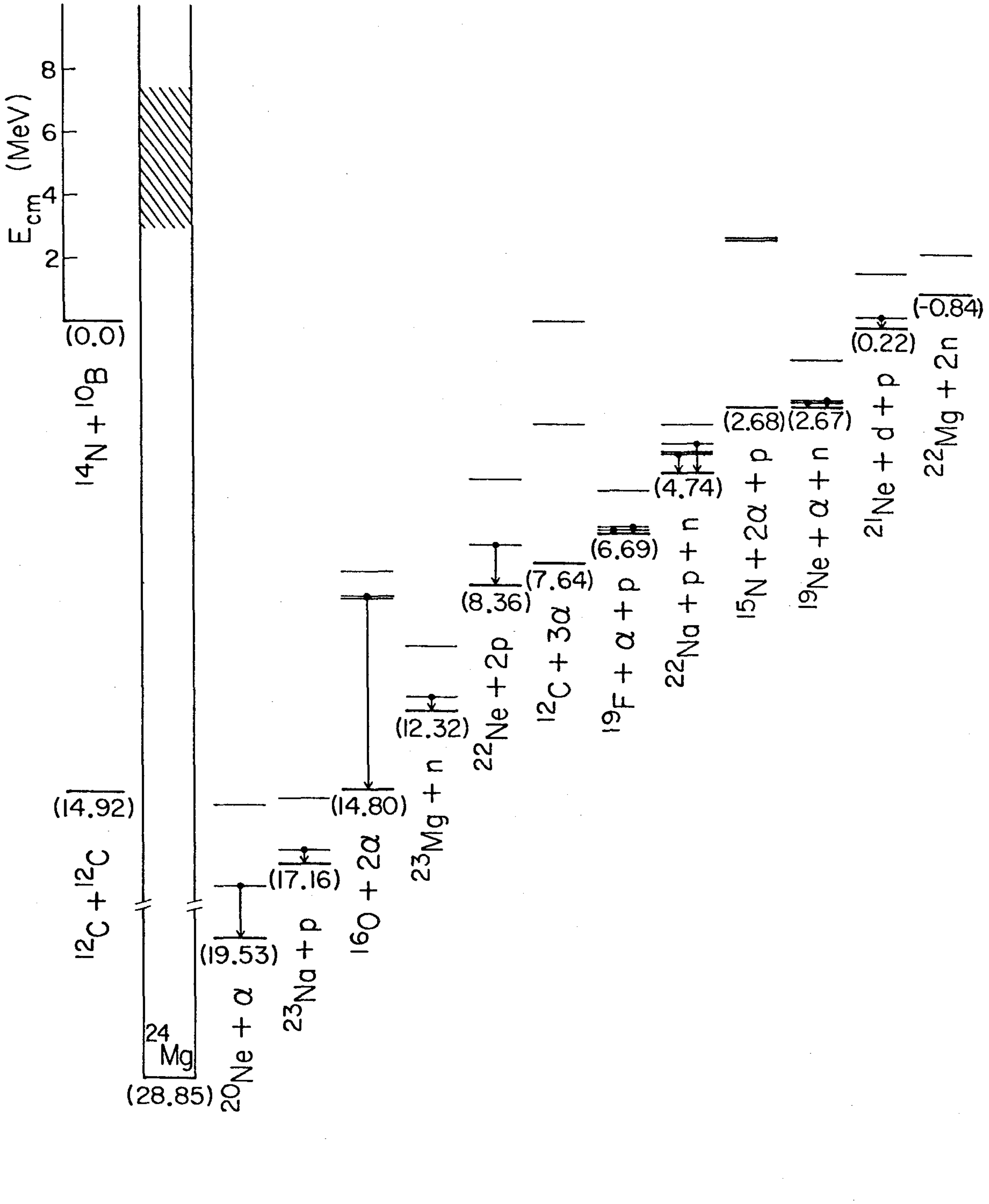
E_{cm} (MeV)
2
4
6
8
(0.0)
$^{14}N + ^{10}B$
(14.92)
$^{12}C + ^{12}C$
^{24}Mg
(28.85)
$^{20}Ne + \alpha$
(19.53)
$^{23}Na + p$
(17.16)
$^{16}O + 2\alpha$
(14.80)
$^{23}Mg + n$
(12.32)
$^{22}Ne + 2p$
(8.36)
$^{12}C + 3\alpha$
(7.64)
$^{19}F + \alpha + p$
(6.69)
$^{22}Na + p + n$
(4.74)
$^{15}N + 2\alpha + p$
(2.68)
$^{19}Ne + \alpha + n$
(2.67)
$^{21}Ne + d + p$
(0.22)
$^{22}Mg + 2n$
(-0.84)

Figure 3

Pulse-height Spectrum of Protons Scattered from a Copper-backed ^{10}B Target

The beam current and integrated charge for these data were ~ 60 nA and 60 μC, respectively. The expected positions of the elastic scattering features arising from the various target constituents are indicated by arrows. The region of the ^{10}B scattering peak is shown on an expanded scale in the inset. The ^{10}B thickness of the target was determined with the aid of previously measured $\sigma_{el}/\sigma_{Ruth}$ value as described in page 9.

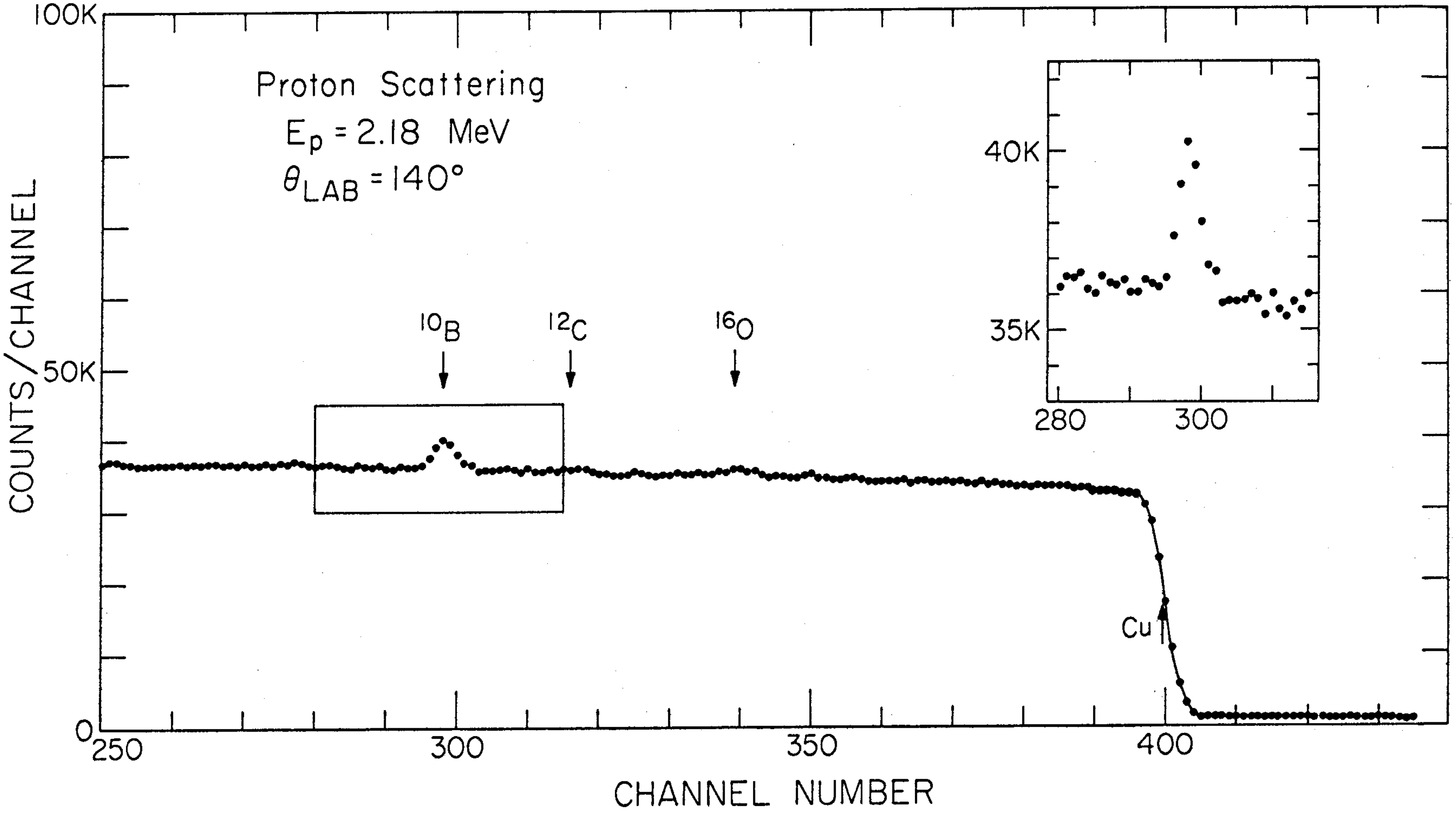
Proton Scattering
$E_p = 2.18$ MeV
$\theta_{LAB} = 140°$
^{10}B
^{12}C
^{16}O
Cu
COUNTS/CHANNEL
100K
50K
0
250
300
350
400
CHANNEL NUMBER
40K
35K
280
300

Figure 4

Photopeak Yields of 718 keV γ-rays from Coulomb Excitation of the ^{10}B Target by ^{14}N and ^{16}O Beams

The yields have been normalized to the calculated Coulomb excitation cross sections, which are given in section II.2.B of Part I, and shown by the solid curves. The error bars on the data points are derived from statistics alone. The ^{10}B target thickness determined by by this method is given in page 12.

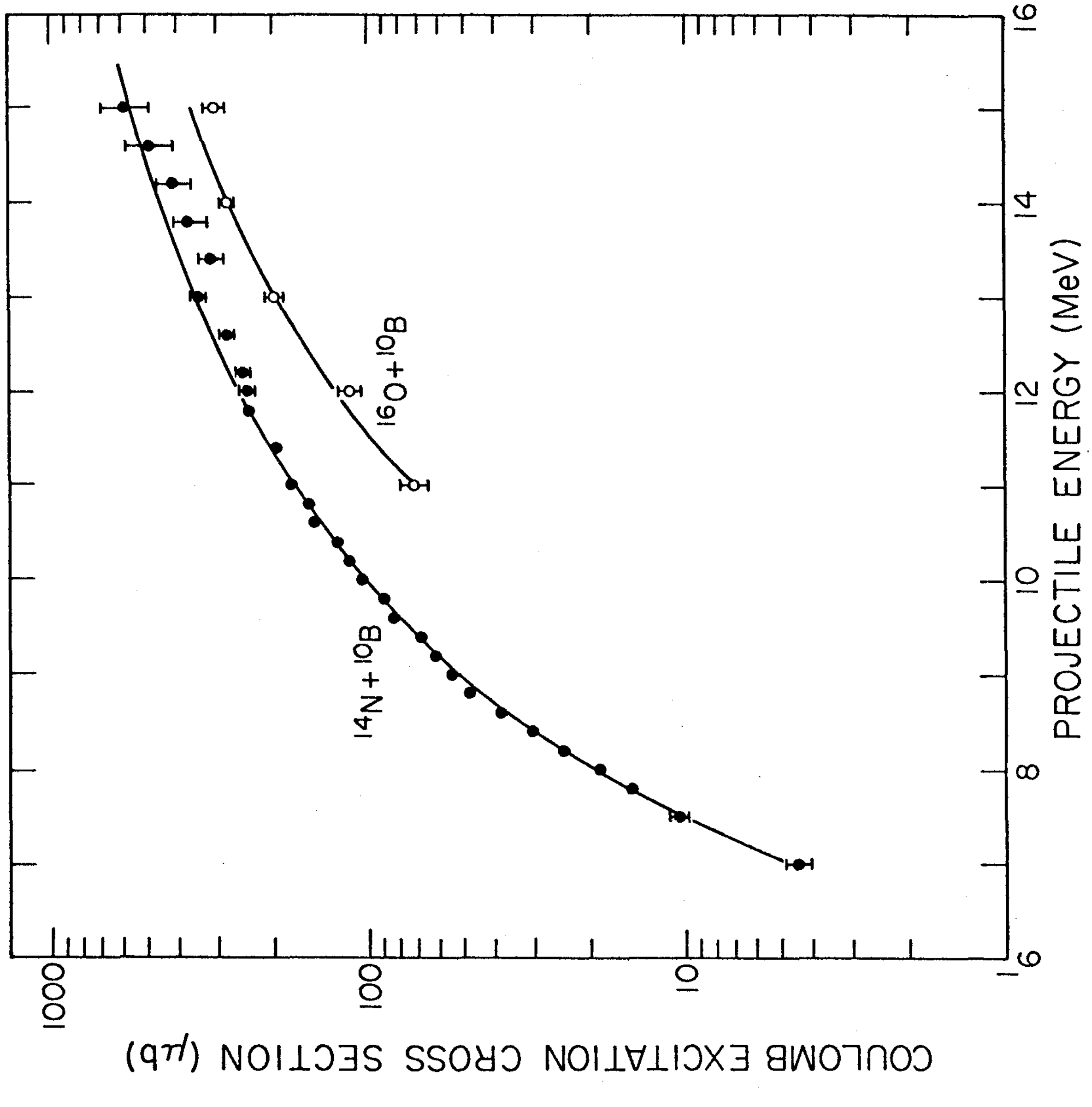
COULOMB EXCITATION CROSS SECTION (μb)
1000
100
10
PROJECTILE ENERGY (MeV)
6
8
10
12
14
16
$^{14}N+^{10}B$
$^{16}O+^{10}B$

Figure 5

Relative Hydrogen Concentration Profiles in a Copper-backed ^{10}B Target

The yields of γ-rays from the reaction $^{1}H(^{19}F,\alpha\gamma)^{16}O$ are plotted vs. ^{19}F beam energy. The energy-loss target thicknesses are indicated. The 16.44 MeV resonance natural width is 86 keV, which is 40 keV wider than the width of 6.40 MeV resonance. This accounts for the apparently greater target thickness measured by the higher energy resonance, in spite of the slightly larger dE/dx for fluorine ions at the lower resonance. For details, see page 16.

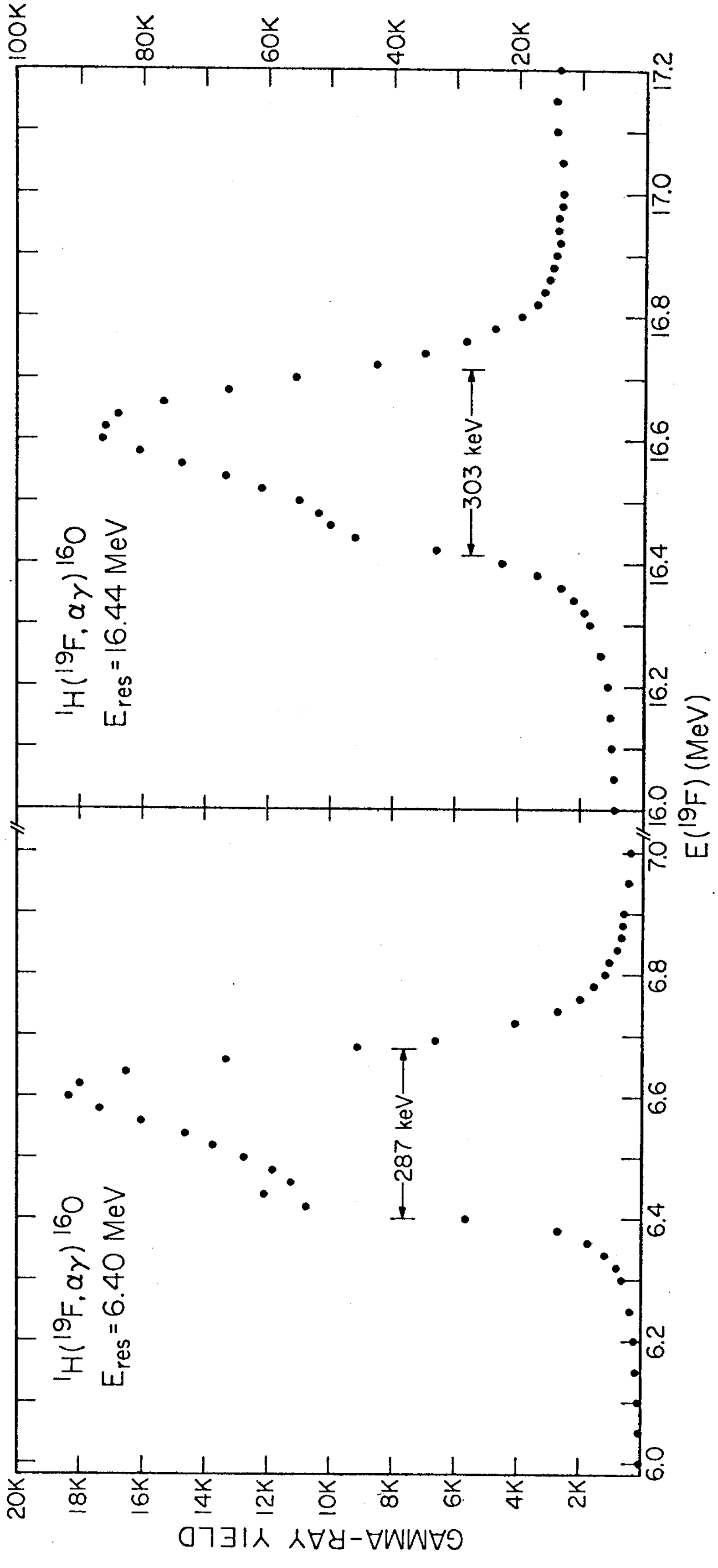
$^1H(^{19}F,\alpha\gamma)^{16}O$
$E_{res} = 6.40$ MeV
$^1H(^{19}F,\alpha\gamma)^{16}O$
$E_{res} = 16.44$ MeV
287 keV
303 keV
GAMMA-RAY YIELD
20K
18K
16K
14K
12K
10K
8K
6K
4K
2K
100K
80K
60K
40K
20K
6.0
6.2
6.4
6.6
6.8
7.0
16.0
16.2
16.4
16.6
16.8
17.0
17.2
$E(^{19}F)$ (MeV)

Figure 6

Gamma-ray Pulse-height Spectrum from the ^{14}N + ^{10}B Reactions

The abscissa for the lower energy portion of the spectrum is at the top of the figure. The numbered full-energy peaks are identified in table 1. The full-energy and excape peaks from the 6.131 MeV state of ^{16}O nucleus are not shown here. For additional details, see table 1 and pages 14 and 18.

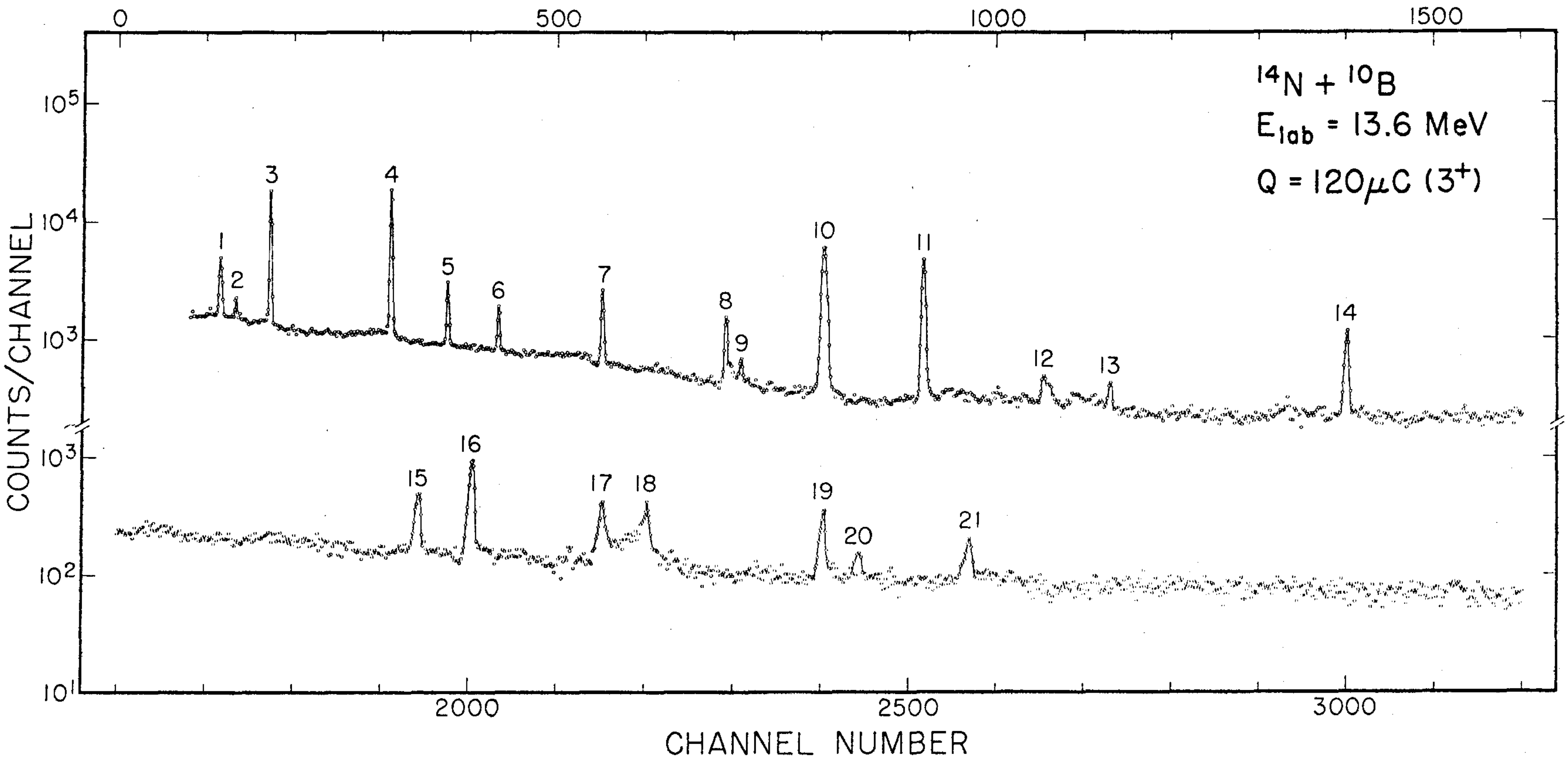

$^{14}N + ^{10}B$
E_{lab} = 13.6 MeV
Q = 120μC (3^+)
0
500
1000
1500
10^5
10^4
10^3
10^3
10^2
10^1
COUNTS/CHANNEL
1
2
3
4
5
6
7
8
9
10
11
12
13
14
15
16
17
18
19
20
21
2000
2500
3000
CHANNEL NUMBER

Figure 7

The Decay Scheme of ^{133}Ba

The gamma-rays of energy 276 keV, 303 keV, 356 keV, and 384 keV were used for calibrating the photopeak efficiency of the Ge(Li) detector employed during the present measurements. For details, see page 23.

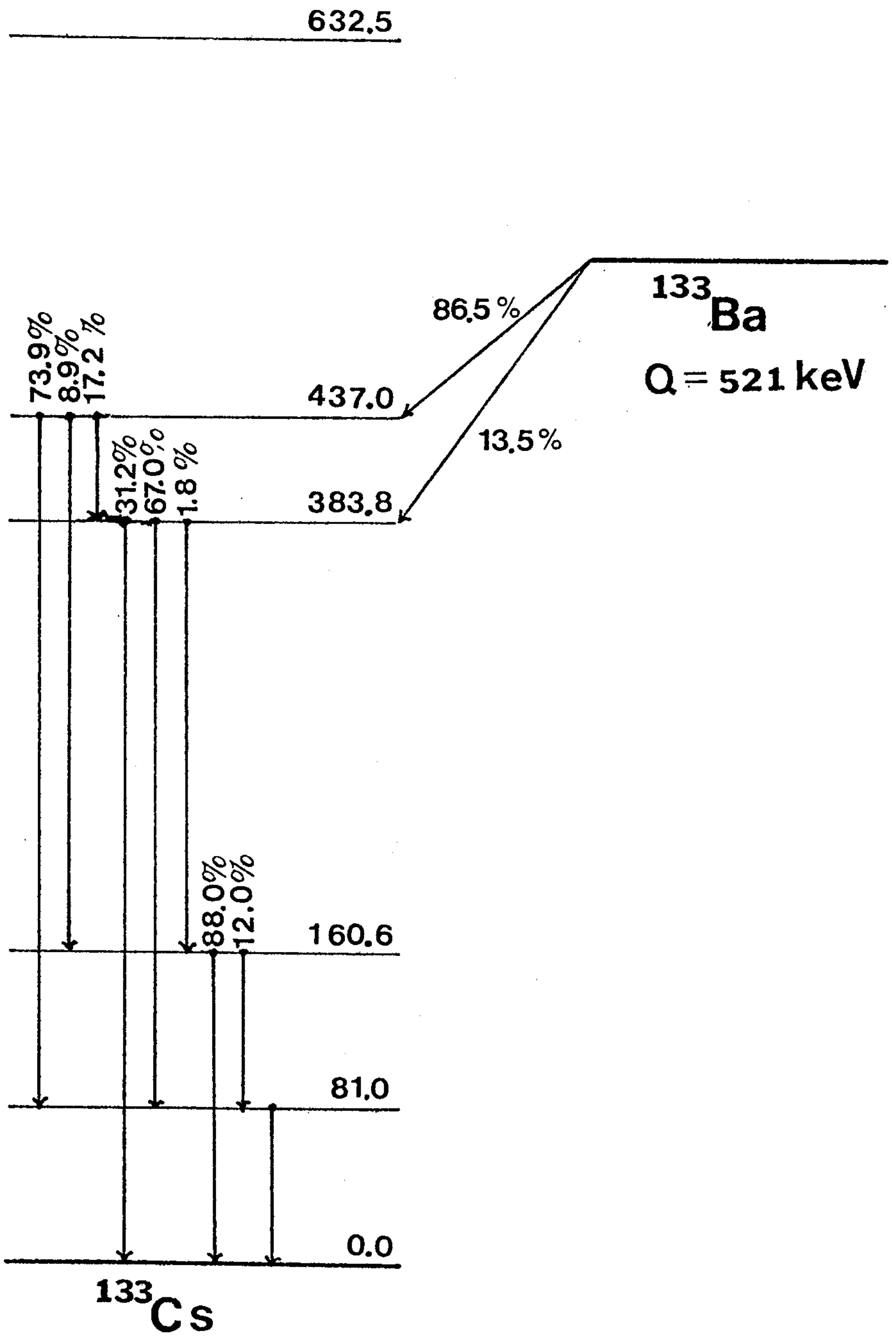
632.5
133Ba
Q = 521 keV
86.5 %
13.5 %
73.9%
8.9%
17.2 %
437.0
31.2%
67.0%
1.8 %
383.8
88.0%
12.0%
160.6
81.0
0.0
133Cs

Figure 8

The Photopeak Efficiency of the Ge(Li) Detector Used in the Present Measurements

For curve 1, the target was 1.4 cm away from the Germanium crystal, with a 3 mm lead sheet inserted between them to attenuate low energy γ-rays. The curve (1) was determined by the measured data points, and with the aid of γ-ray attenuation calculations based on the assumption that the efficiency curve without the lead absorber would be parallel to curve 2.

For curve 2, the distance between the target and the Germanium crystal was about 3 cm, without any lead sheet in between.

For more details, see page 24.

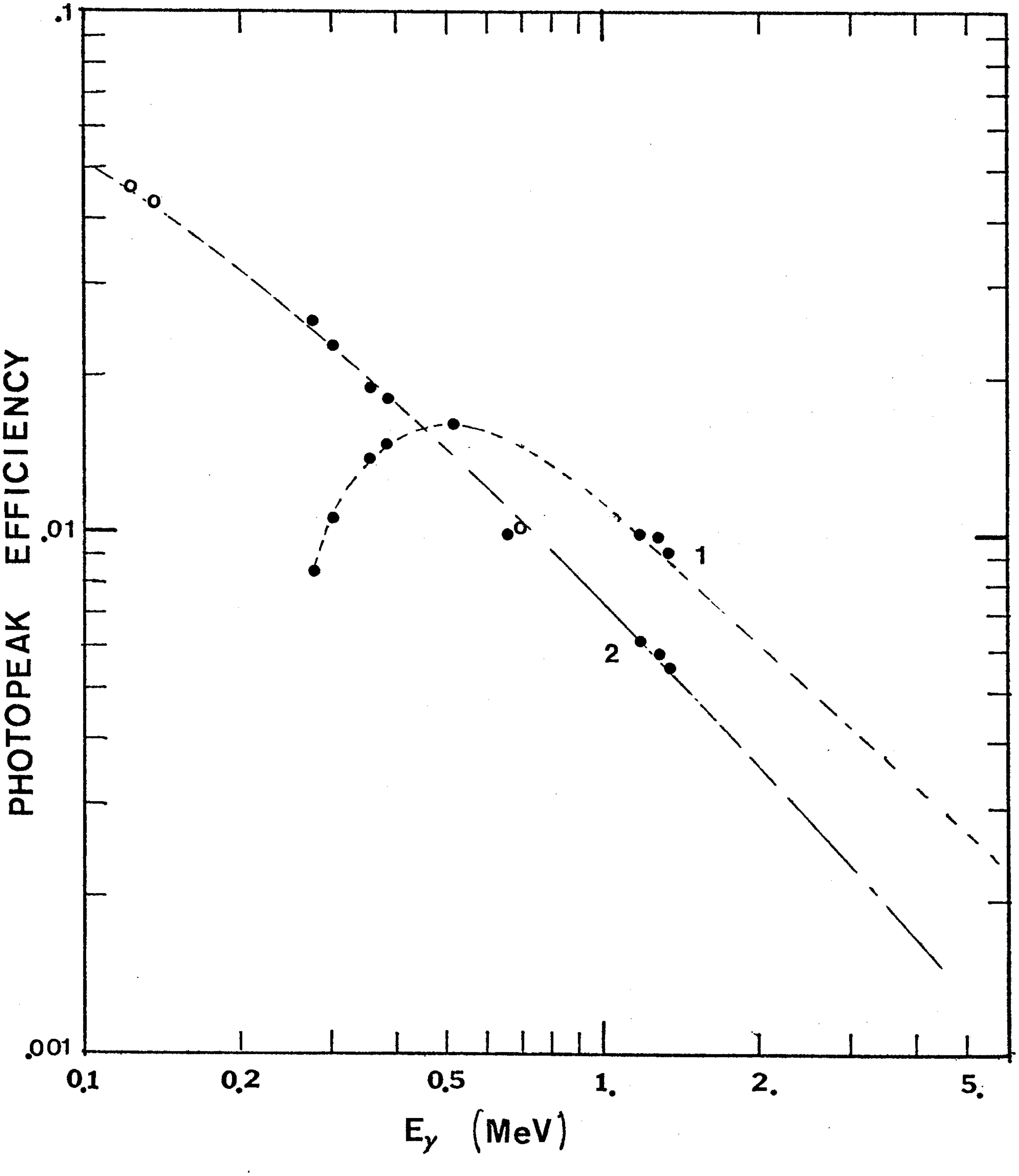

.1
.01
.001
0.1
0.2
0.5
1.
2.
5.
PHOTOPEAK EFFICIENCY
E_γ (MeV)
1
2

Figure 9

The Excitation Function of the ^{27}Al(p,γ)^{28}Si near the E_p = 992 keV Resonance

The resonance γ-rays were used to determined the relative detection efficiencies for γ-rays with energies between 1.5 MeV and 10 MeV. For details, see page 25.

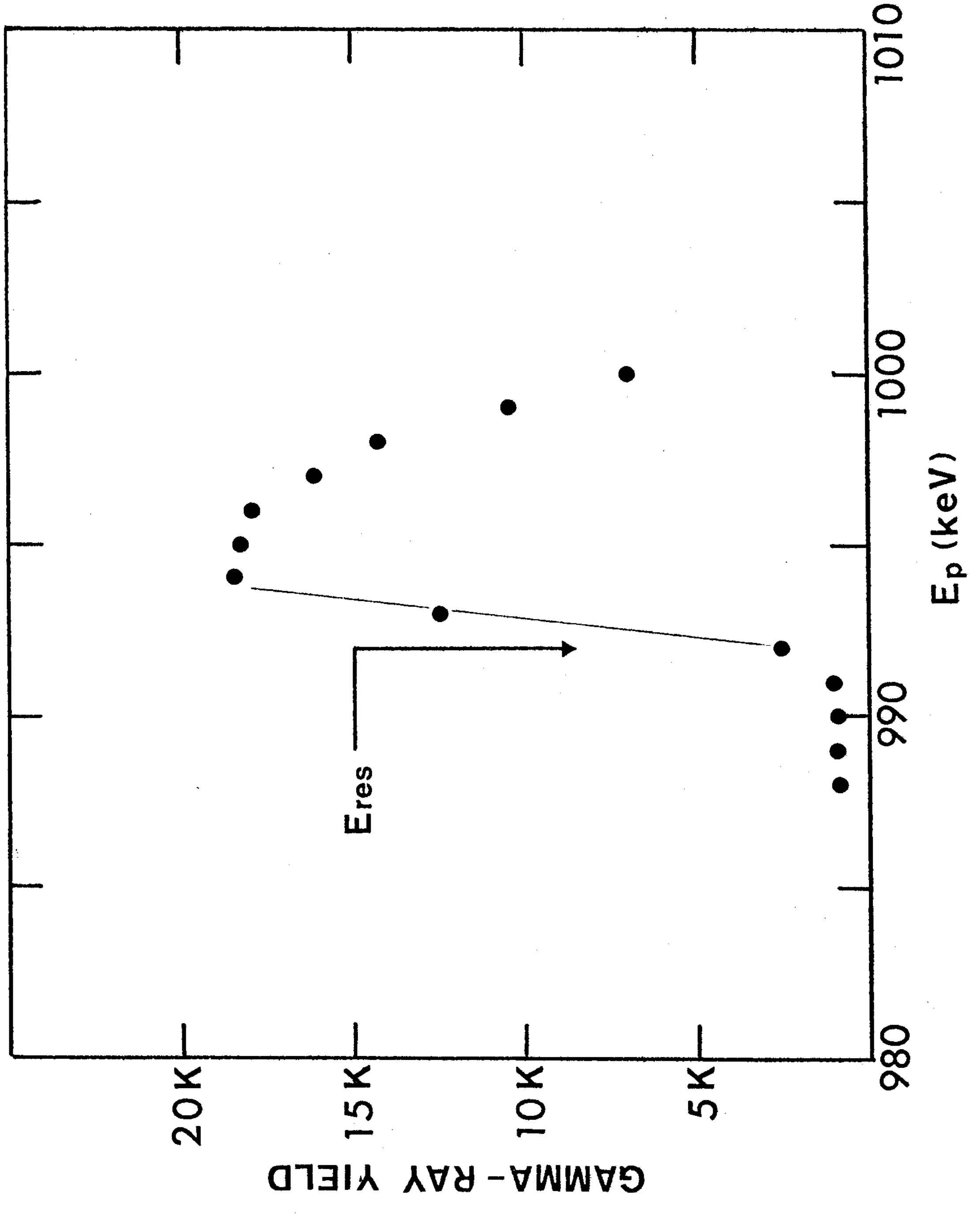
GAMMA-RAY YIELD
20K
15K
10K
5K
980
990
1000
1010
E_p (keV)
E_res

Figure 10

Relative Photopeak Efficiency Curve for the Ge(Li) Detector Used in the Present Experiment

The photopeak efficiency calibration curves shown in fig. 8 were extended to the energy region $E_\gamma \approx 10$ MeV by using the E_p=992keV resonance of $^{27}Al(p,\gamma)^{28}Si$ as described in section II.3.B. The curve shown here is for geometry 3 defined in the main text, and is the continuation of curve 2 in fig.8. For details, see page 25.

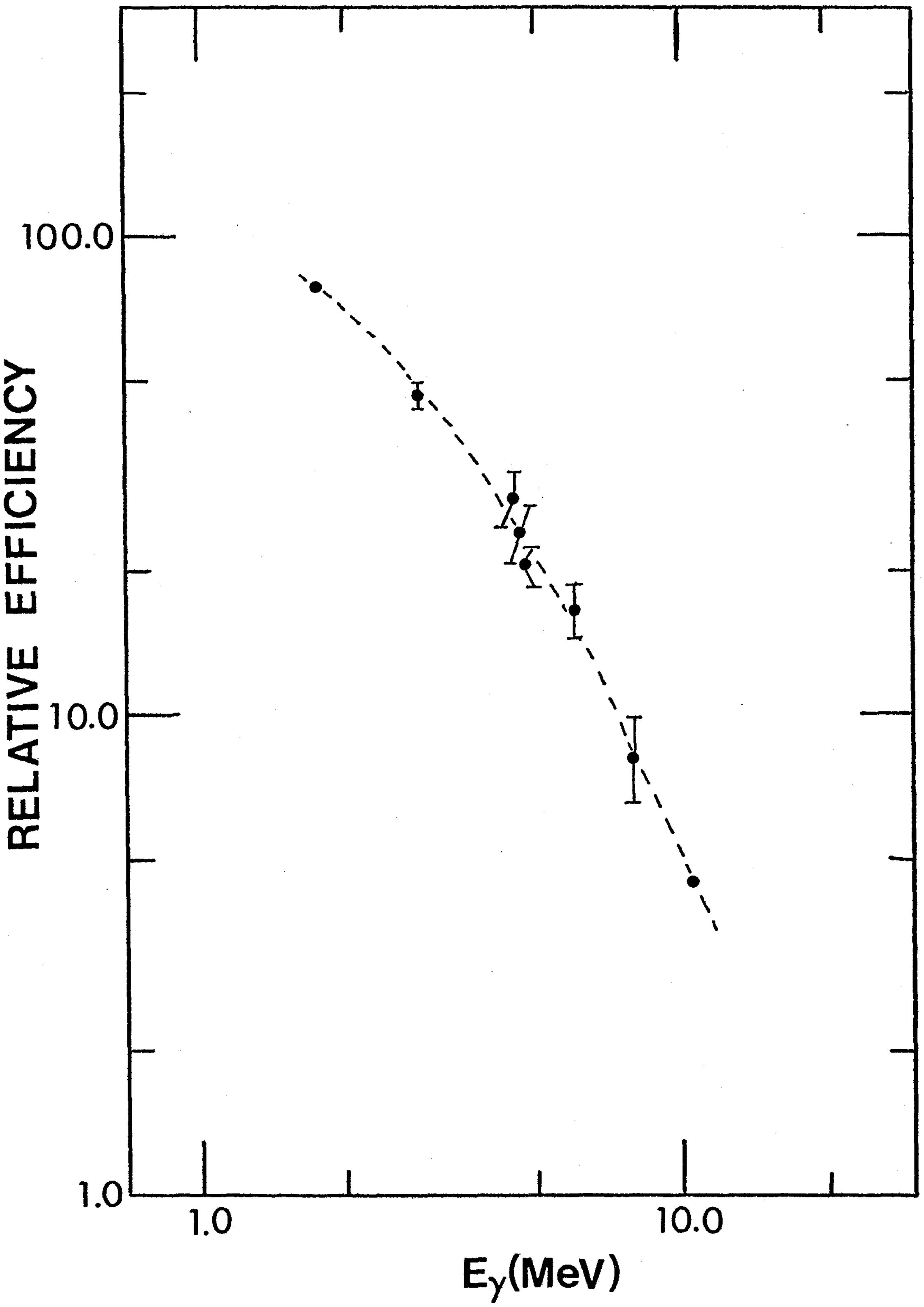
100.0
10.0
1.0
1.0
10.0
RELATIVE EFFICIENCY
E_γ(MeV)

Figure 11

Cross Sections for Production of Single-Particle Evaporation Residues from ^{14}N + ^{10}B Fusion Reaction

The error bars at low energies arise from counting statistics alone. For details, see page 33.

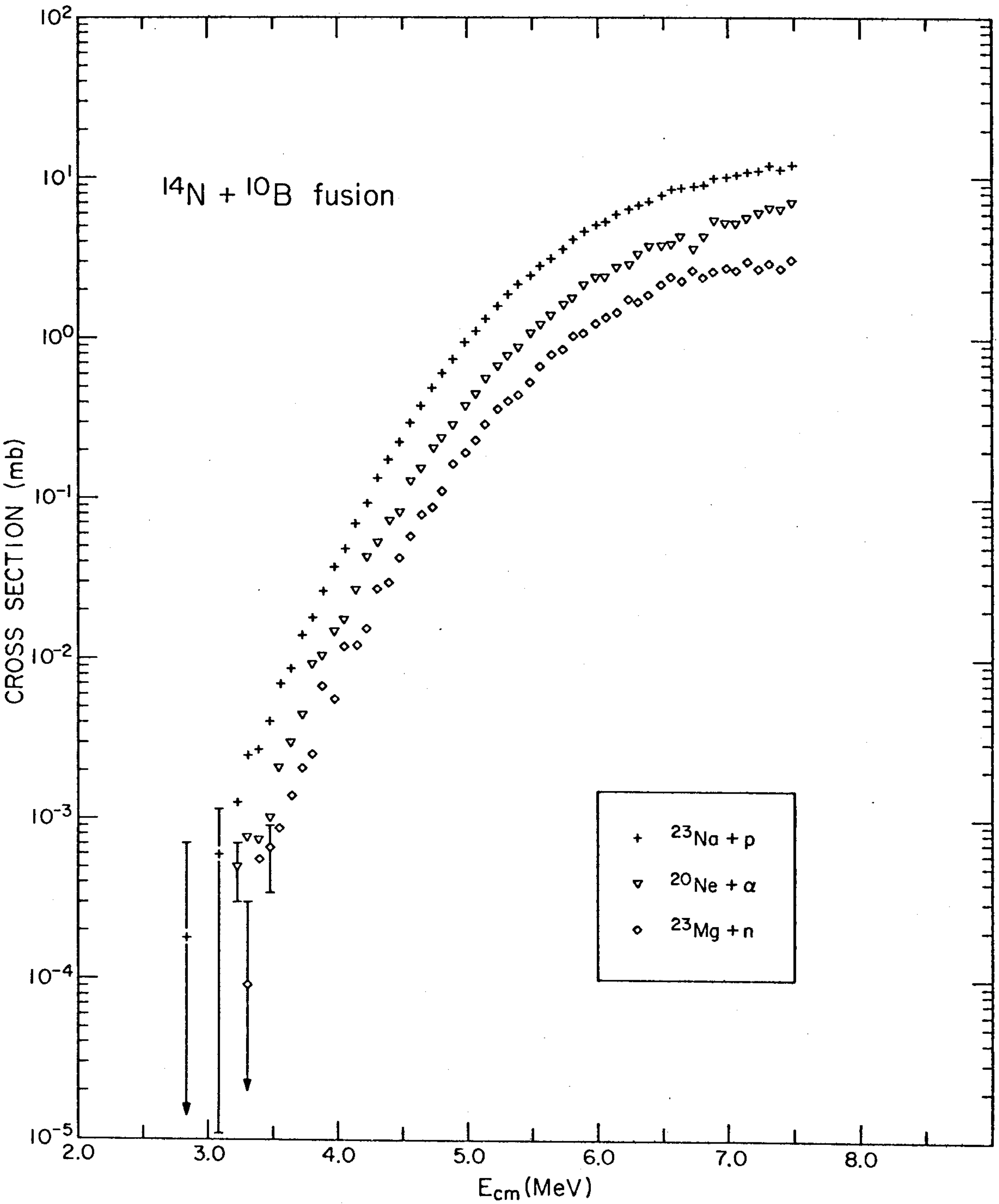
$^{14}N + ^{10}B$ fusion
CROSS SECTION (mb)
E_{cm} (MeV)
10^{2}
10^{1}
10^{0}
10^{-1}
10^{-2}
10^{-3}
10^{-4}
10^{-5}
2.0
3.0
4.0
5.0
6.0
7.0
8.0
+ $^{23}Na + p$
▽ $^{20}Ne + \alpha$
◇ $^{23}Mg + n$

Figure 12

Cross Sections for Production of Two-particle Evaporation Residues from the ^{14}N + ^{10}B Fusion Reactions

For clarity, the data for ^{16}O, ^{19}F and ^{21}Ne have been displaced vertically by the factors indicated. The error bars at low energies derive from counting statistics alone. For details, see pages 35 and 38.

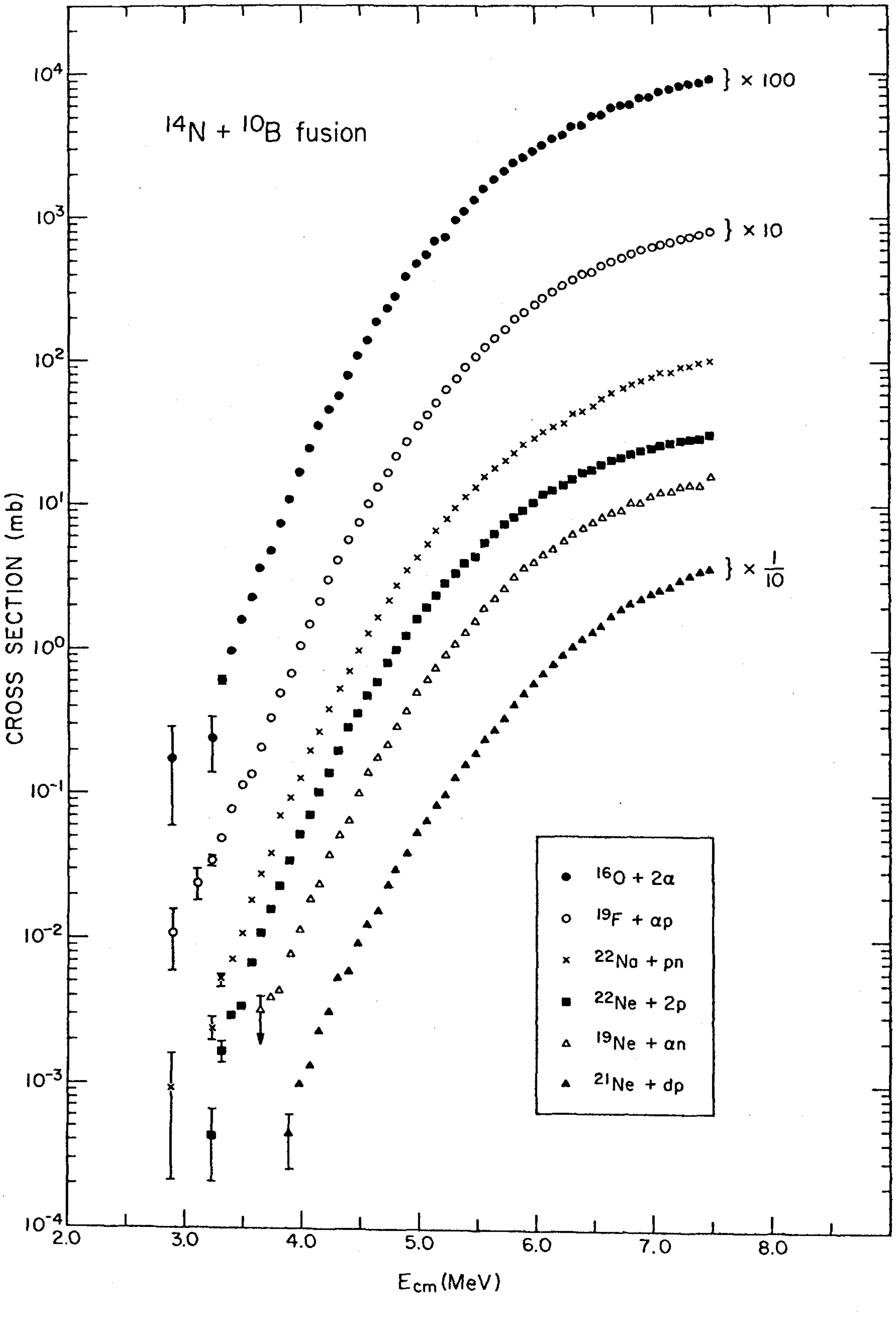
$^{14}N + ^{10}B$ fusion
} × 100
} × 10
} × $\frac{1}{10}$
CROSS SECTION (mb)
10^4
10^3
10^2
10^1
10^0
10^{-1}
10^{-2}
10^{-3}
10^{-4}
2.0
3.0
4.0
5.0
6.0
7.0
8.0
E_{cm} (MeV)
● $^{16}O + 2\alpha$
○ $^{19}F + \alpha p$
× $^{22}Na + pn$
■ $^{22}Ne + 2p$
△ $^{19}Ne + \alpha n$
▲ $^{21}Ne + dp$

Figure 13

Calculated Bound State Fractions for ^{16}O and ^{19}F

The bound state fractions for ^{19}Ne, ^{22}Ne and ^{22}Na differ from unity by at most a few percent and are not shown here. Calculations of bound state fractions are discussed on page 37.

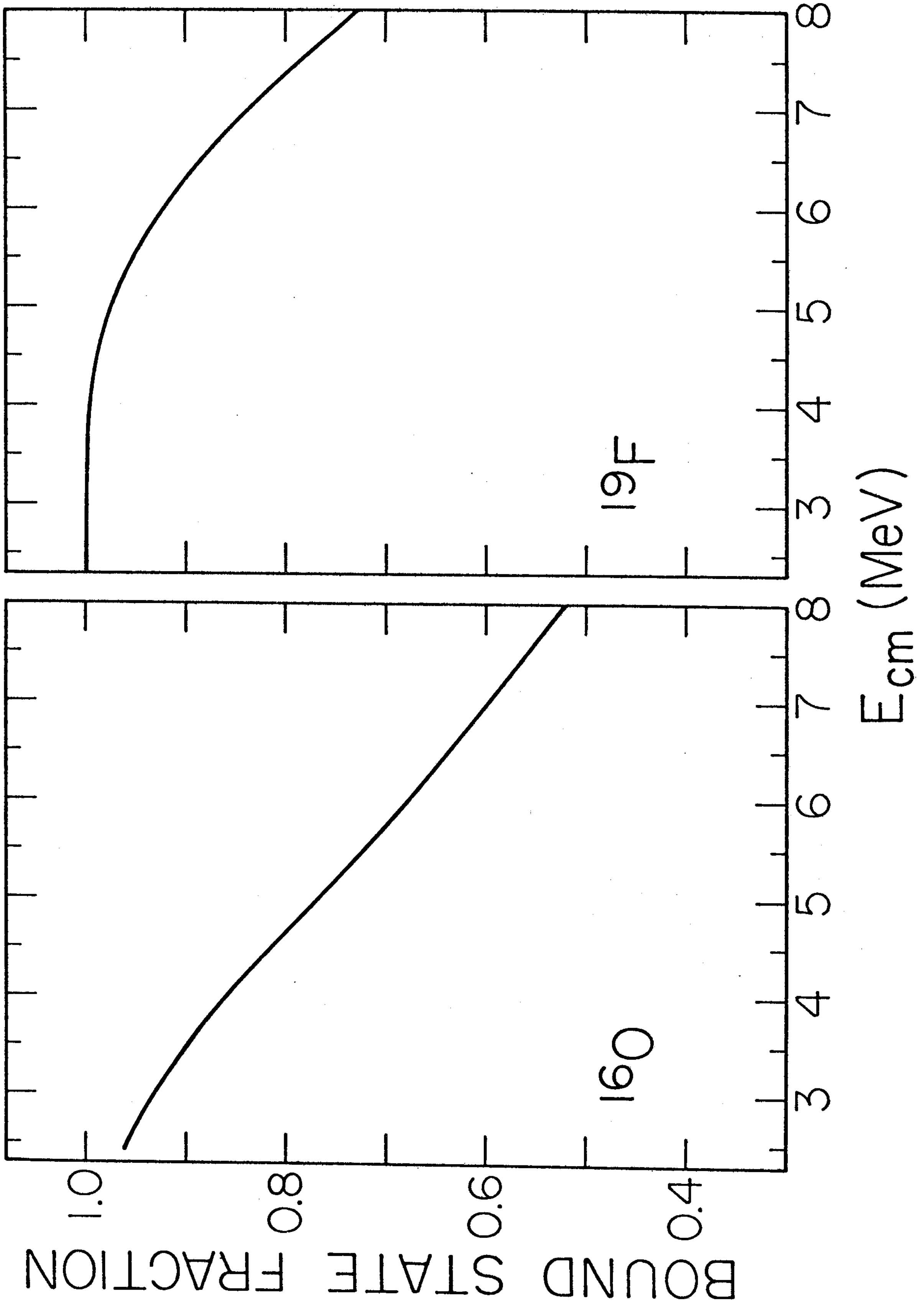
BOUND STATE FRACTION
1.0
0.8
0.6
0.4
^{16}O
3
4
5
6
7
8
^{19}F
3
4
5
6
7
8
E_{cm} (MeV)

Figure 14

$^{14}N + ^{10}B$ Fusion Cross Sections

The cross sections measured in the present work are shown as open circles, while the results of measurements by High and Čujec (Hi 77a) are shown as filled circles. The two sets of data are compared in section III.5 (pages 38, 39).

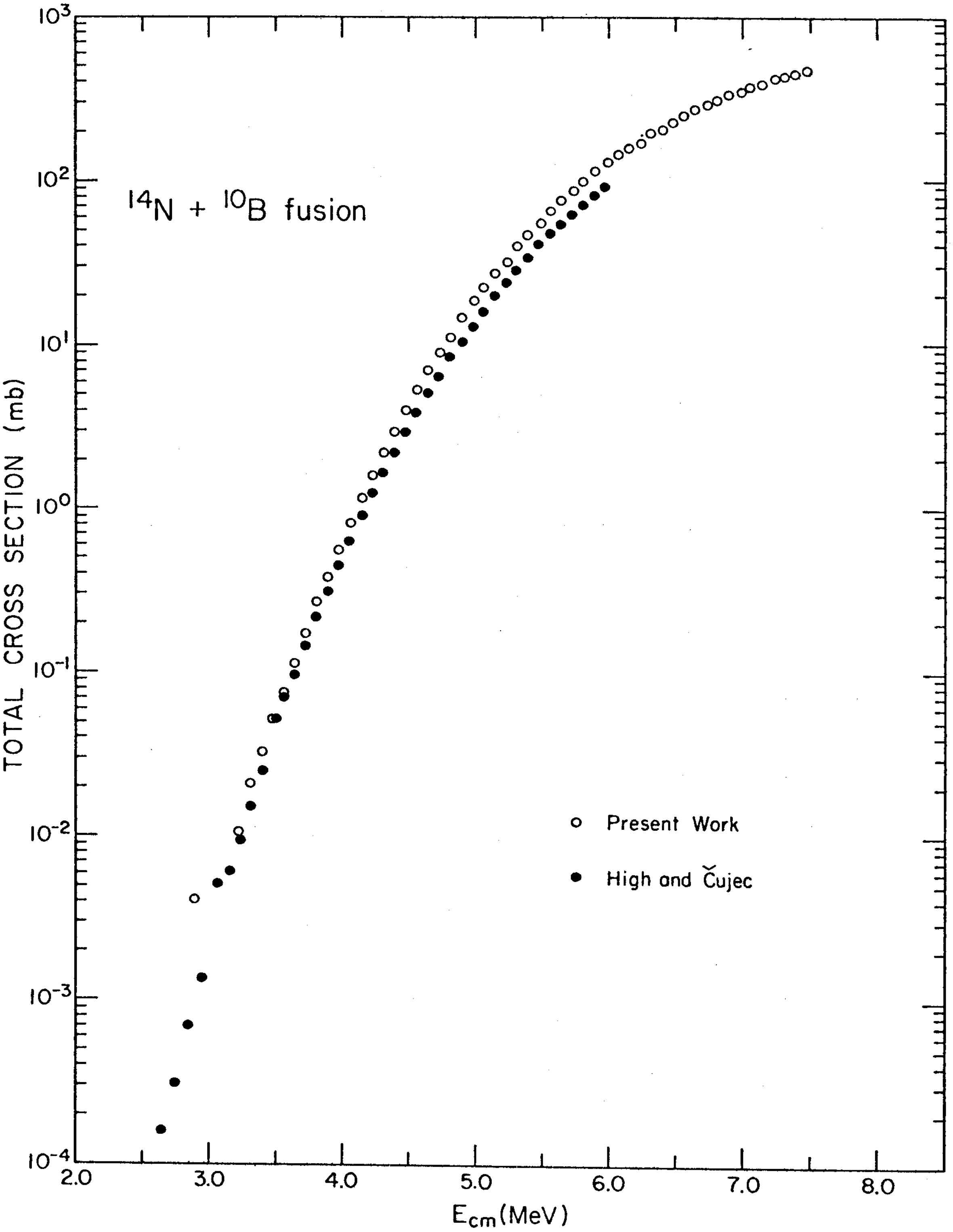
$^{14}N + ^{10}B$ fusion
TOTAL CROSS SECTION (mb)
10^3
10^2
10^1
10^0
10^{-1}
10^{-2}
10^{-3}
10^{-4}
2.0
3.0
4.0
5.0
6.0
7.0
8.0
E_{cm}(MeV)
○ Present Work
● High and Čujec

Figure 15

Pulse-height Spectrum of Proton Scattered from a Thin Carbon-backed ^{10}B Target

This spectrum was accumulated at $\theta_{lab} = 120°$, with an incident proton beam at 2.2 MeV laboratory energy. The beam current and integrated charge were $\sim$15 nA and 24 μc respectively. (page 44)

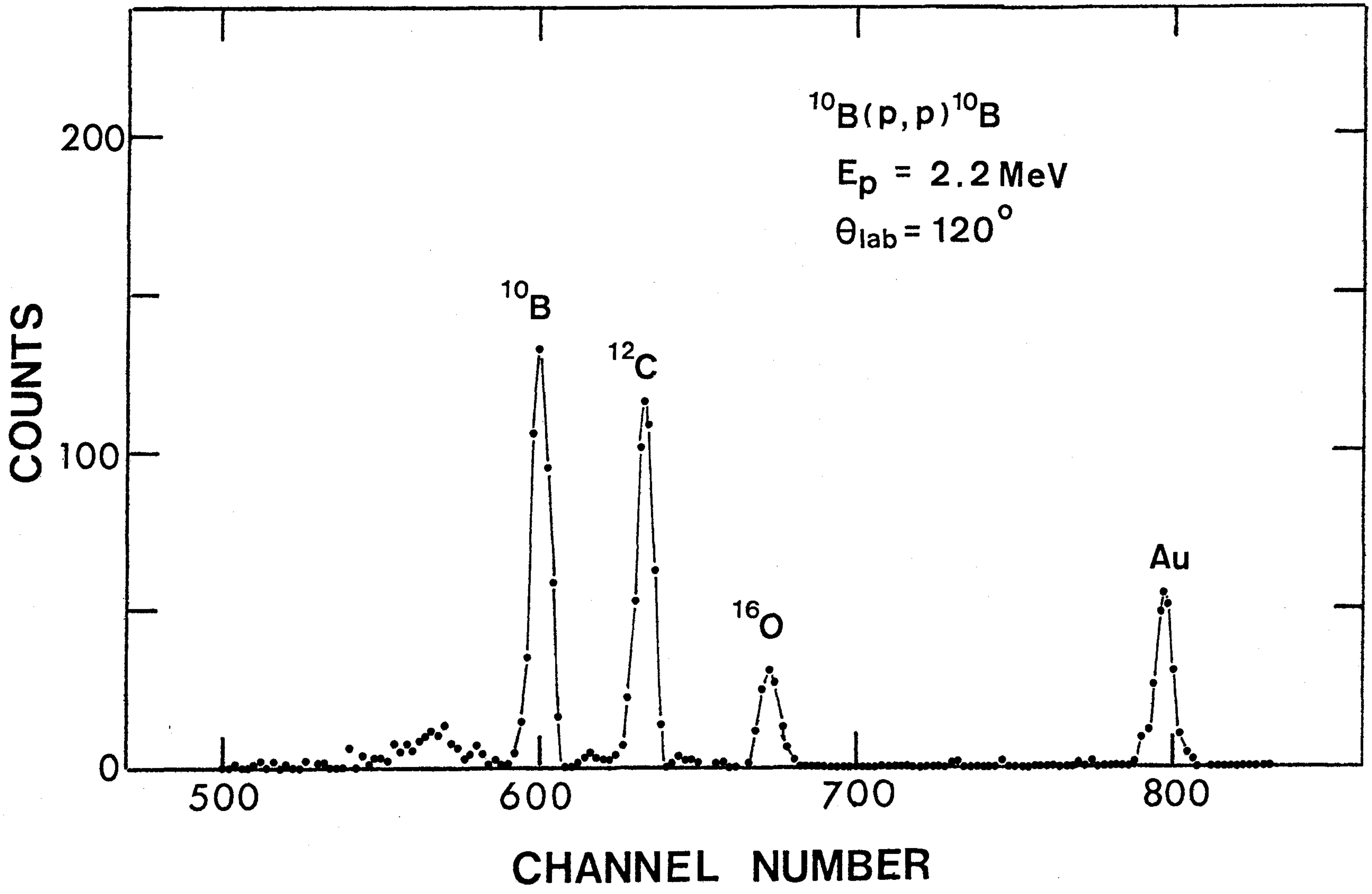
$^{10}B(p,p)^{10}B$
E_p = 2.2 MeV
θ_{lab} = 120°
^{10}B
^{12}C
^{16}O
Au
COUNTS
0
100
200
CHANNEL NUMBER
500
600
700
800

Figure 16

Pulse-height Spectrum of Scattered Particles Detected When a ^{14}N Beam is Incident on a Carbon-film-backed ^{10}B Target

Peaks arising from scattered ^{14}N ions are labelled by the target nuclei. The recoils of the target constituents are also indicated. For more details, see page 46.

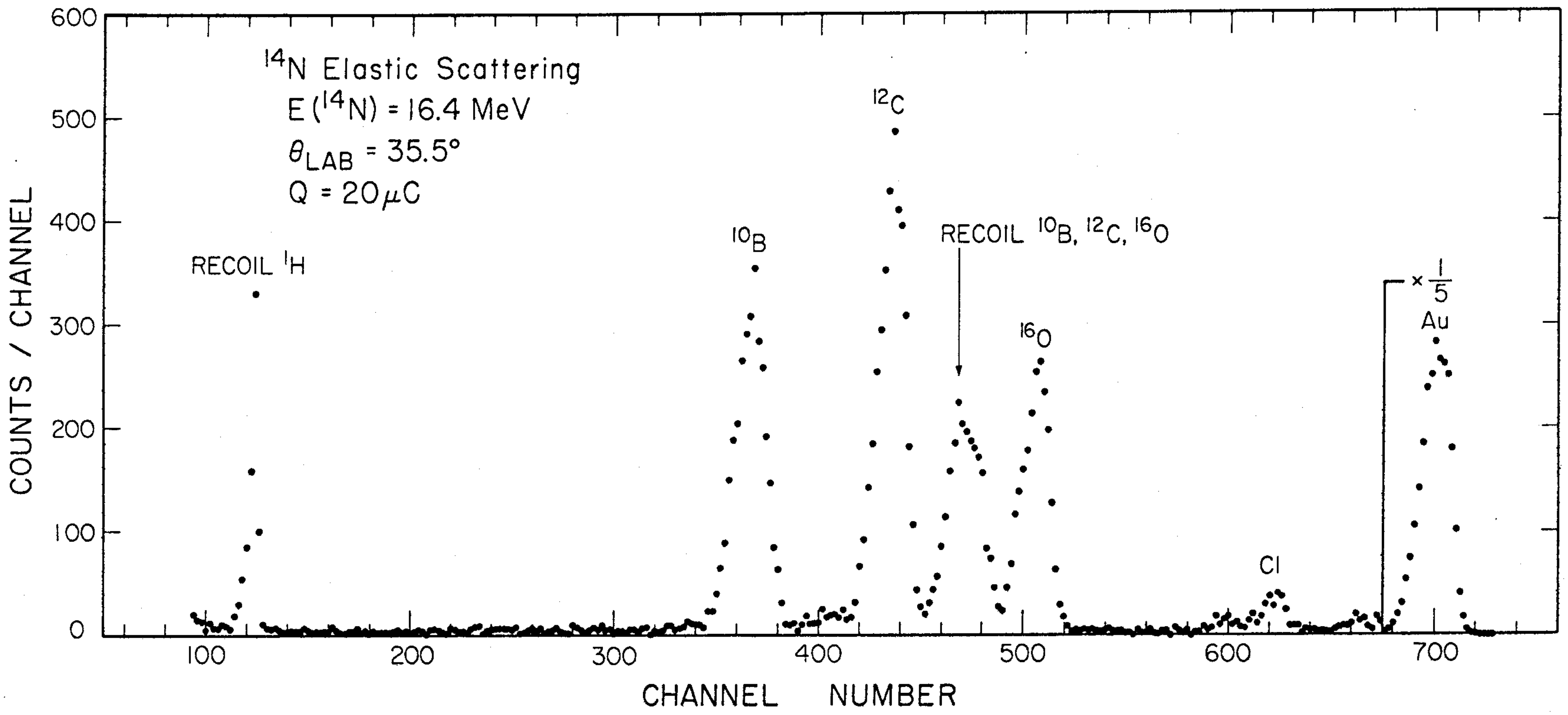
^{14}N Elastic Scattering
$E(^{14}N) = 16.4$ MeV
$\theta_{LAB} = 35.5°$
$Q = 20 \mu C$
RECOIL ^1H
^{10}B
^{12}C
RECOIL ^{10}B, ^{12}C, ^{16}O
^{16}O
Cl
$\times \frac{1}{5}$
Au
COUNTS / CHANNEL
CHANNEL NUMBER
0
100
200
300
400
500
600
700

Figure 17

Pulse-height Spectrum of Scattered Particles Detected When a ^{14}N Beam is Incident on a Self-supporting ^{10}B Target

Peaks arising from scattered ^{14}N ions are labelled by the target nuclei. The recoils of target constituents are also indicated. For details, see page 46.

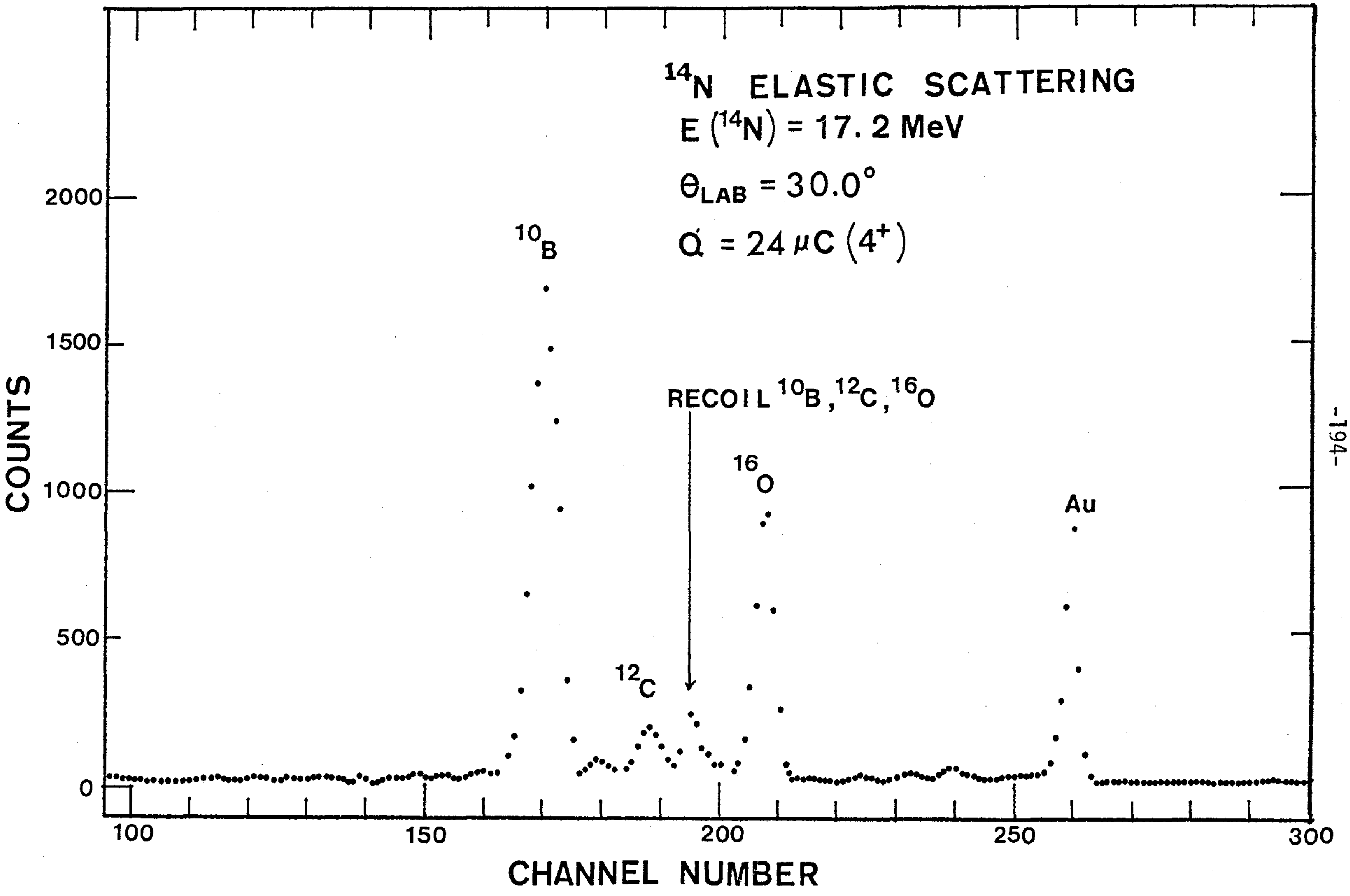

^{14}N ELASTIC SCATTERING
$E\,(^{14}N) = 17.2$ MeV
$\theta_{LAB} = 30.0°$
$Q = 24\,\mu C\,(4^+)$
^{10}B
^{12}C
RECOIL ^{10}B, ^{12}C, ^{16}O
^{16}O
Au
COUNTS
0
500
1000
1500
2000
100
150
200
250
300
CHANNEL NUMBER

Figure 18

$^{14}N + ^{10}B$ Elastic Scattering Differential Cross Section Presented as the Ratio to the Rutherford Scattering Cross Section

The data have been normalized to Rutherford scattering at low energies as described in section IV.3. The scale for the $\theta_{cm} = 74.4°$ scattering is at the right. The solid curves shown are the results of IWBC calculations with a = 0.50 fm and $R_b = 8.08$ fm ($r_o = 1.24$ fm). For the scattering data, see page 47 . For further details of IWBC calculations, see page 54.

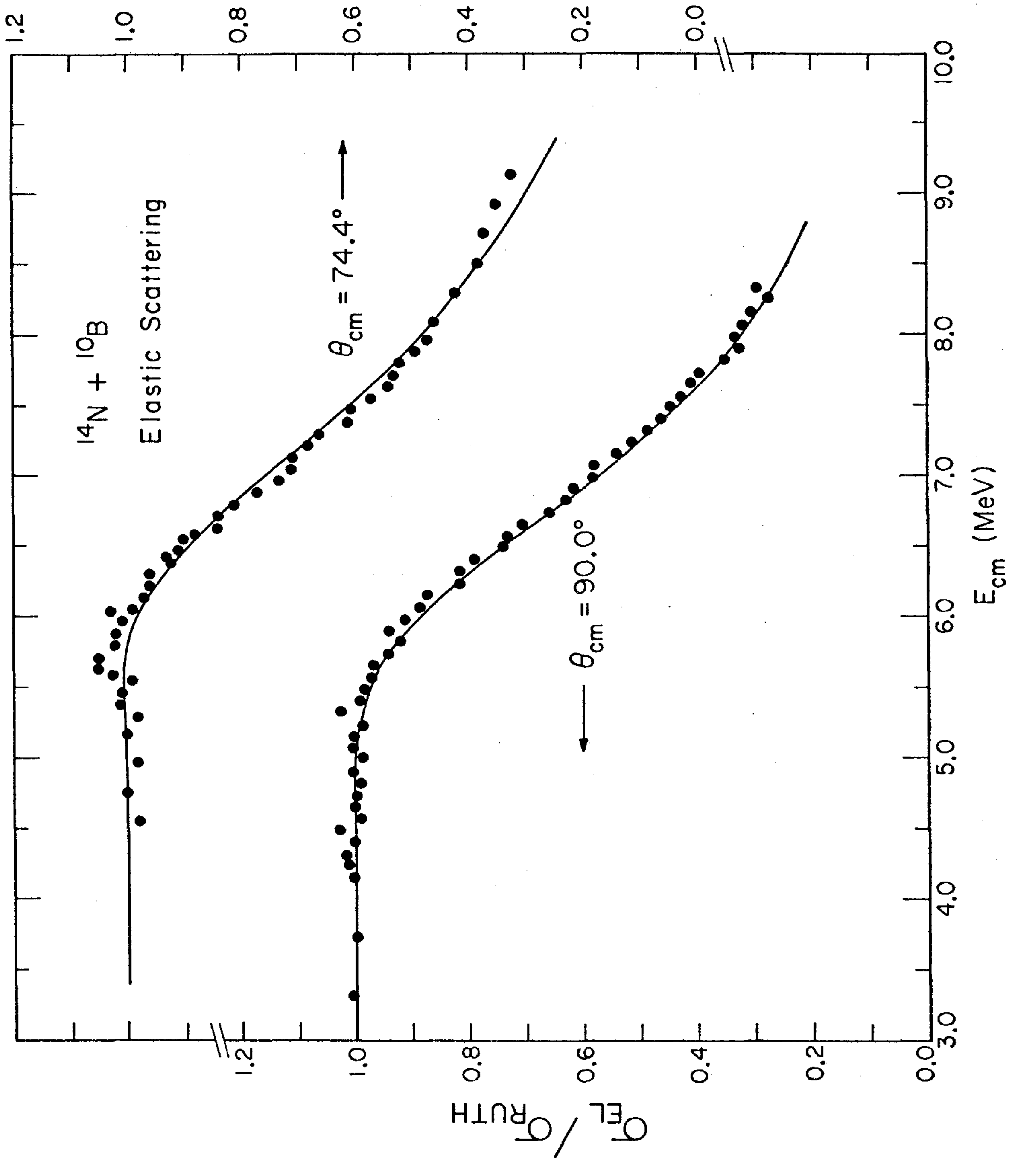

$^{14}N + ^{10}B$
Elastic Scattering
$\theta_{cm} = 74.4°$
$\theta_{cm} = 90.0°$
E_{cm} (MeV)
$\sigma_{EL} / \sigma_{RUTH}$
3.0
4.0
5.0
6.0
7.0
8.0
9.0
10.0
0.0
0.2
0.4
0.6
0.8
1.0
1.2

Figure 19

IWBC Calculations for ^{14}N + ^{10}B Elastic Scattering

Measurements at $\theta_{cm} = 90.0°$ are shown as filled circles. The solid curves are best IWBC fits, with r_b = 1.77 fm (or R_b= 8.08 fm) and a = 0.50 fm. The dashed curves are IWBC calculations with different parameter sets: (1) Top, r_b = 1.70 fm, a = 0.50 fm (2) Bottom: r_b = 1.77 fm, a = 0.60 fm. For more details, see page 55.

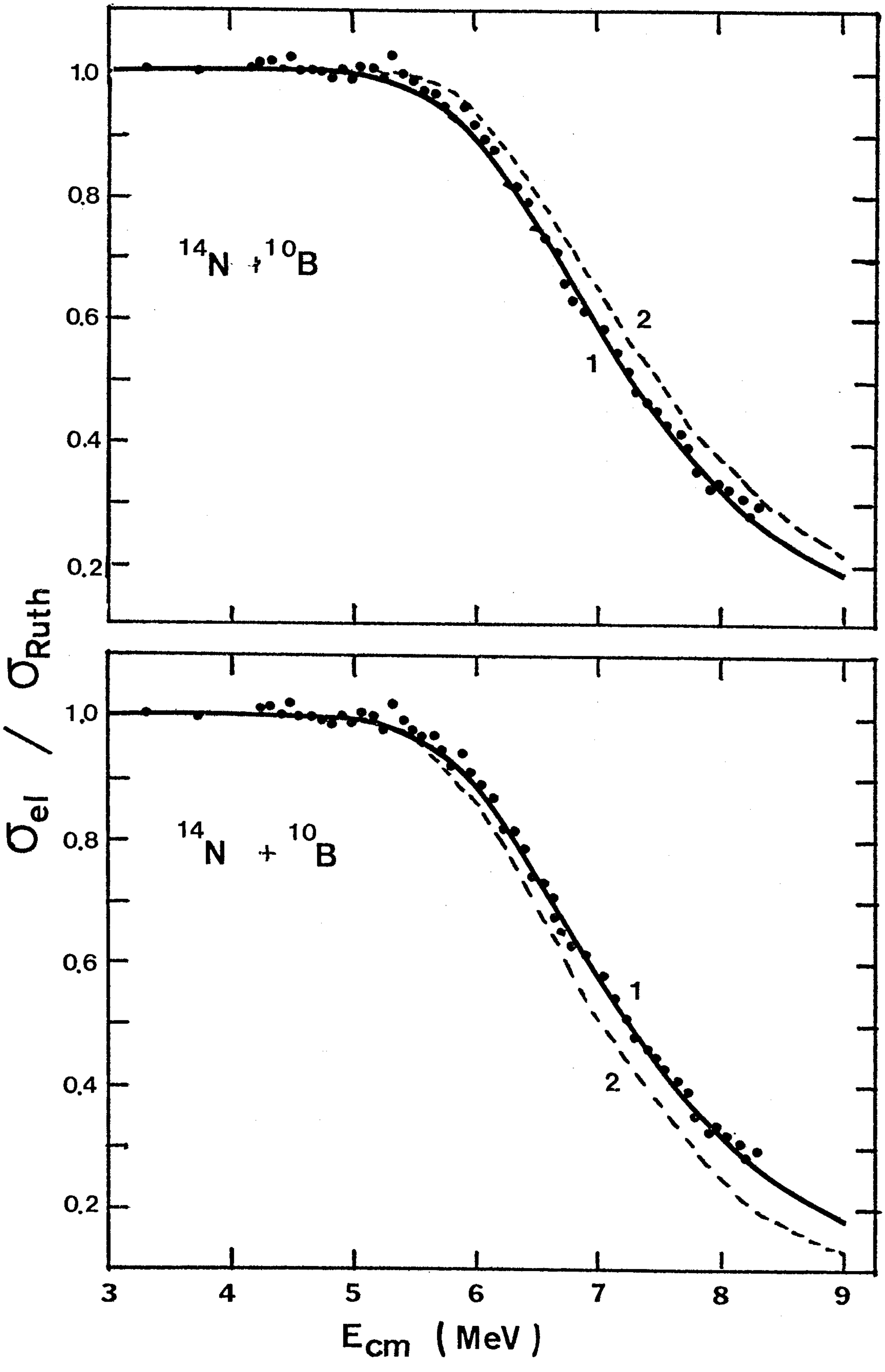

1.0
0.8
0.6
0.4
0.2
$^{14}N + ^{10}B$
1
2
1.0
0.8
0.6
0.4
0.2
$^{14}N + ^{10}B$
1
2
3
4
5
6
7
8
9
$\sigma_{el} / \sigma_{Ruth}$
E_{cm} (MeV)

Figure 20

S-factor for the $^{14}N + ^{10}B$ Fusion Reaction

The filled circles are from the present work. The error bars at low energies derive from counting statistics alone. The solid curve is an IWBC calculation with the parameter set, R_b=8.08 fm and a = 0.50 fm, which gives the best fit for the elastic scattering data in fig. 18. For comparison purpose, the $^{12}C + ^{12}C$ fusion S-factor of Patterson et al (Pa 69) are shown as open circles, displaced upward by a factor of 10 for display clarity. For details, see pages 55 and 59.

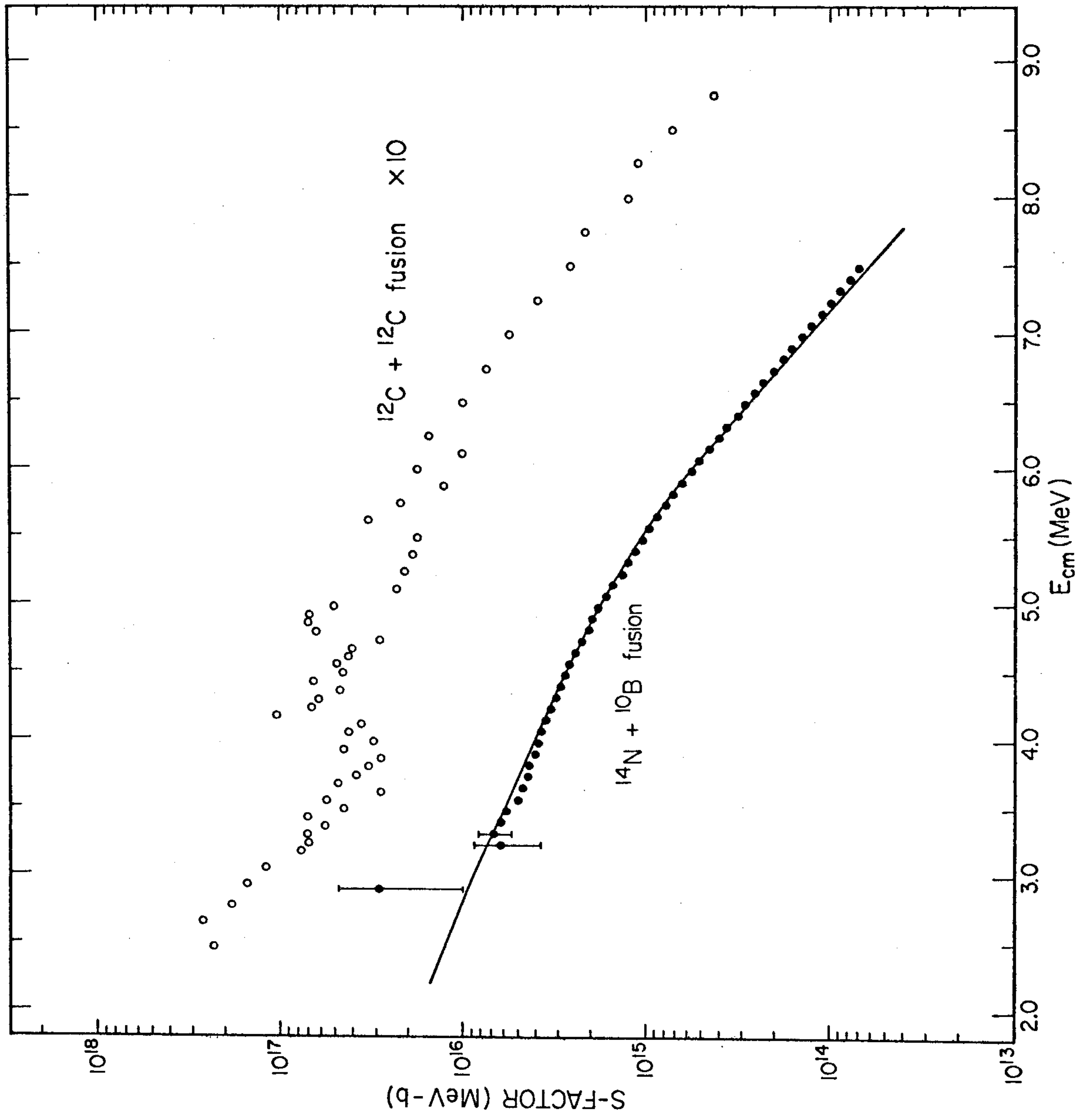
S-FACTOR (MeV-b)
10^18
10^17
10^16
10^15
10^14
10^13
2.0
3.0
4.0
5.0
6.0
7.0
8.0
9.0
E_cm (MeV)
12C + 12C fusion ×10
14N + 10B fusion

Figure 21

IWBC Calculations of ^{14}N + ^{10}B S-factors

The filled circles are from the present measurement. The calculated fusion S-factors from an IWBC model with the parameter set of fig. 18 and fig. 20 are shown as solid curves. For comparison, the IWBC calculations were also carried out with parameter sets given in fig. 19, and the results are displayed as dashed curves. Parameter sets used for these calculations are: (1) Top, r_b = 1.70 fm, a = 0.50 fm. (2) Bottom: r_b = 1.77 fm, a = 0.60 fm. for more details, see page 57.

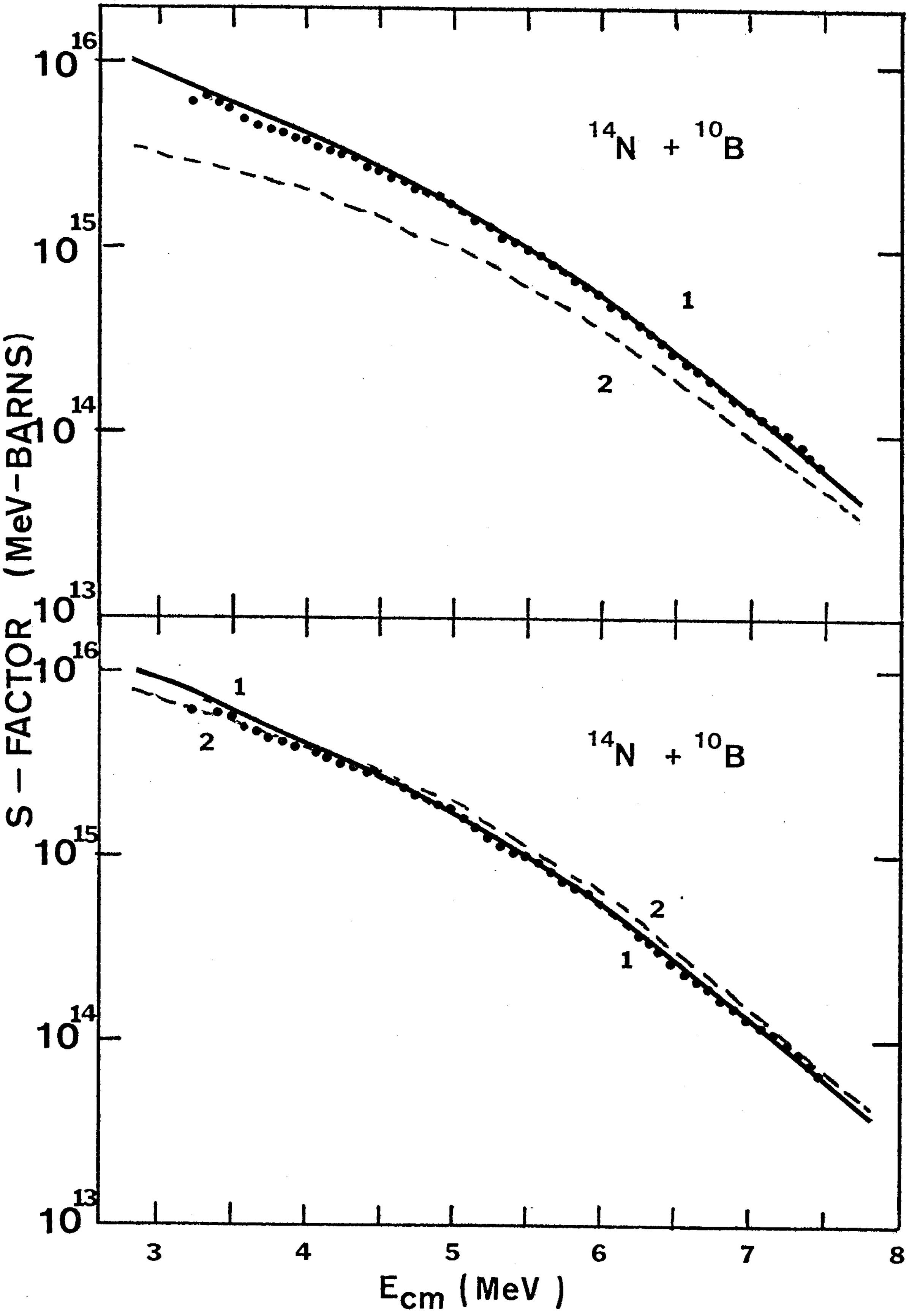
$^{14}N + ^{10}B$
1
2
$^{14}N + ^{10}B$
1
2
2
1
10^{16}
10^{15}
10^{14}
10^{13}
10^{16}
10^{15}
10^{14}
10^{13}
S – FACTOR (MeV–BARNS)
3
4
5
6
7
8
E_{cm} (MeV)

Figure 22

The Q-value Scheme for the Open Channels Initiated by the Reaction of ^{16}O with ^{16}O

The reaction cross section for $^{16}O + {}^{16}O$ was measured from a center of mass energy of 7.0 MeV to 12.0 MeV. The γ-ray transitions used for the deduction of cross sections are indicated by arrows. For more details, see pages 67 and 98.

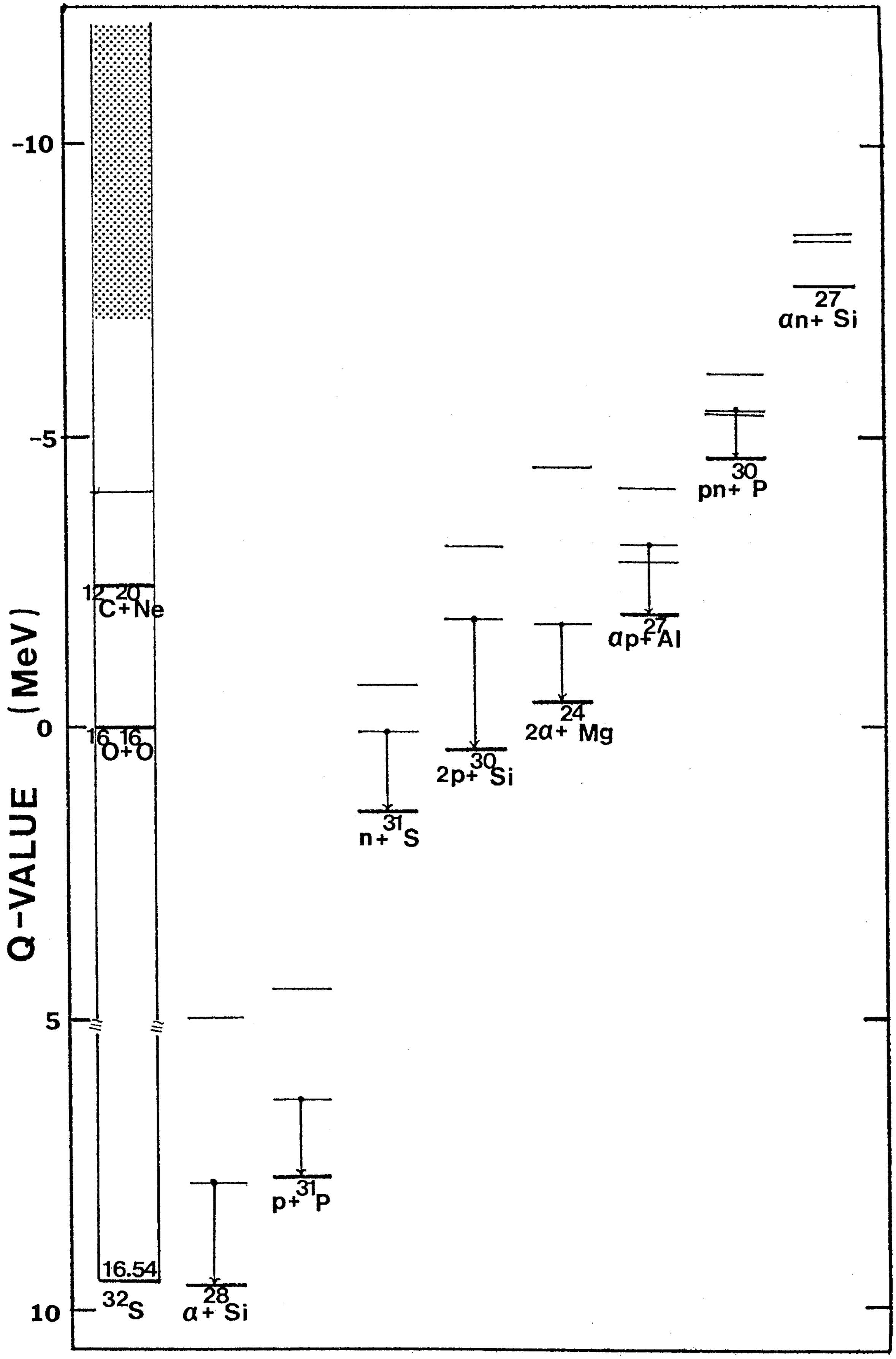
Q-VALUE (MeV)
-10
-5
0
5
10
12 20 C+Ne
16 16 O+O
16.54
32S
28 α+ Si
p+ 31P
n+ 31S
2p+ 30Si
2α+ 24Mg
αp+ 27Al
pn+ 30P
αn+ 27Si

Figure 23

Gamma-ray Pulse-height Spectrum from the $^{16}O + ^{16}O$ Reaction

The γ-ray peak at 3498 keV from $^{30}Si(2 \rightarrow 0)$ is shown on an expanded scale in the inset. The labelled full-energy peaks are identified in table 10. γ-rays with $E_\gamma \geq 2$ MeV are strongly Doppler shifted and broadened as expected from their relatively short lifetimes. For more details, see pages 70 and 79.

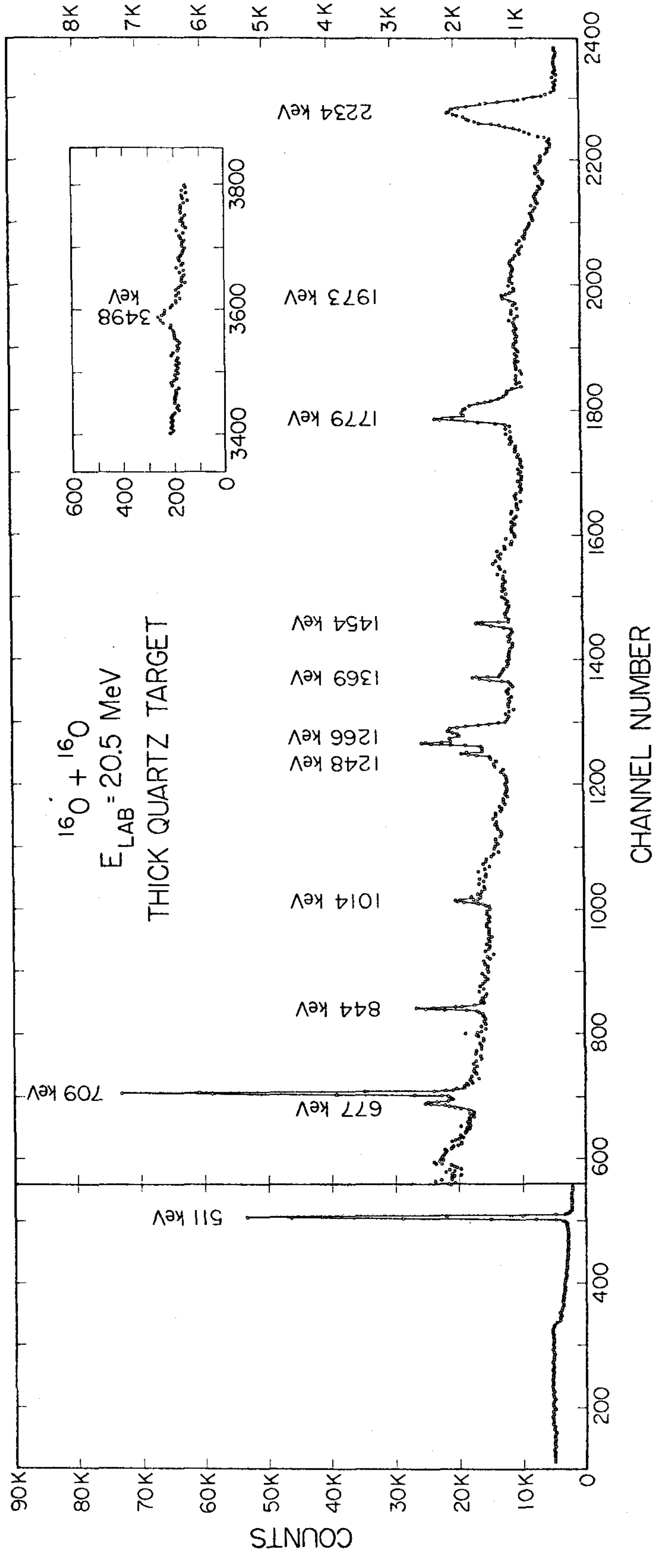
$^{16}O + ^{16}O$
$E_{LAB} = 20.5$ MeV
THICK QUARTZ TARGET
511 keV
677 keV
709 keV
844 keV
1014 keV
1248 keV
1266 keV
1369 keV
1454 keV
1779 keV
1973 keV
2234 keV
3498 keV
COUNTS
CHANNEL NUMBER
0
10K
20K
30K
40K
50K
60K
70K
80K
90K
1K
2K
3K
4K
5K
6K
7K
8K
200
400
600
800
1000
1200
1400
1600
1800
2000
2200
2400
3400
3600
3800
0
200
400
600

Figure 24

Profiles of the Hydrogen Distribution in the Evaporated Silicon Monoxide Target

The ordinate represents the integrated number of counts with pulse height $\geq$ 2 MeV per 100 μC. The surface peak is most likely caused by a few monolayers of water adsorbed on the target. The target thickness determination is described in page 76.

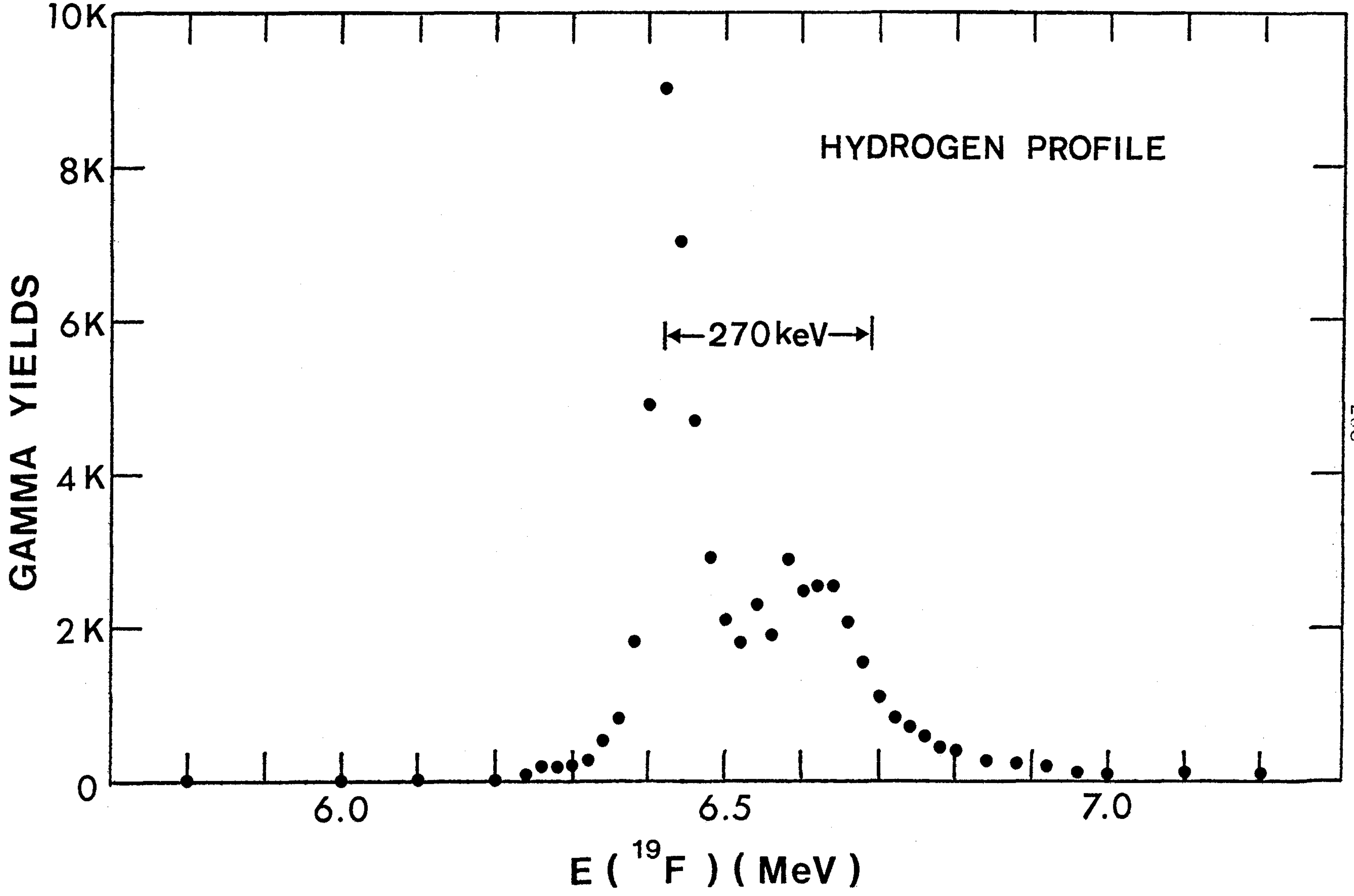
HYDROGEN PROFILE
270keV
GAMMA YIELDS
10K
8K
6K
4K
2K
0
6.0
6.5
7.0
E (^{19}F) (MeV)

Figure 25

Some γ-ray Yields from the ^{12}C + ^{16}O Reactions

The evaporated silicon monoxide target was bombarded with a ^{12}C beam. Yields of the 844 keV and 1014 keV γ-rays from the ^{27}Al residual mucleus, and the yield of the 1369 keV γ-rays from the ^{24}Mg residual nucleus were measured. These measurements were used to correct the ^{16}O + ^{16}O yields of the same γ-rays for possible carbon impurities in the targets. For details, see pages 77 and 82.

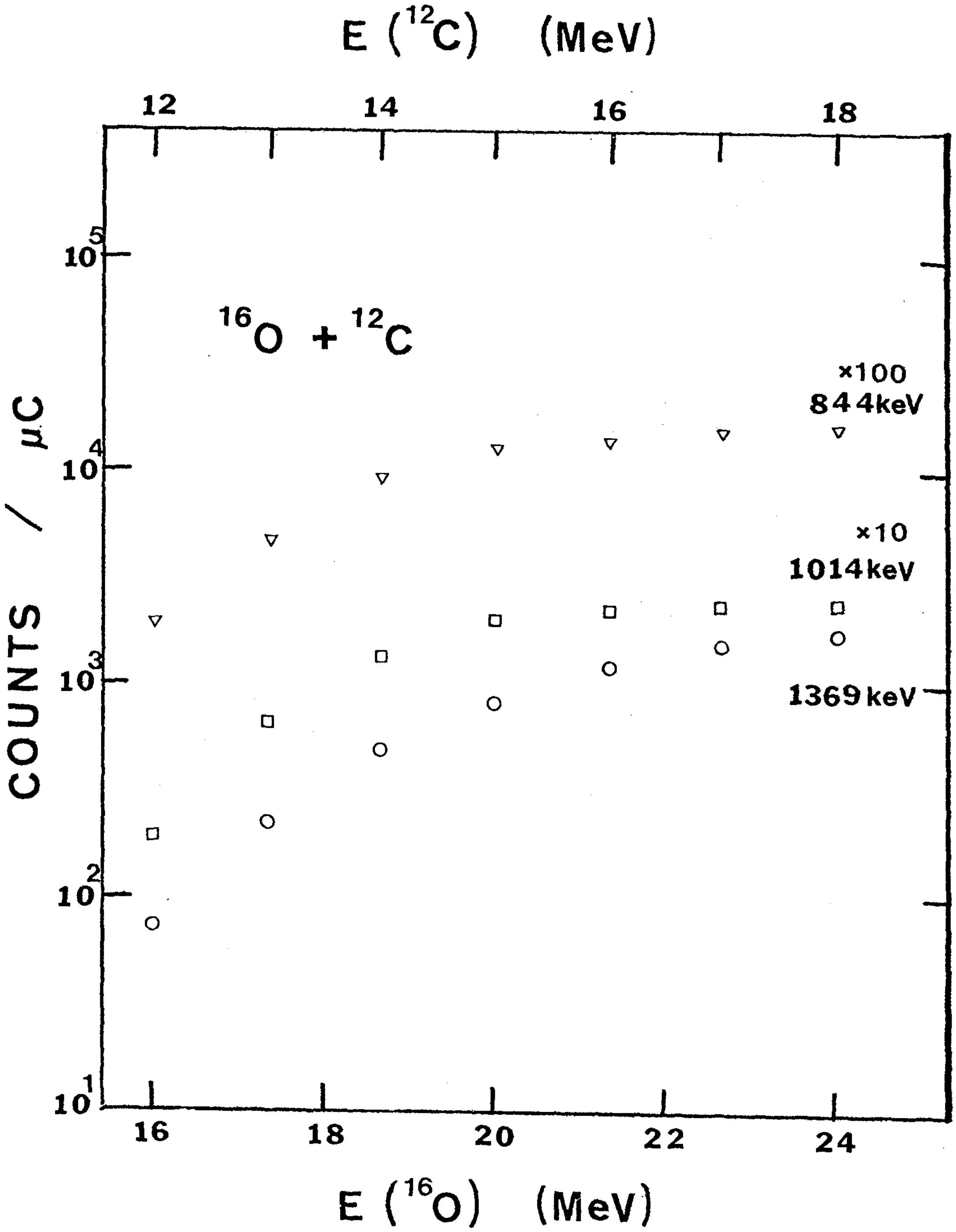
E (^{12}C) (MeV)
12
14
16
18
10^5
10^4
10^3
10^2
10^1
^{16}O + ^{12}C
×100
844keV
×10
1014keV
1369 keV
COUNTS / µC
16
18
20
22
24
E (^{16}O) (MeV)

Figure 26

Some γ-ray Yields from the $^{16}O + ^{16}O$ Reactions

The yields of the 844 keV, 1014 keV and 1369 keV γ-rays were measured with an anodized tantalum target, bombarded by ^{16}O. The observed γ-ray excitation functions are quite different from those in fig. 25. The filled circles indicate repeated measurements at $E(^{16}O) = 18.0$ MeV after 8 hours, showing some evidence of ^{12}C build-up. The repeated measurements at $E(^{16}O) = 20.0$ MeV and 22.0 MeV were essentially identical to the data points obtained earlier, and are therefore not shown. For details, see page 82.

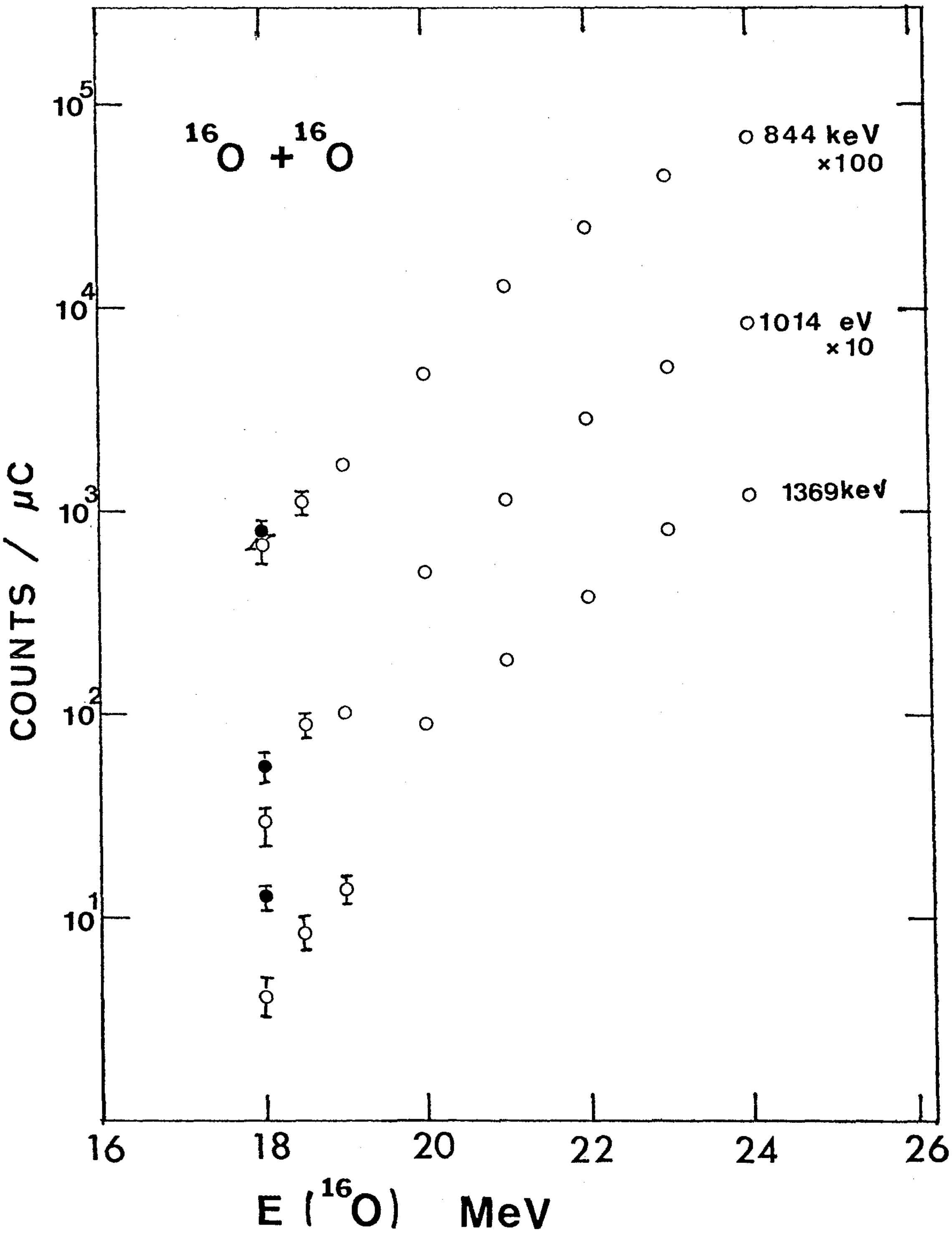
$^{16}O + ^{16}O$
844 keV ×100
1014 eV ×10
1369keV
COUNTS / μC
10^5
10^4
10^3
10^2
10^1
16
18
20
22
24
26
E (^{16}O) MeV

Figure 27

Transmission Coefficients for the α + ^{28}Si Channel

The transmission coefficients were computed with the computer code HAUSER*4, with the optical model parameters given in table 11. The filled circles indicate energies at which the transmission coefficients for the orbital angular momenta, $\ell = 0$ and $\ell = 10$, were calculated. For details, see page 86.

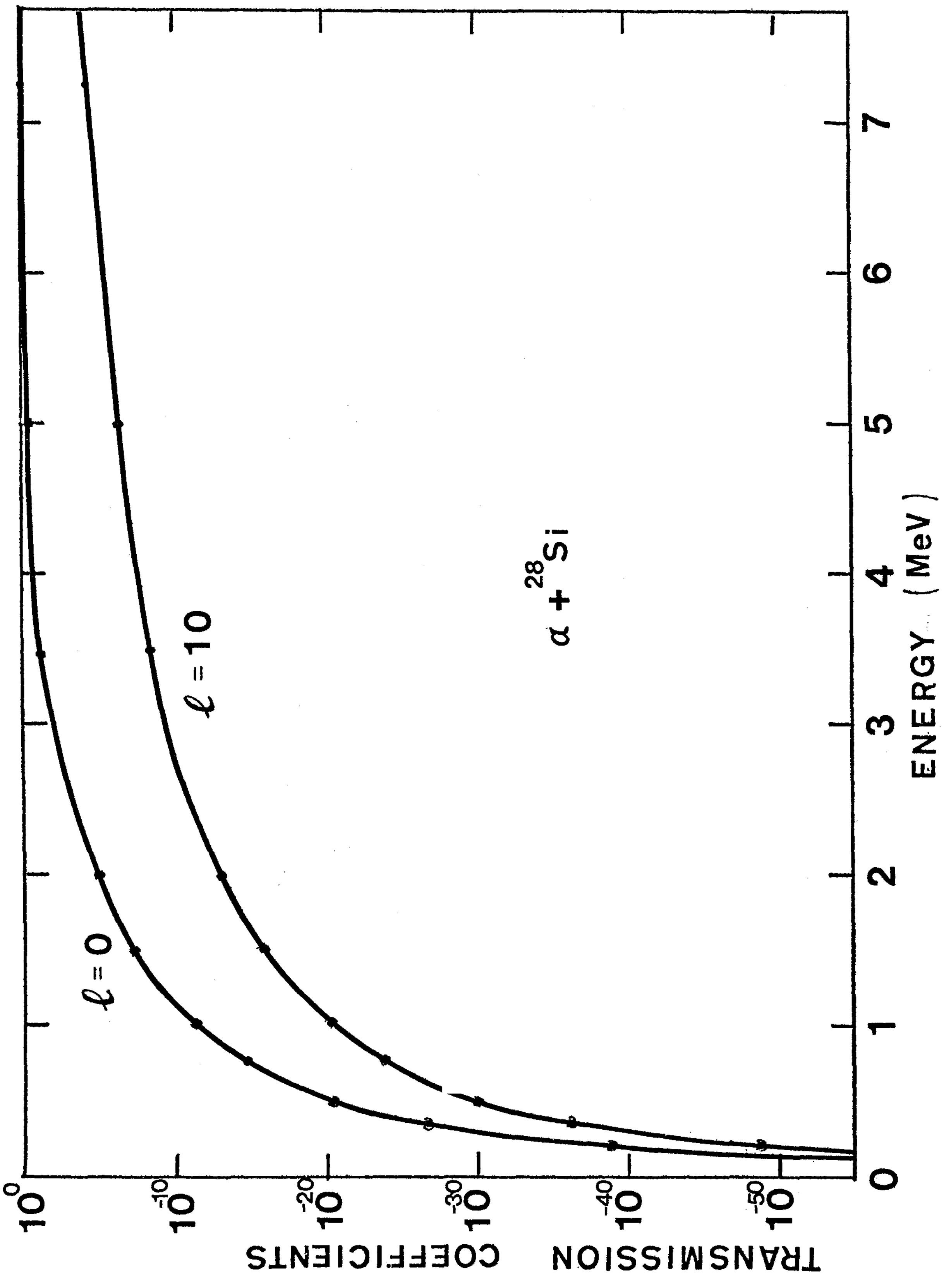
TRANSMISSION COEFFICIENTS
10^0
10^-10
10^-20
10^-30
10^-40
10^-50
ENERGY (MeV)
0
1
2
3
4
5
6
7
ℓ = 0
ℓ = 10
α + 28Si

Figure 28

Semi-logarithmic Plot of the Integrated Number of Discrete Levels vs. Excitation Energy

The solid line is a fit to the general trend of the energy dependence of the total number of levels. The parameters, E_0 and T, determined from this line are $E_0 = -0.19$ MeV, T = 1.93 MeV. Level densities are described on page 87.

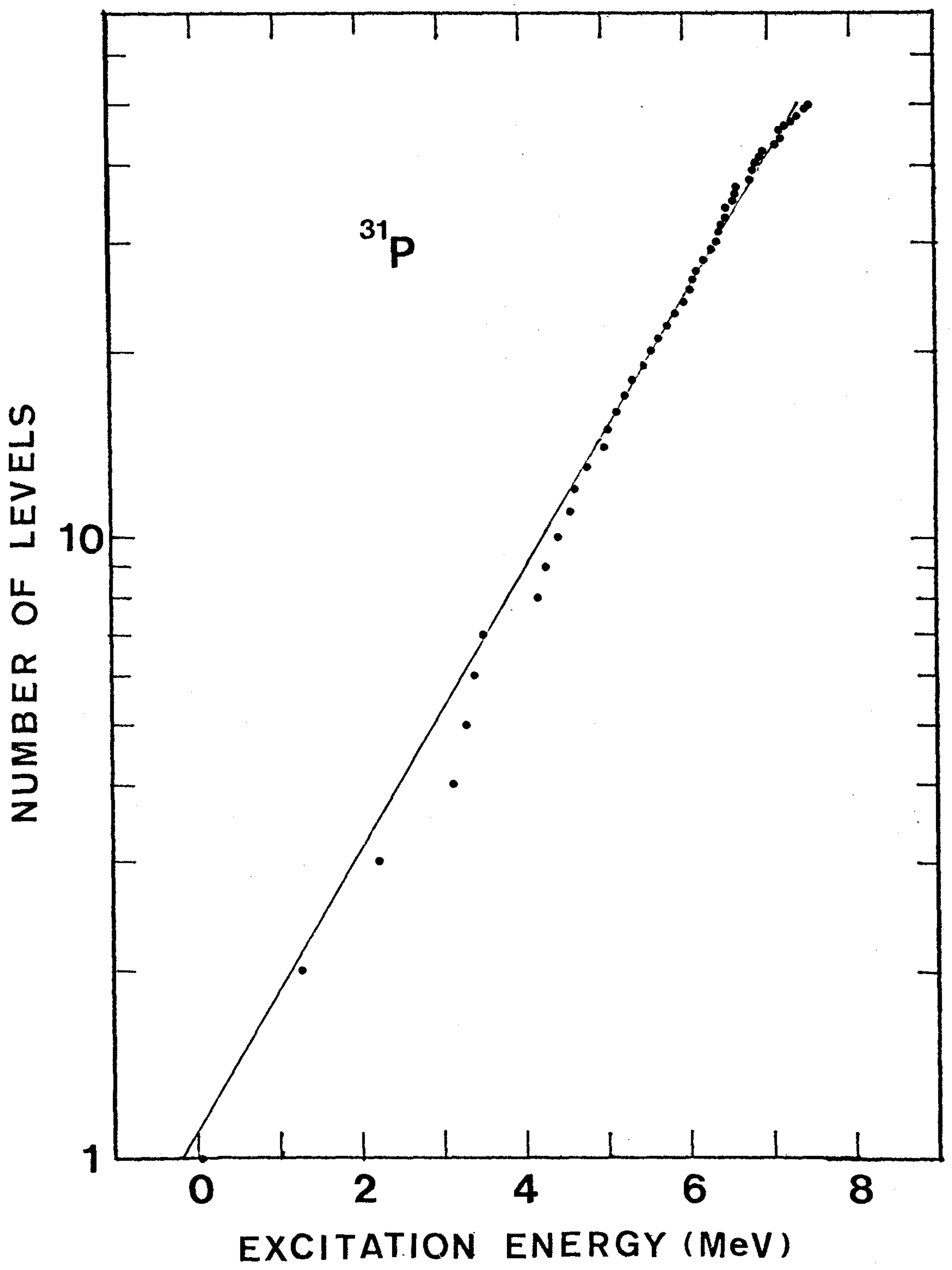
^{31}P
NUMBER OF LEVELS
10
1
0
2
4
6
8
EXCITATION ENERGY (MeV)

Figure 29

Probability Function for the ^{28}Si Intermediate Nucleus

The probability for evaporating an α-particle or a proton as a function of ^{28}Si excitation energy was calculated at the energies indicated. The straight lines indicate that the computer code HAUSER*4 interpolates the probability function linearly for the particular energies necessary in the calculation of eq.(III-17) in page 89. Only the probability function for spin and parity 0^+ states of the nucleus ^{28}Si are shown here. The oscillatory structure reflects the summation over the final states of the nuclei ^{24}Mg and ^{27}Al. For details, see page 90.

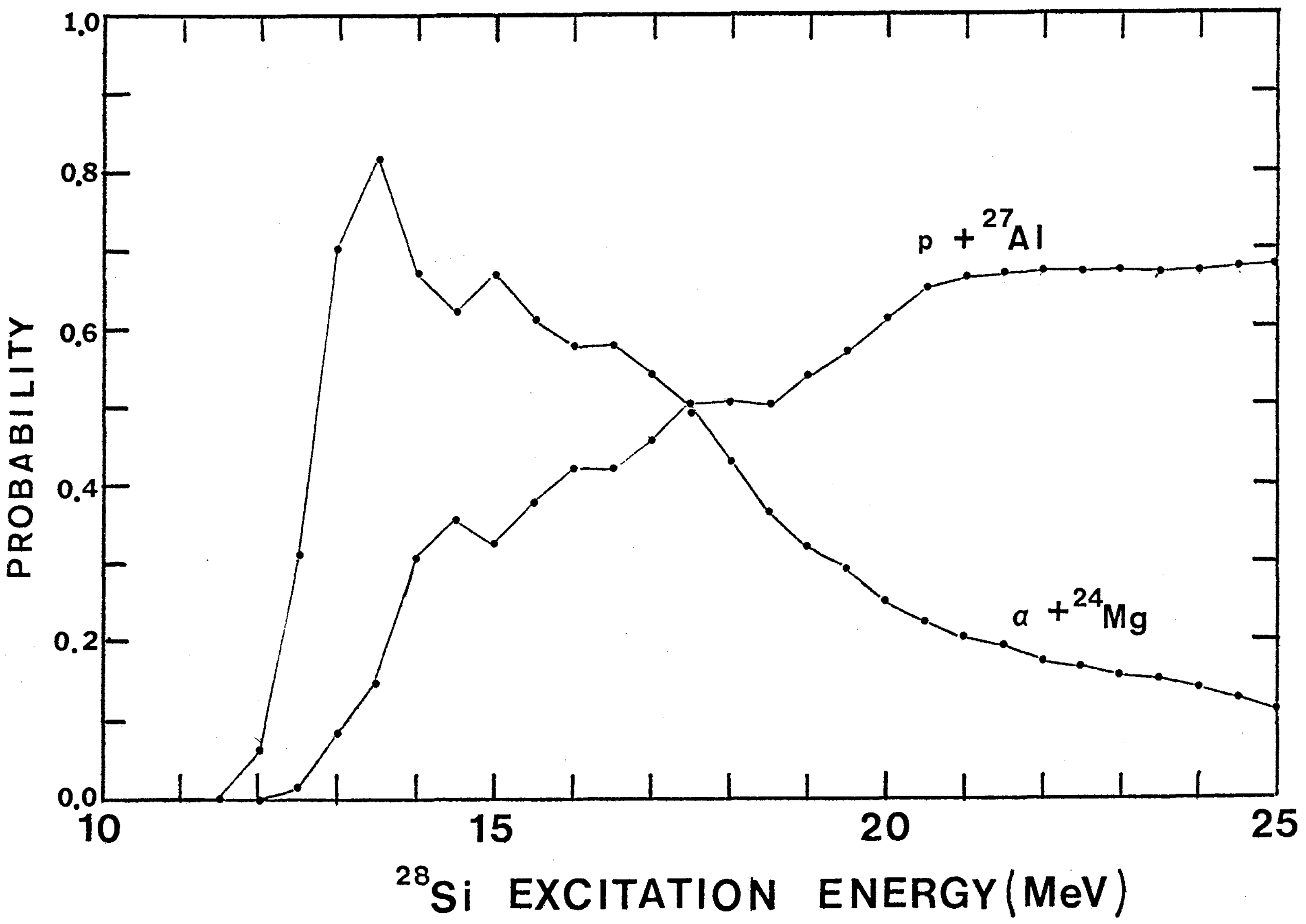
PROBABILITY
0.0
0.2
0.4
0.6
0.8
1.0
10
15
20
25
^{28}Si EXCITATION ENERGY (MeV)
p + ^{27}Al
α + ^{24}Mg

Figure 30

Bound State Fractions for ^{28}Si and ^{31}P

The bound state fractions represent the probability that, when ^{28}Si or ^{31}P is formed, it cannot decay by particle emission. The cross sections necessary for calculating the bound state fractions were obtained from statistical model calculations. For more details, see page 91.

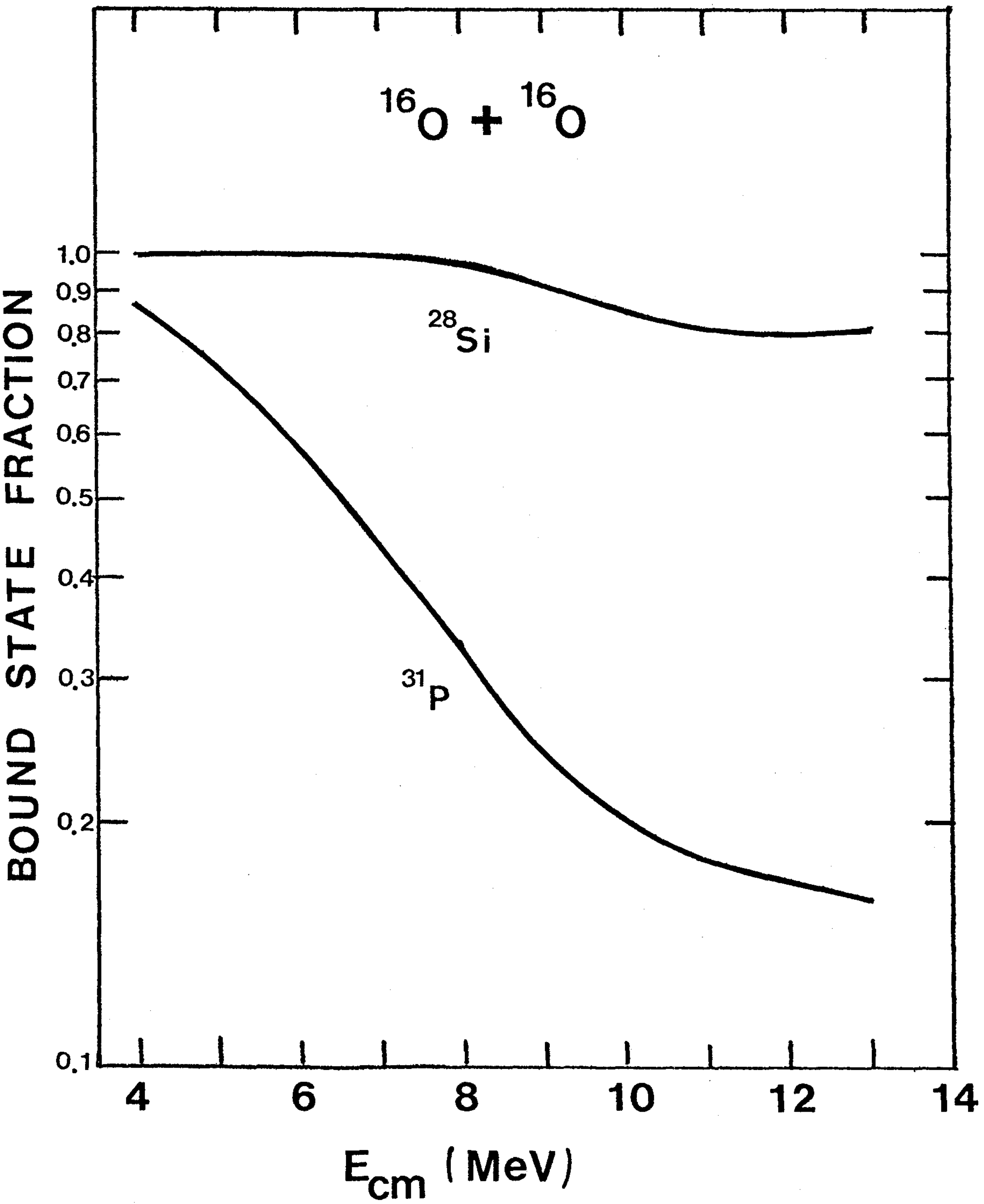
$^{16}O + ^{16}O$
BOUND STATE FRACTION
1.0
0.9
0.8
0.7
0.6
0.5
0.4
0.3
0.2
0.1
^{28}Si
^{31}P
4
6
8
10
12
14
E_{cm} (MeV)

Figure 31

Summing and Branching Correction Factors for the γ-rays Produced by the $^{16}O + ^{16}O$ Reactions

The curves result from a statistical model calculation using the computer code HAUSER*4. For more details, see page 92.

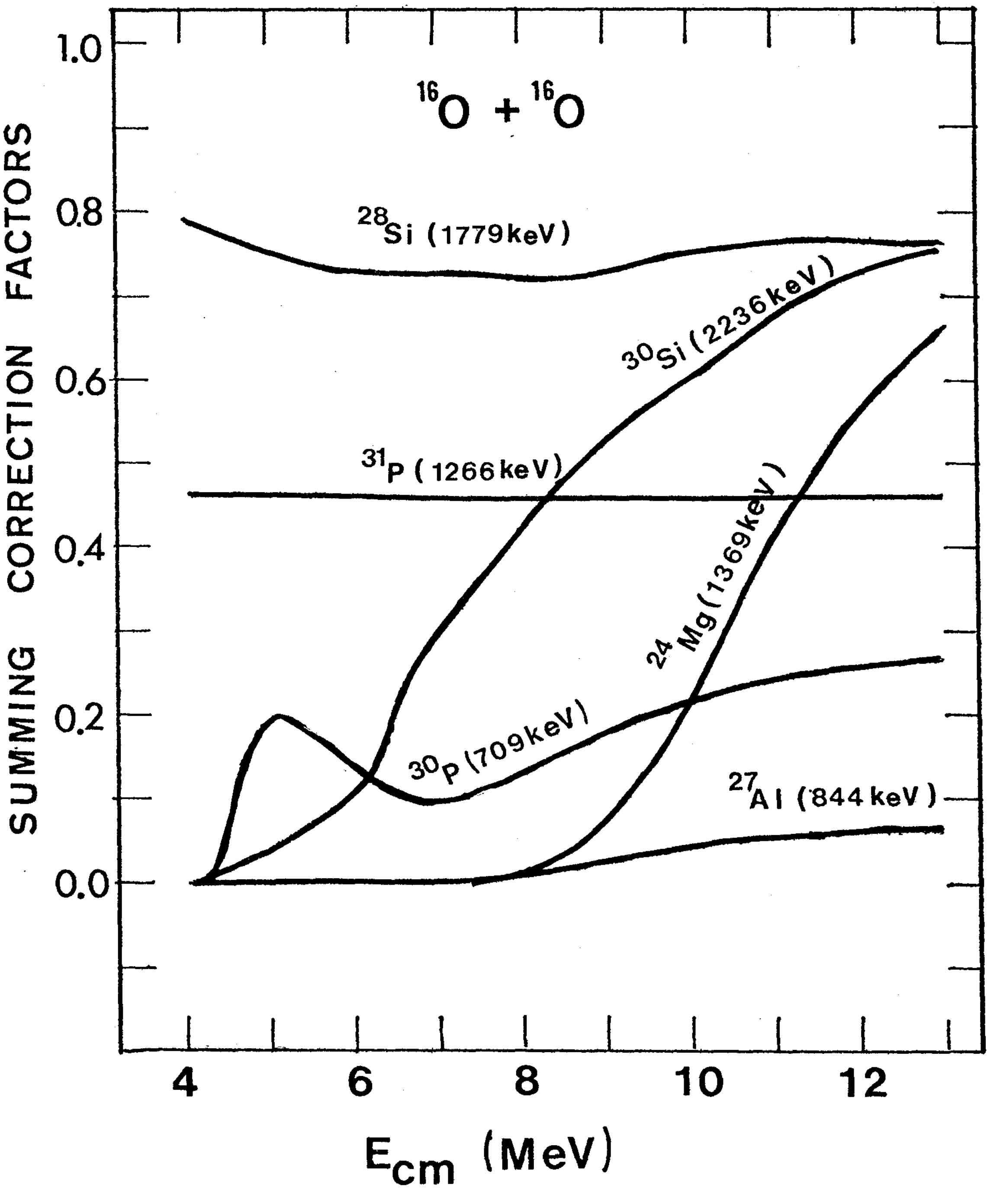
$^{16}O + ^{16}O$
SUMMING CORRECTION FACTORS
1.0
0.8
0.6
0.4
0.2
0.0
4
6
8
10
12
E_{cm} (MeV)
^{28}Si (1779keV)
^{30}Si (2236keV)
^{31}P (1266keV)
^{24}Mg (1369keV)
^{30}P (709keV)
^{27}Al (844keV)

Figure 32

Cross Sections for the Production of ^{28}Si, ^{31}P, ^{31}S and ^{30}Si from the $^{16}O + ^{16}O$ Reactions

The error bars at low energies represent the counting statistics alone. These cross sections were determined from the γ-ray yields measured with the quartz target. For more details, see pages 93 and 94.

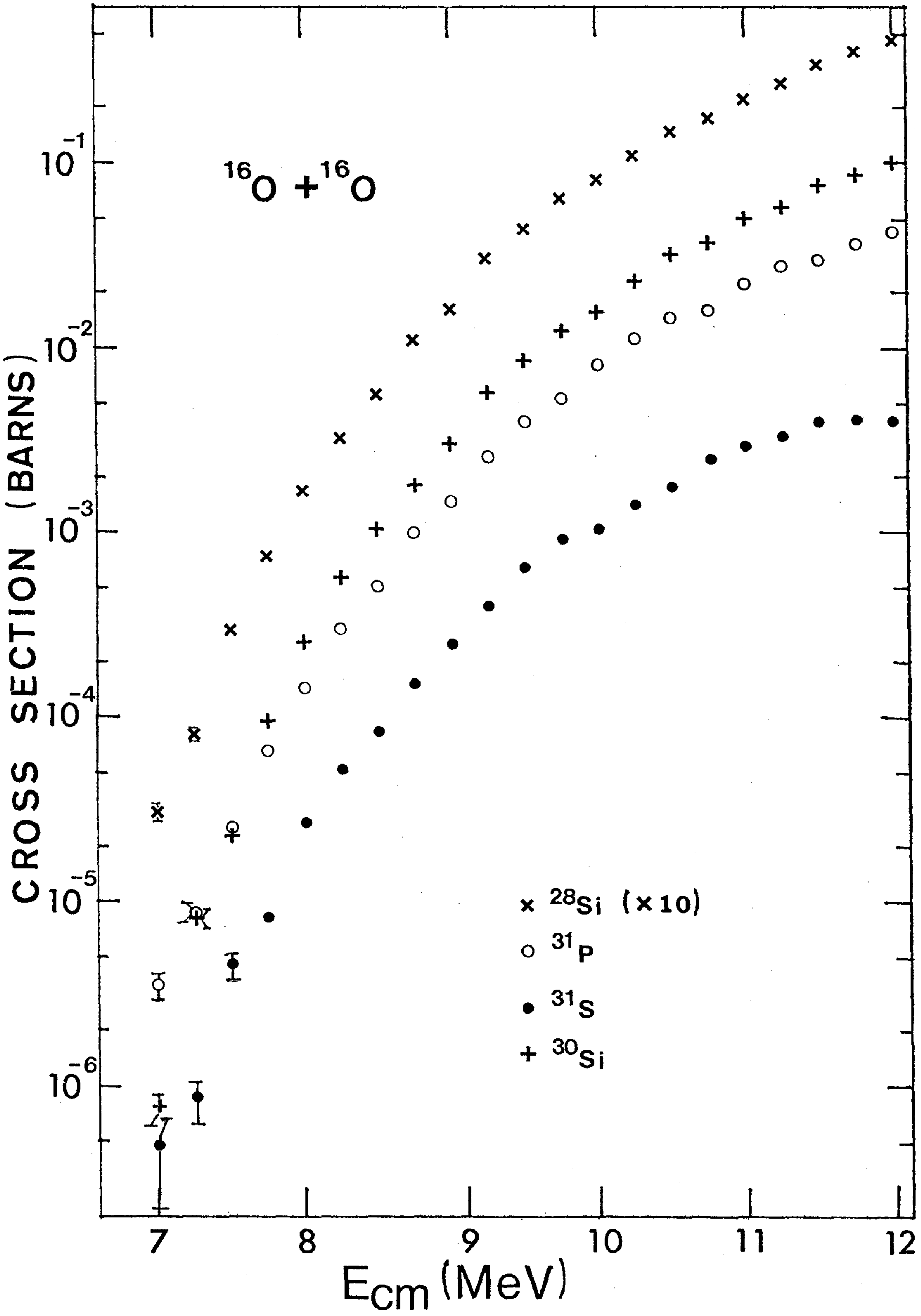
$^{16}O + ^{16}O$
CROSS SECTION (BARNS)
10^{-1}
10^{-2}
10^{-3}
10^{-4}
10^{-5}
10^{-6}
× ^{28}Si (×10)
○ ^{31}P
● ^{31}S
+ ^{30}Si
7
8
9
10
11
12
E_{cm} (MeV)

Figure 33

Cross Sections for Productions of ^{30}P from the $^{16}O + ^{16}O$ Reaction

The error bars indicated are from counting statistics alone. For the other data points, the statistical uncertainties are smaller than the data points. These cross sections were determined from the 709 keV γ-ray yields with a quartz target (open circles), and from an evaporated silicon monoxide target (triangles). The relative excitation function for γ-rays of the same energy obtained with an anodized tantalum target (x) agrees well with the cross sections from the quartz and SiO targets. The open squares indicate the ^{30}P production cross sections of Spinka and Winkler. For more details, see pages 94 and 95.

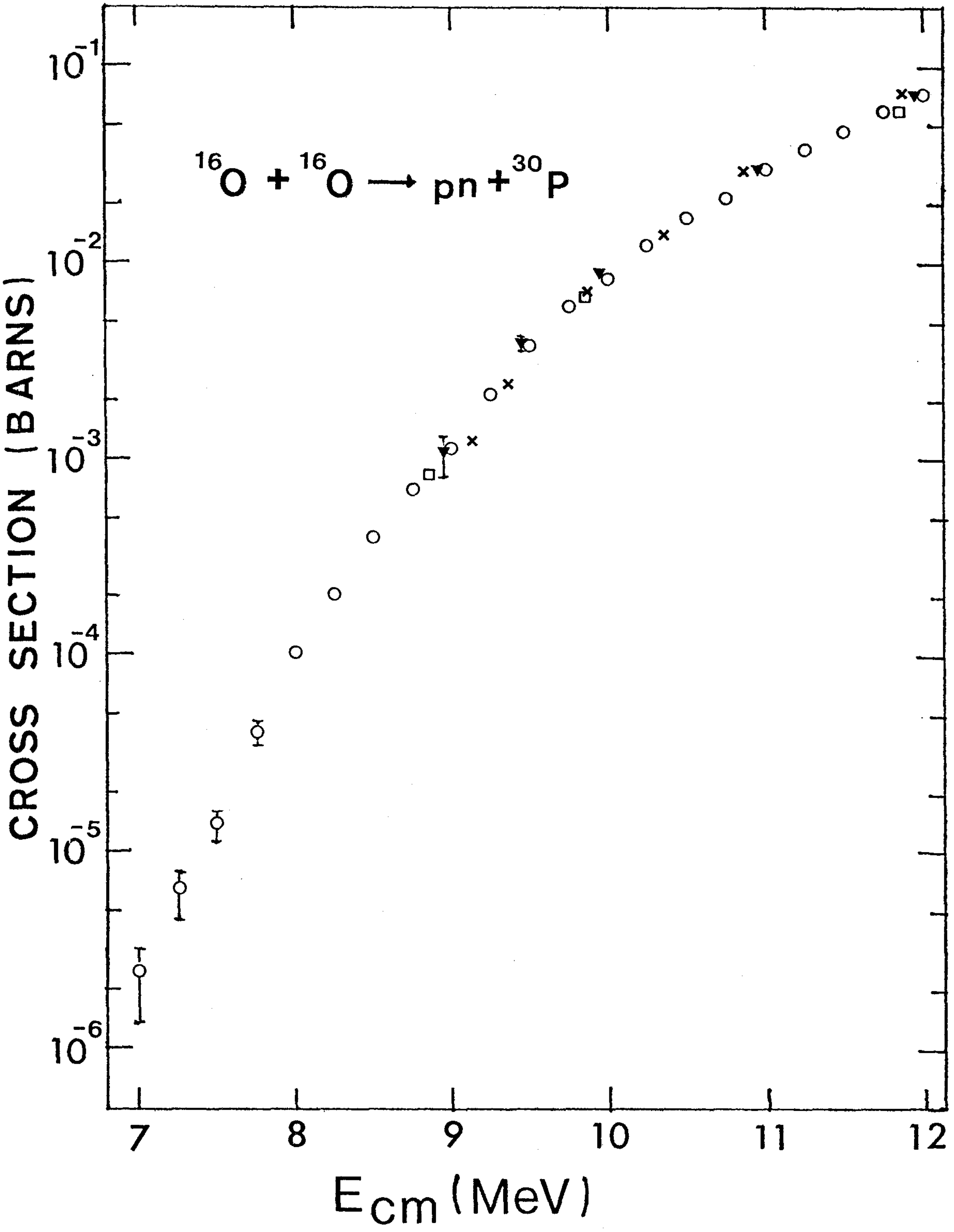
$^{16}O + ^{16}O \longrightarrow pn + ^{30}P$
CROSS SECTION (BARNS)
10^{-1}
10^{-2}
10^{-3}
10^{-4}
10^{-5}
10^{-6}
7
8
9
10
11
12
E_{cm} (MeV)

Figure 34

Cross Sections for Production of ^{24}Mg and ^{27}Al from the ^{16}O + ^{16}O Reactions

The error bars are from counting statistics alone. The open and filled circles represent data obtained with a thick quartz target, while the open and filled triangles represent the data obtained with an anodized tantalum target. The dashed curves are relative cross sections calculated from the statistical model, and were used to estimate the cross sections for the production of ^{24}Mg and ^{27}Al at lower energies. For more details, see pages 96 and 97.

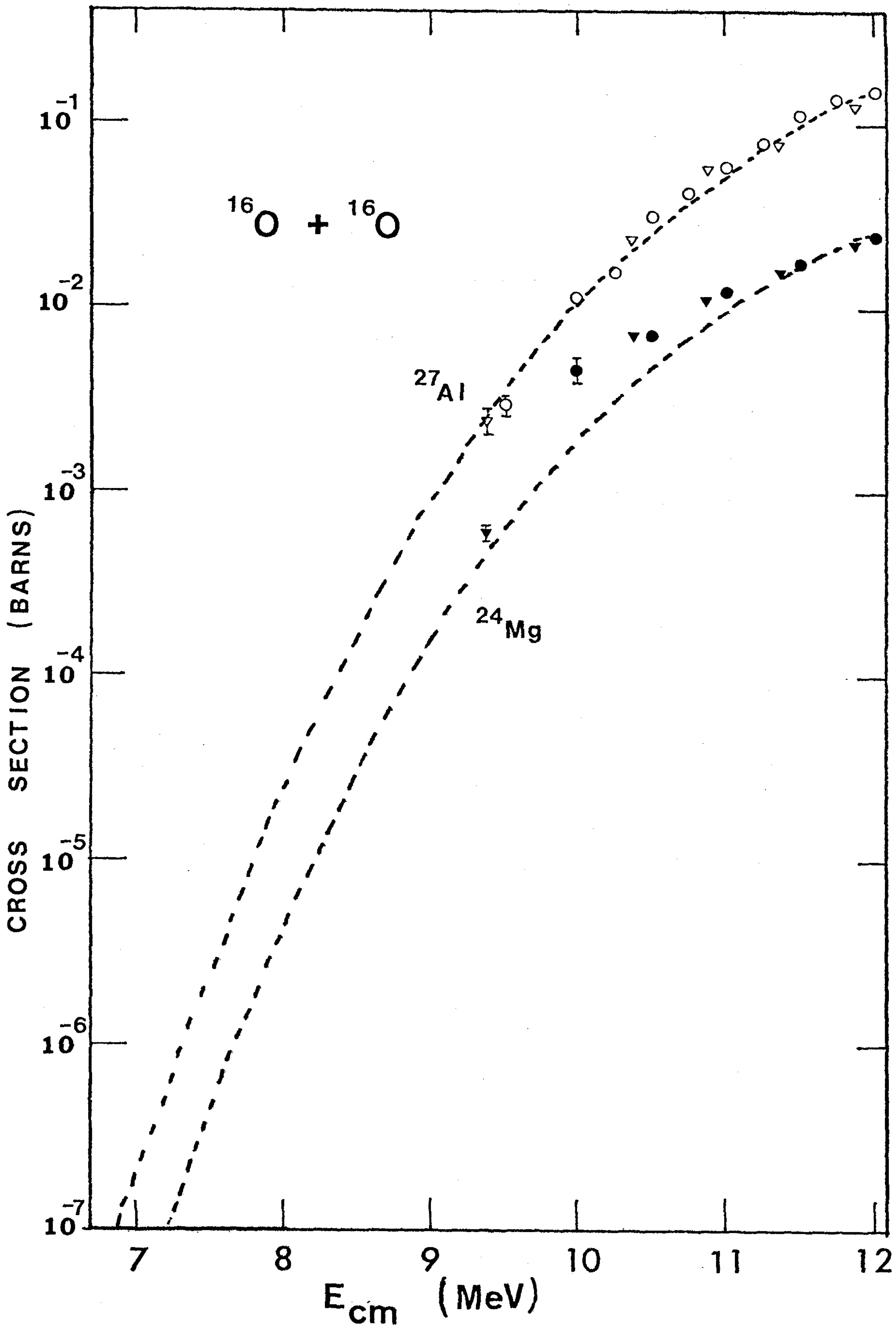
$^{16}O + ^{16}O$
^{27}Al
^{24}Mg
CROSS SECTION (BARNS)
10^{-1}
10^{-2}
10^{-3}
10^{-4}
10^{-5}
10^{-6}
10^{-7}
7
8
9
10
11
12
E_{cm} (MeV)

Figure 35

Total Fusion Cross Sections for the $^{16}O + ^{16}O$ Reactions

The fusion cross sections, shown as filled circles, were obtained by the summation of the cross sections for ^{28}Si, ^{31}P, ^{31}S, and ^{30}Si (fig. 32), ^{30}P (fig. 33), and ^{24}Mg and ^{27}Al (fig. 34) The open circles are the total cross sections measured earlier by Spinka and Winkler by detecting protons and alpha-particles. Comparisons with other data are given in chapter V. For more details, see pages 98 and 104.

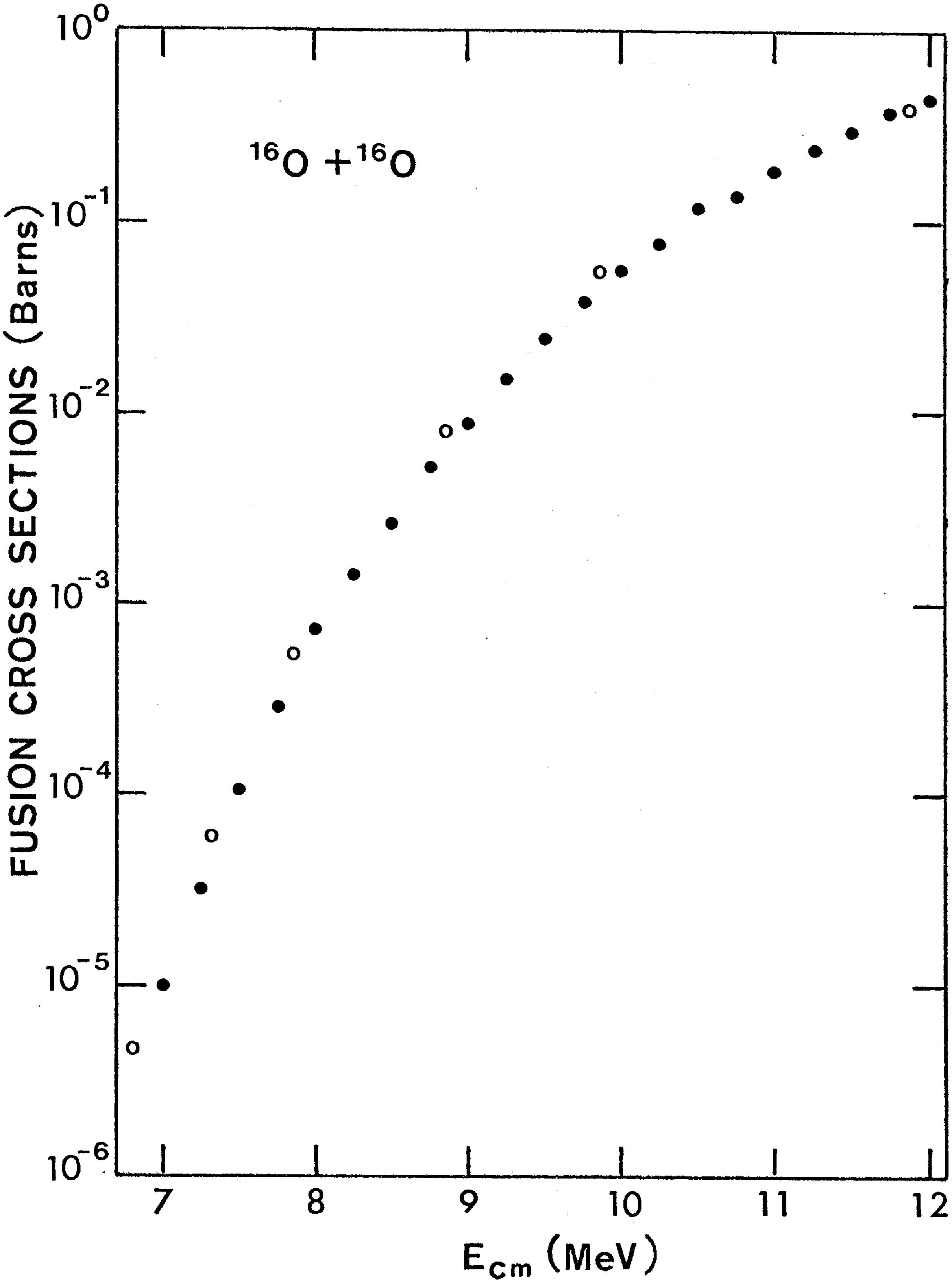
$^{16}O + ^{16}O$
FUSION CROSS SECTIONS (Barns)
10^0
10^{-1}
10^{-2}
10^{-3}
10^{-4}
10^{-5}
10^{-6}
7
8
9
10
11
12
E_{cm} (MeV)

Figure 36

Total Fusion Cross Sections Inferred Independently from the α-channel and p-channel

The cross sections were calculated by dividing the cross sections for the production of ^{28}Si (or ^{31}P) by the bound state fractions shown in fig. 30. The dashed curve shows the total fusion cross sections from fig. 35 for comparison. For more details, see pages 100 to 102.

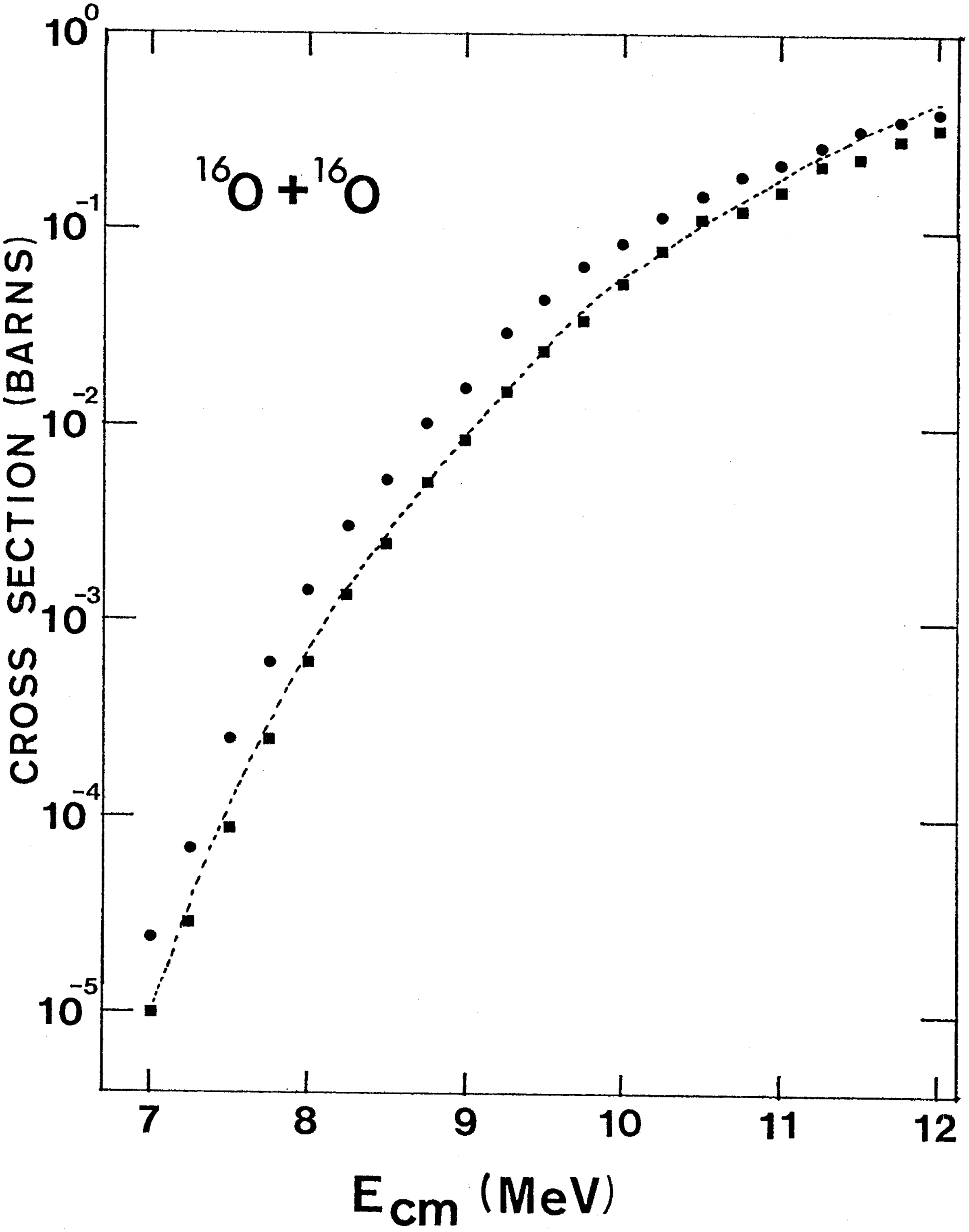
$^{16}O + ^{16}O$
CROSS SECTION (BARNS)
10^0
10^{-1}
10^{-2}
10^{-3}
10^{-4}
10^{-5}
7
8
9
10
11
12
E_{cm} (MeV)

Figure 37

S-factor for the $^{16}O + ^{16}O$ Fusion Reaction

The filled circles are the S-factors measured in the present work. The open circles are the results of Spinka and Winkler. For more details, see pages 102 and 104.

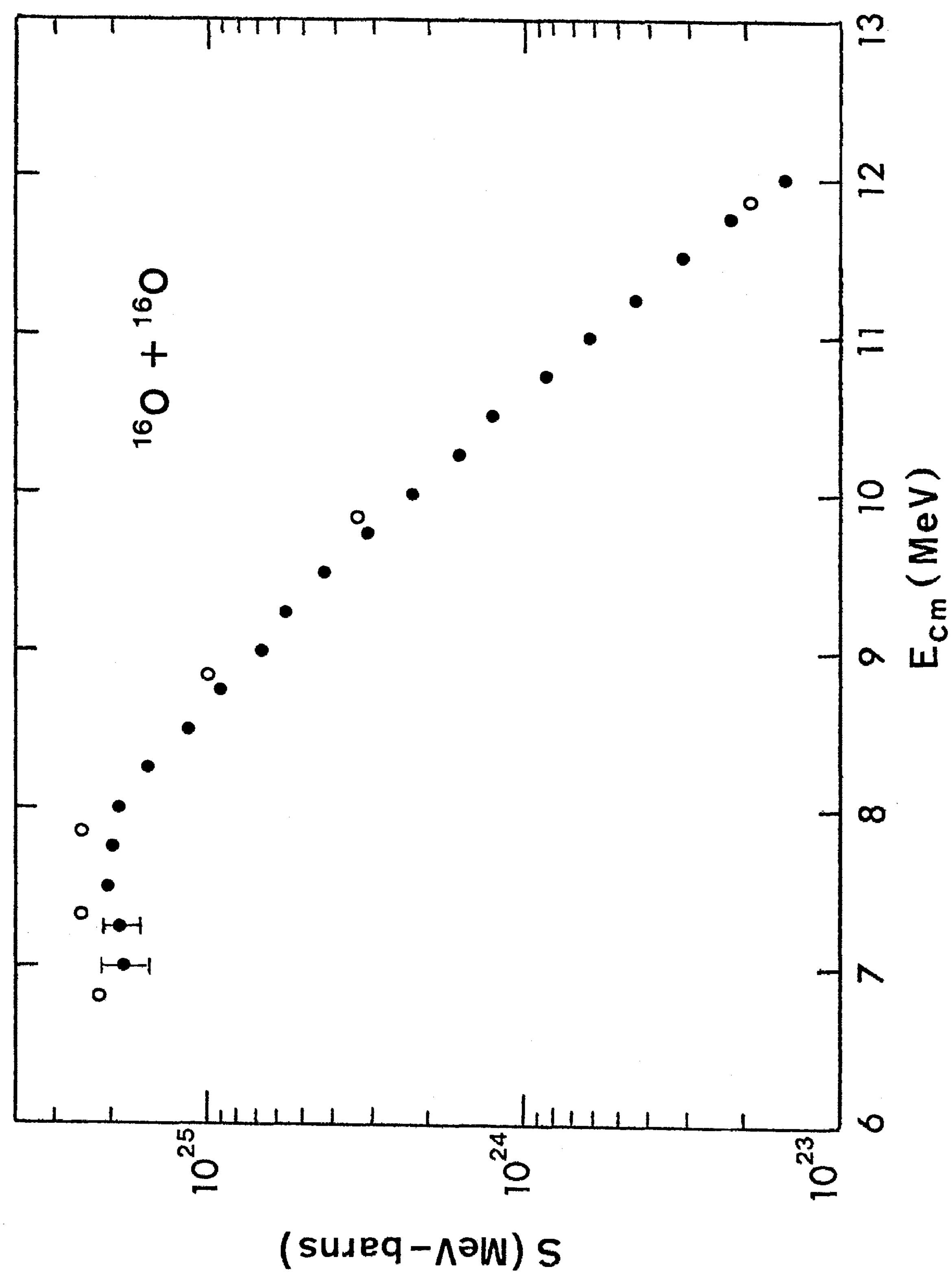
$^{16}O + ^{16}O$
S (MeV−barns)
10^{25}
10^{24}
10^{23}
E_{cm} (MeV)
6
7
8
9
10
11
12
13